Measuring Ozone Deposition to the Ocean Surface and Assessing its Biogeochemical Controls

David Christopher Loades

Doctor of Philosophy

University of York

Chemistry

September 2021

Abstract

Dry deposition of ozone to the sea surface represents a significant portion of global tropospheric ozone loss. It introduces considerable uncertainty in global models due to limited understanding of the reactivity of iodide and organic material in the sea surface towards ozone. This is particularly true of organic material due to its variable composition.

This thesis details ozone flux and associated measurements at and around the Penlee Point Atmospheric Observatory (PPAO) on the UK south coast from 2018 until 2021 where coastal ozone flux was calculated via eddy covariance. Monthly median deposition velocity was 0.007 – 0.033 cm s^{-1} across all fieldwork, similar to the values reported from ship-based measurements: 0.009 – 0.034 cm s^{-1}.

Iodide and dissolved organic carbon (DOC) concentrations in the water within the flux footprint were ~50 to ~100 nmol dm^{-3} and 1.3 – 2.2 mg dm^{-3}. While iodide increased to a peak in July (coinciding with phytoplankton blooms), DOC conversely peaked in November. These measurements were used with a 1-layer and a 2-layer model to compare deposition observations to predictions. The 1-layer model in the absence of DOC reactivity typically gave values closest to observations and showed a similarly strong variation with friction velocity. Inclusion of the DOC-ozone reaction with a rate constant of 3.7×10^{-6} dm^3 mol^{-1} s^{-1} caused both models to overestimate, but also mimic some variation between months suggesting its contribution was overestimated, but still important.

Liquid chromatography-mass spectrometry was used to identify compounds in the water near the PPAO. Double bond equivalence decreased following exposure to 500 ppbv ozone, while dicarboxylic acid concentrations increased, potentially due to unsaturated fatty acid ozonolysis. Several dicarboxylic acid concentrations in PPAO samples fell from November – April, similarly to DOC concentrations. The potential for some introduction of dicarboxylic acids as contaminants from the sampling method remains a possibility.

List of Contents

List of Tables

List of Figures

Acknowledgements

This PhD was funded by the NERC SPHERES doctoral training program.

I would firstly like to thank my supervisors: Prof. Lucy Carpenter and Prof. James Lee. It has been a pleasure working with both them and their respective research groups. I could not have hoped for better support and supervision throughout my project.

I would like to thank members of both the Carpenter group and the Lee group for a wealth of practical help, insightful conversations, and moral support over the last 4 years, as well as many other students and members of staff within the Wolfson Atmospheric Chemistry Laboratories. I would especially like to thank Dr Liselotte Tinel who conducted the DOC measurements as well as many of the iodide measurements presented in this thesis, and Dr Rosie Chance who developed and refined the LCMS method used in this work.

My thanks also go to the staff at the Plymouth Marine Laboratory who made the fieldwork possible. Special thanks to Dr Ming-Xi Yang and Dr Tom Bell who were instrumental in the installation of equipment at the Penlee Point Atmospheric Observatory, and to Jani Pewter who kept things running throughout covid-19. This work would not have been possible without their hard work, and that of all those involved in collecting, processing, and distributing water samples.

Finally, a massive thank you to my parents who have supported me through this PhD just as they have with anything I have ever done.

Author's Declaration

I declare that this thesis is a presentation of original work and I am the sole author. This work has not previously been presented for an award at this, or any other, University. All sources are acknowledged as references.

I am the first author on the following publication[1], which discusses the first phase of fieldwork reported in Chapters 2 and 3:

Loades, D. C. *et al.* Ozone deposition to a coastal sea: comparison of eddy covariance observations with reactive air-sea exchange models. *Atmos. Meas. Tech.* **13**, 6915-6931 (2020).

1. Introduction

1.1 The Importance of Ozone

Ozone (O_3) exists as a trace gas throughout the atmosphere. The majority of atmospheric ozone is situated in the stratosphere where its high concentrations (sometimes referred to as the 'ozone layer') absorbs UV-B light that would otherwise prove highly damaging to life on the Earth's surface. By contrast, although it is present at far lower concentrations in the troposphere (tens of ppb), ozone is considered a harmful pollutant in many ways.

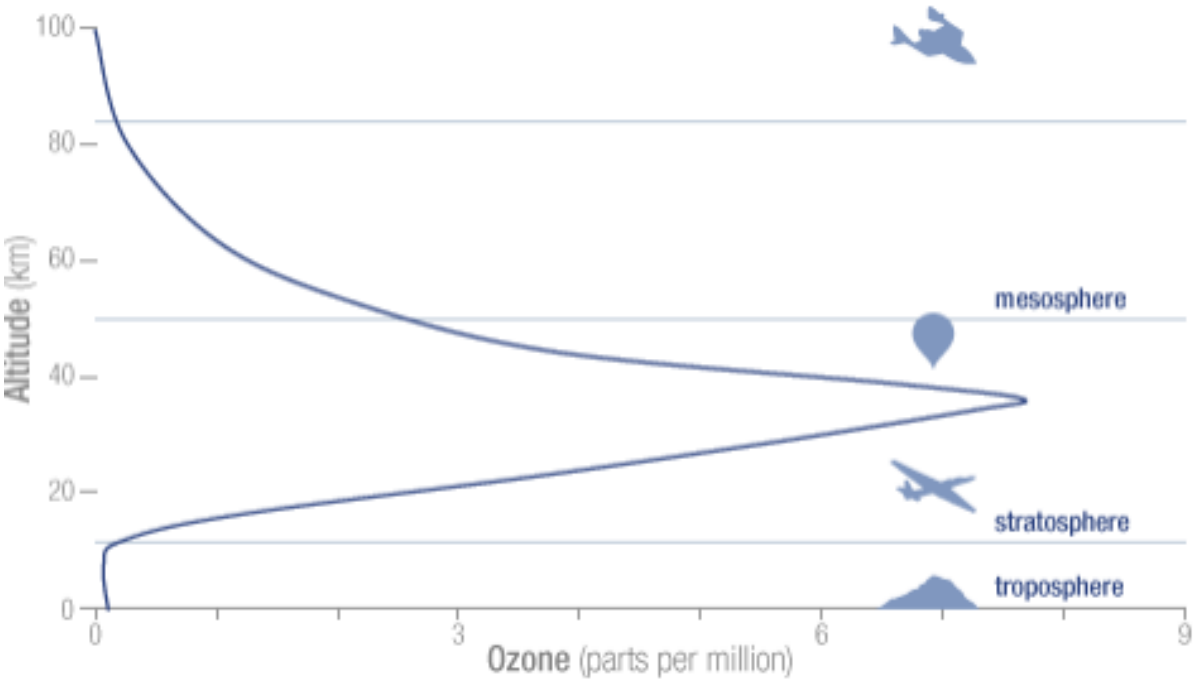

Figure 1.1: The vertical profile of ozone in the atmosphere: https://ozonewatch.gsfc.nasa.gov/facts/

In humans, ozone has been linked to the exacerbation of asthma[2–7], cystic fibrosis[7], pneumonia, chronic obstructive pulmonary disease[8], and even mental health[9]. As such, the WHO recommends an 8-hour exposure limit of 50 ppb, not far above the 35-40 ppb levels typically seen in the northern hemisphere[10]. Tropospheric ozone levels increased throughout the 20th century in the northern hemisphere particularly as anthropogenic emissions of ozone generating compounds rose[11]. Today, exceedances of this limit are common[12–14], and the frequency of future exceedances will depend heavily on how successfully precursor emission controls are implemented[15–17].

In addition to its effects on human health, ozone is also harmful to plants, affecting both crops and natural ecosystem diversity. The yield and health of many globally important crops such as maize[18,19], wheat[20,21], rice[20,22], and soybeans[21] has been shown be affected by high ozone concentrations. This not only has implications for food security as the global population increases, but also for the economy due to the loss of income from staple crops[22,23]. The effects of tropospheric ozone are also important

for natural environments, such as the stability and growth of forests[24]. With an estimated 40% of terrestrial ecoregions enduring ozone levels beyond the threshold for ecological risk in 2000[25], the potential risks to biodiversity posed by high tropospheric ozone is great.

Beyond its acute health effects on both animal and plant life, ozone also has climatological effects due to its interaction with many greenhouse gases. While ozone in the stratosphere has a net cooling effect on the Earth, tropospheric ozone increases temperatures, contributing towards global warming[26]. Establishing the warming caused by ozone presents a number of challenges, particularly because its short lifetime (relative to other greenhouse gases such as CO_2 and methane) means that it is not well mixed spatially. This short lifetime also means that direct historical observations (such as those from ice cores) are not available, nor is there a reliable proxy for ozone concentration. As such, assessing the warming caused by ozone since pre-industrial times (~1750) relies heavily on modelling. Nevertheless, the warming potential of tropospheric ozone, expressed as a radiative forcing (RF) value, has been estimated by multi-model studies as part of the atmospheric chemistry and climate model intercomparison Project (ACCIMP) to be 0.34 W m^{-2} between the years from 1850-2000[27–29]. The fifth assessment report of the Intergovernmental Panel on Climate Change (IPCC) expanded the considered period to 1750-2010 using models that cover this period[30–32] to yield a total RF value of 0.40 W m^{-2} since pre-industrial times[33]. This makes the warming effect of tropospheric ozone comparable to that of halocarbons[33].

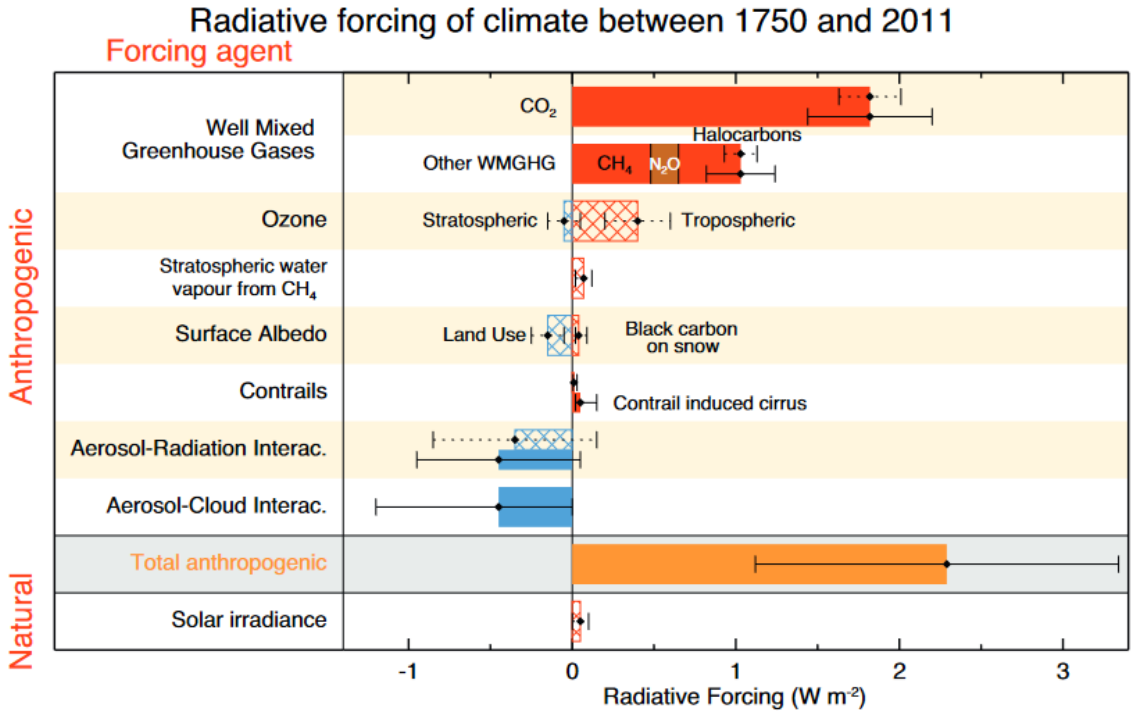

Figure 1.2: Radiative forcing estimates for different forcing agents, IPCC: https://www.ipcc.ch/site/assets/uploads/2018/02/WG1AR5_Chapter08_FINAL.pdf

Finally, ozone contributes to the oxidative environment in the atmosphere, with the capacity to oxidise a range of non-radical species. Its concentration also partially dictates the formation of hydroxy radicals (OH) via the formation of exited atomic oxygen and its subsequent reaction with water vapour.

$$O_3 + h\nu \rightarrow O_2 + O(^1D) \quad \text{(R1)}$$

$$O(^1D) + M \rightarrow O + M \quad \text{(R2)}$$

$$O(^1D) + H_2O \rightarrow 2OH \quad \text{(R3)}$$

Since ozone exists in higher concentrations in the stratosphere, and is exposed to greater UV radiation there, (R1) proceeds more rapidly than in the troposphere. However, the narrow band of wavelengths in the range 300-320 nm penetrate deep enough into the atmosphere to reach ozone in the troposphere, where the relatively high water vapour concentrations promote the formation of OH through (R3)[34]. The ability of OH to oxidise non-radical species then facilitates the removal of notable pollutants such as carbon monoxide (CO), and greenhouse gases such as methane (CH_4). These mechanisms play a central role in the chemical production of ozone in the troposphere and are discussed in Section 1.2.

1.2 The Tropospheric Ozone Budget

Due to its reactivity, ozone has a lifetime in the troposphere of around 22 days[35], though it varies strongly with location and season. The total global budget of ozone can be estimated by considering its major sources and sinks. The major sources are stratosphere-troposphere exchange (STE) and photochemical generation. The major pathways through which ozone is destroyed are photochemical destruction and dry deposition, with photochemistry being approximately 3 times that of deposition[36]. Estimates for the magnitude of each of these factors from the literature are given in Table 1.1.

Table 1.1: Estimated annual sources and losses of tropospheric ozone. All values given in Tg yr^{-1}

Reference	Exchange *	Chem. Production	Chem. Loss	Dry deposition
(Lelieveld & Dentener, 2000)[36]	+570	+3310	-3170	-710
(Bey et al., 2001)[37]	+470	+4900	-4300	-1070
(Sudo et al., 2002)[38]	+593	+4895	-4498	-990
(Horowitz et al., 2003)[39]	+340	+5260	-4750	-860
(von Kuhlmann et al., 2003)[40]	+540	+4560	-4290	-820
(Shindell et al., 2003)[41]	+417	-	-	-1470
(Park et al., 2004)[42]	+480	-	-	-1290
(Rotman et al., 2004)[43]	+660	-	-	-830
(Wong et al., 2004)[44]	+600	-	-	-1100
(Stevenson et al., 2004)[45]	+395	+4980	-4420	-950
(Wild et al., 2004)[46]	+520	+4090	-3850	-760
(Folberth et al., 2006)[47]	+715	+4436	-3890	-1261
(Stevenson et al., 2006)[48]	+520	+5060	-4560	-1010
(Huijnen 2010)[49]	+421	+4289	-3881	-829
(Kawase 2011)[50]	+560	+4876	-4520	-916
(Young et al. 2013)[51]	+477	+4877	-4260	-1094
(Hu et al. 2017)[52]	+325	+4960	-4360	-910
(Badia et al. 2021)[53]	-	+4742	-4250	-873
(Griffiths et al. 2021)[54]	-	+4510	-3948	-846

* **Net ozone transfer between the stratosphere and troposphere.**

STE is a collection of processes that leads to the movement of gases between the stratosphere and troposphere, which otherwise experience limited mixing due to the diminished temperature gradient at and above the tropopause. While this effects many gaseous species, it is particularly important for ozone due to its very high stratospheric concentrations relative to the troposphere below. STE can occur via a variety of mechanisms. On a global scale, STE occurs through the circulation of air rising near the equator and descending nearer the poles, known as Brewer-Dobson circulation. This brings high-ozone air from the stratosphere downwards into the troposphere in high-latitude regions over timescales of several months. In the absence of diabatic processes (the transfer of heat or mass), air parcels are bound to regions of constant potential temperature, or entropy, known as isentropic surfaces. These surfaces can span a range of altitudes; isentropic surfaces at high latitudes can span from the tropopause as far down as the planetary boundary layer, inputting high levels of ozone into

the troposphere at a level that can raise health concerns[55]. Tropopause folds are considered the dominant mechanism for intrusion of stratospheric air into the troposphere, particularly at mid-latitudes[56]. These are 'tongues' of air that develop near jet stream cores or large low-pressure systems (cut-off lows) with high ozone and low water content[57]. These intrusions can then dissipate into the troposphere by various mechanisms, leading to irreversible transfer for ozone on the timescale of the intrusion event[58,59].

The photochemical production of ozone in the troposphere is dictated by its interactions with NO_x, and in turn those of NO_x with CO and volatile organic compounds (VOCs). NO_2 is photolyzed to form O atoms which react rapidly with O_2 to form O_3. NO and O_3 also react with each other. In isolation, these reactions form a null cycle in which ozone is neither produced nor destroyed.

$$NO_2 + h\nu \rightarrow NO + O(^3P) \quad \text{(R4)}$$

$$O(^3P) + O_2 \rightarrow O_3 \quad \text{(R5)}$$

$$NO + O_3 \rightarrow NO_2 + O_2 \quad \text{(R6)}$$

In order for net production of O_3 to occur, an alternative method for the oxidation of NO to NO_2 is required that does not consume O_3. In the troposphere, this is achieved by peroxy radicals (HO_2 and RO_2 where R is an alkyl group), formed by the oxidation of CO and VOCs.

The OH present in the troposphere, produced by (R1+R3), oxidises CO to hydroperoxyl radicals (HO_2).

$$CO + OH \rightarrow CO_2 + H \quad \text{(R7)}$$

$$H + O_2 + M \rightarrow HO_2 + M \quad \text{(R8)}$$

In the absence of NO_x, HO_2 self-reacts to form hydrogen peroxide (H_2O_2), which can then either be lost via wet deposition, be photolyzed to OH, or regenerate HO_2.

$$2HO_2 \rightarrow H_2O_2 + O_2 \quad \text{(R9)}$$

$$H_2O_2 + h\nu \rightarrow 2OH \quad \text{(R10)}$$

$$H_2O_2 + OH \rightarrow HO_2 + O_2 \quad \text{(R11)}$$

In the presence of NO_x, HO_2 can instead react with NO to form NO_2.

$$HO_2 + NO \rightarrow OH + NO_2 \quad \text{(R12)}$$

The NO_2 formed by (R12) can then go on to form O_3 via (R4+R5), hence leading to the net formation of O_3 since the NO_2 itself was not formed by the ozone-consuming pathway (R6).

CH_4 can also act as a source of peroxy radicals in the troposphere, as can other VOCs which behave similarly. Isoprene is a particularly important example – its biogenic sources are sufficient to make ozone production NO_x limited outside of urban centres in the United States.[34]

$$CH_4 + OH \rightarrow CH_3 + H_2O \quad \text{(R13)}$$

$$CH_3 + O_2 + M \rightarrow CH_3O_2 + M \quad \text{(R14)}$$

The methyl peroxy radical CH_3O_2 formed in (R14) is analogous to the hydrogen peroxy radical HO_2 formed in (R11), able to react either with another peroxy radical similar to (R9), or with NO like in (R12).

$$CH_3O_2 + HO_2 \rightarrow CH_3OOH + O_2 \quad \text{(R15)}$$

$$CH_3O_2 + NO \rightarrow CH_3O + NO_2 \quad \text{(R16)}$$

Just like the reaction of HO_2 with NO in (R12), (R16) leads to net production O_3 via the reaction of NO_2 in (R4+R5). However, unlike the reactions of HO_2, both reaction of CH_3O_2 have products that can go on to form further peroxy radicals. In the case of (R15), methyl hydroperoxide (CH_3OOH) can either photolyse or react with OH similarly to H_2O_2 in (R10+R11). A significant difference however is that hydrogen abstraction can occur at two different places with CH_3OOH leading either to the formation of formaldehyde (CH_2O) or the regeneration of CH_3O_2.

$$CH_3OOH + OH \rightarrow CH_2O + OH + H_2O \quad \text{(R17)}$$

$$CH_3OOH + OH \rightarrow CH_3O_2 + H_2O \quad \text{(R18)}$$

$$CH_3OOH + h\nu \rightarrow CH_3O + OH \quad \text{(R19)}$$

The methoxy radical (CH_3O) formed in (R19) then quickly reacts with O_2 to form HO_2.

$$CH_3O + O_2 \rightarrow CH_2O + HO_2 \quad \text{(R20)}$$

This HO_2 then proceeds to reacts via the pathways shown in (R9+R12). Note however that since (R15) uses HO_2 in the formation of CH_3OOH, there is no net gain of HO_2 in this pathway at this point, and therefore no net ozone production from NO_2 formed in (R12). The CH_2O also undergoes either oxidation by OH or photolysis, with 2 possible photolysis routes.

$$CH_2O + OH \rightarrow CHO + H_2O \quad \text{(R21)}$$

$$CH_2O + O_2 + h\nu \rightarrow CHO + HO_2 \quad \text{(R22)}$$

$$CH_2O + h\nu \rightarrow CO + H_2 \quad \text{(R23)}$$

The formyl radicals (CHO) produced by (R21+R22) then react with O_2.

$$CHO + O_2 \rightarrow CO + HO_2 \quad \text{(R24)}$$

CO can then continue to react to form one further HO_2 radical via (R7+R8). It is therefore possible for the ozone production from a single molecule of methane to vary greatly according to the concentration of NO_x and the pathways through which the methane and its produces react. The most extreme case requires high NO_x, that the methane reaction proceeds entirely via the reaction route (R13+R14+R16+R20+R22+R24), that all of the resulting CO reacts fully through (R7+R8), and that all HO_2 radicals form NO_2 via (R12). In this case, a single methane molecule can cause the net production of 5 molecules of ozone.

$$CH_4 + 10O_2 \rightarrow CO_2 + H_2O + 5O_3 + 2OH$$

In the opposite extreme with zero NO_x following (R13+R14+R15+R17+R21) and subsequent self-reaction of the single HO_2 produced in the pathway via (R9), no ozone at all would be produced.

$$2CH_4 + 3O_2 + 6OH \rightarrow 6H_2O + 2CO_2 + H_2O_2$$

The relative concentrations of both NO_x and VOCs are therefore hugely important in defining the photochemical production of tropospheric ozone. The presence of these gases in the atmosphere is partially due to natural sources; NO_x is generated by microbial action in soils, oxidation of biogenic ammonia, wildfires, and lightning. Meanwhile VOCs are emitted from trees, biomass decomposition as well as plant and animal respiration. Anthropogenic sources of these species can lead to increased ozone production above what is natural. Fossil fuel combustion is a huge source of both NO_x and VOCs. Biomass burning also plays a role, as do VOCs released from many consumer products.

This production of ozone within the troposphere is partially balanced by its loss mechanisms. The first major route for ozone loss is the photochemical production of OH outlined in (R1-R3). In remote parts of the troposphere away from anthropogenic influence, it can also be destroyed though reaction with OH and HO_2.

$$O_3 + HO_2 \rightarrow OH + 2O_2 \quad \text{(R25)}$$

$$O_3 + OH \rightarrow HO_2 + O_2 \quad \text{(R26)}$$

Though both photochemical production and loss are estimated to be large, the overall photochemistry of ozone in the troposphere is estimated to be a source to the ozone budget. Together with STE, these production terms are balanced by the remaining pathway for tropospheric ozone loss – dry deposition of ozone to the Earth's surface.

1.3 Dry Deposition

Dry deposition is the process by which a chemical species or particle is removed from the atmosphere via downward transport (gravity or turbulence) and subsequent reaction at the surface. It is typically considered distinct from wet deposition, in which a species relies upon dissolution in precipitation for its downward transport. Due to its sparing solubility in water, dry deposition is the dominant mechanism for ozone. Measurements and models of dry deposition typically report deposition in terms of a deposition velocity (v_d), with units of cm s^{-1} or mm s^{-1} depending on magnitude or preference. It can be thought of as the average downwards velocity of a particle or molecule and is closely to mass flux – the mass passing through a unit area per unit of time.

$$F = v_d \times C \tag{1}$$

Strictly C is the concentration difference across the boundary. However due to ozone's high reactivity and low solubility, its concentration in water is taken to be 0, and hence C is simply the atmospheric concentration. In order to calculate a deposition velocity, most models use a 'resistance in series' approach, akin to Ohms law in electronics.

$$v_d = \frac{1}{R_a + R_b + R_c} \tag{2}$$

Each resistance term represents sequential parts of the deposition pathway, and each have their own parameterisations. R_a represents aerodynamic resistance in the air above a surface and is independent of chemical species. R_b represents the resistance of moving through the quasi-laminar layer of air immediately above a surface, and therefore depends on a substance's diffusivity. Lastly, R_c denotes the total surface resistance for which parameterisations vary greatly depending on the application. For example, deposition in a forest environment may divide R_c up into branching paths of resistances for uptake by plant stomata and cuticles, canopy effects, and uptake to underlying soils and water[60]. For oceanic deposition however, a single surface resistance term is typically used. It is worth noting that

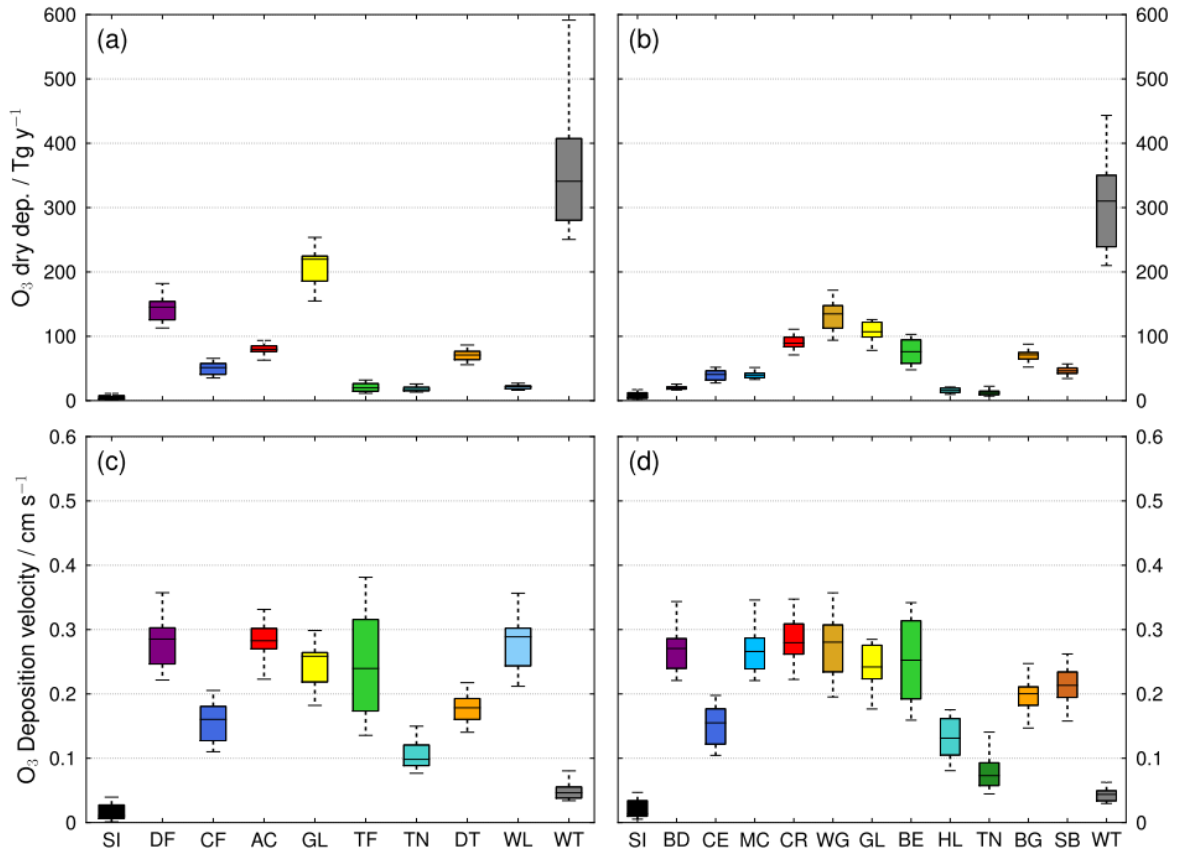

Figure 1.3: Global total deposition (a and b) and deposition velocity (c and d) of ozone to different land classes predicted from 2 datasets – 'OW11' (a and c) and 'GLCF' (b and d) – from Hardacre et al. (2016). SI = snow and ice, DF = deciduous forest, CF = coniferous forest, AC = agricultural and crops, GL = grassland, TF = tropical forest, TN = tundra, DT = desert, WL = wetland, WT = water, BD = broadleaf deciduous forest, CE = coniferous evergreen forest, MC = mixed coniferous forest and woodland, CR = cropland, WG = wooded grassland, BE = broadleaf evergreen forest, HL = high-latitude deciduous forest, BG = bare ground, SB = shrubs on bare ground. From Hardacre et al. (2015)

Eq. 2 sometimes appears with a gravitational settling term added on the right-hand side. This is important for work with aerosols and particles[61], but is assumed to be zero when working with molecular deposition due to their negligible weight.

The value of R_c, and hence v_d, for ozone varies greatly depending on the terrain over which deposition is considered[62]. Typically, surfaces with much vegetation result in greater ozone deposition than those without[60]. This is partially due to stomatal uptake, accounting for roughly 30-40% of deposition over vegetation[63,64], though it varies greatly with humidity and temperature[63,65]. While non-stomatal uptake was for a time assumed to be constant, it was later shown to be otherwise; uptake to soil has been shown to vary with organic content and porosity, being especially important in arid regions[66,67]. In contrast, the ocean environment is largely agreed to yield some of the lowest deposition velocities of any surface (see Figure 1.3), with R_c typically accounting for ~95% of the total resistance[68,69]. As such, oceanic deposition velocity is sometimes approximated to the inverse of R_c. This surface resistance term is determined by a few factors. Since significant deposition is observed even in the

absence of any air or waterside turbulence, chemical reaction is established as an important factor. The reaction of ozone with iodide at the sea surface is a key part of this[70], and efforts have been made to determine rate constant of this reaction for use in models[70–73]. Dissolved organic carbon (DOC) has been suggested to be of similar importance to ozone reactivity as iodide[74], and surfactants at the sea surface microlayer (SML) have also been indicated to play a role[69,75]. In addition to chemical reactivity, oceanic turbulent mixing is thought to enhance ozone deposition[76]. A dependence on wind-induced turbulence has also been observed in a number of studies[69,77,78], though a strong correlation is not consistently present (e.g. in the open ocean eddy covariance measurements of Helmig at al.)[79]. Though the magnitude of oceanic ozone deposition velocity is small in relation to other land classes, the large surface area covered by oceans means that it contributes the greatest amount to the global deposition sink, with variability regarding the total mass stemming from differences in ozone concentrations within different models. Crucially, past models have commonly used a fixed surface resistance value of 2000 s m^{-1}.[80–84] As such, a better understanding of how physical and chemical processes affect surface resistance could significantly improve models of the tropospheric ozone budget.

Aside from the immediate destruction of ozone, the reactions of ozone with iodide at the sea surface are also the dominant source of global iodine emissions[85–87], with further implications for atmospheric chemistry. Organic iodine compounds from biological sources also contribute to atmospheric iodine, but minorly compared with the inorganic fraction[88].

$$I^-_{(aq)} + O_{3(aq\ or\ g)} \rightarrow IOO^-_{(aq)} \quad \text{(R27)}$$

$$IOO^-_{(aq)} \rightarrow IO^-_{(aq)} + O_{2(g)} \quad \text{(R28)}$$

$$IO^-_{(aq)} + H^+_{(aq)} \rightarrow HOI_{(aq)} \quad \text{(R29)}$$

$$HOI_{(aq)} + H^+_{(aq)} + I^-_{(aq)} \rightarrow I_{2(aq)} + H_2O \quad \text{(R30)}$$

$$I_{2(aq)} \rightarrow I_{2(g)} \quad \text{(R31)}$$

$$HOI_{(aq)} \rightarrow HOI_{(g)} \quad \text{(R32)}$$

HOI is thought to be the major inorganic iodide portion, with emissions of HOI and I_2 estimated as 100-250 nmol m^{-2} d^{-1} and 2-10 nmol m^{-2} d^{-1} respectively[86]. These gaseous compounds then have important consequences for tropospheric chemistry; not only are they significant sources of aerosols[89–91], they also lead to destruction of ozone in the troposphere, and even the stratosphere[92]. Globally, the inclusion of iodine chemistry in models leads to approximately a 15% reduction in tropospheric ozone[89,93], and reduces ozone exposure in the summer in Europe by 15%[94]. Furthermore, observations in a tropical marine environment suggested a 50% increase in ozone loss compared with

the GEOS-CHEM model without halogen chemistry[95]. This then acts as a negative feedback mechanism, acting as a buffer against increasing tropospheric ozone; as ozone rises, so do iodine emissions from the sea, which in turn promote the loss of tropospheric ozone[96].

A number of studies have found the presence of organic material to affect iodine emissions, though a consistent effect is not yet apparent. Observations of supressed iodine emissions were reasoned to be a consequence of the physical effects of organic material inhibiting the emission of iodine[97,98]. However there is some evidence that certain compounds such as acids may individually enhance emission by acting as a source of H^+ for the reactions (R29+R30)[99,100].

The organic compounds themselves are also candidates for emission and subsequent feedback cycles with ozone. Fatty acids in particular have been shown to emit aldehydes upon exposure to ozone[101,102], and the complex mixture of organics present in seawater likely contains other reactive compounds. Given the importance of VOCs in the formation of tropospheric ozone (Section 1.2), this could be an important consideration in modelling tropospheric ozone, though more work is needed to establish the magnitude of any effect.

1.4 The Sea Surface Microlayer (SML)

Key to understanding the deposition of ozone to the ocean is the sea surface microlayer – generally referring to the top few 100 µm of the ocean. This layer constitutes the boundary between the air and the sea, and shows notable physical and chemical differences from the water below[103]. It is possible for a visible film to form at the ocean surface where concentrations of insoluble surfactants are sufficiently high. These appear as regions of very still, flat surface water due to capillary wave dampening. This effect is attributed to the formation of a monolayer of surfactants, only 2-3 nm thick[104] (see Figure 1.4) and can dampen the air-sea exchange of gas, heat, and momentum[105]. These natural, visible slicks are only maintained at low (<5 m s^{-1}) wind speeds, though there is evidence for artificial slicks persisting at higher (~13 m s^{-1}) wind speeds[106]. This is an important distinction from the deeper SML, which shows enrichment in organic material that persists at typical global average wind speeds (6.6 m s^{-1}) and even up to 10 m s^{-1} wind speeds[107–109]. Air-sea exchange is driven both by turbulent and molecular diffusion. The former operates at a scale defined by the turbulent eddies in the air and in the water, whereas the latter operates on the scale of the SML in which turbulent eddies are surpressed[110]. This layer in which molecular diffusion dominated over turbulence is sometimes referred to as the 'diffusive sublayer' of the SML. Transfer on each side of the boundary is defined by transport rates for air and water, k_a and k_w respectively. However, for sparingly soluble gases such as ozone, only k_w is significant[111,112]. Due to this dependence upon both turbulence and diffusivity, the enrichment of surfactant molecules within the SML can affect k_w in two main ways: as a

physiochemical barrier, and by inhibiting turbulent energy transfer. Though visible slicks formed by high concentrations of hydrophobic surfactants would intuitively have great impact, their dispersion at modest winds speeds means that it is the hydrophilic surfactants that exists deeper within the SML that are considered most important for air-sea exchange globally[113].

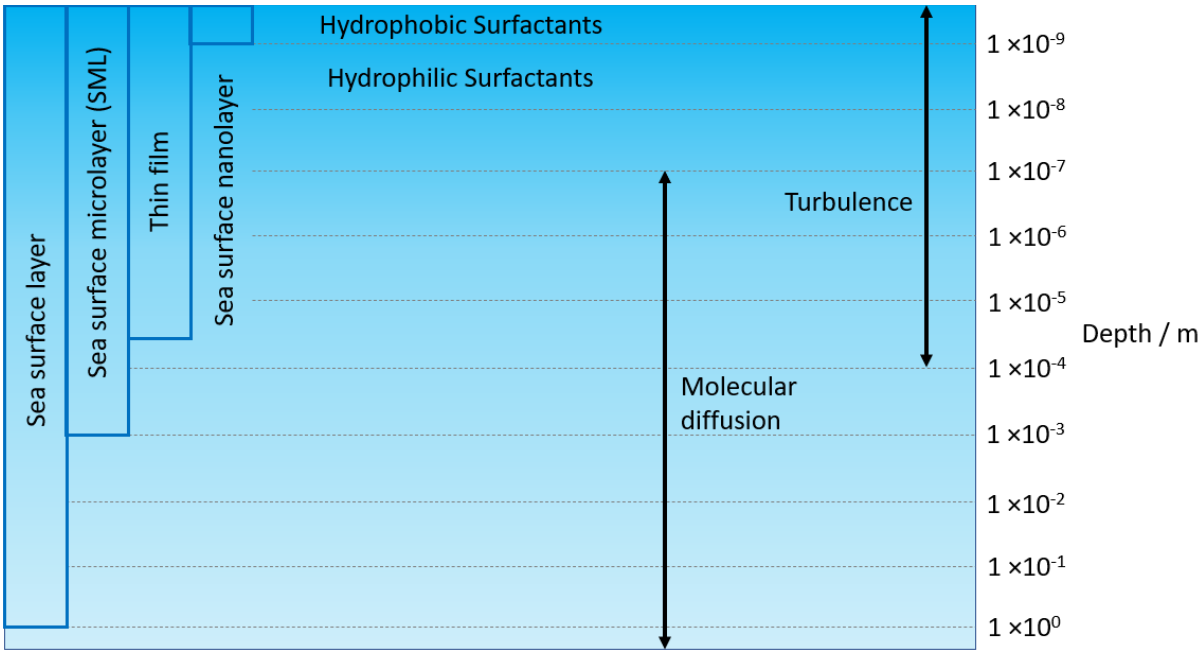

Figure 1.4: The structure of the sea surface microlayer, adapted from Hardy: The Sea Surface and Global Change; Liss, P. S., Duce, R. A., Eds.; Cambridge University Press: Cambridge, U.K., 1997

In the case of ozone, chemical reactivity means that surfactants and other organic species lead to overall enhanced deposition, contrary to their physical dampening effects[69,75]. For example, ozone has been shown to react with chlorophyll[114] and polyunsaturated fatty acids (PUFAs)[102,115–117]. This potentially explains the observation that the reaction of ozone with DOC is of comparable size to that with iodide[74]. That is not to say that the physical effects of surfactants are not relevant; there is evidence for the presence of DOC enhancing deposition overall, but weaking the significance of the ozone-iodide reaction by as much as 50% at typical oceanic concentrations[97]. This therefore has consequences for the assumption that chemical reactivity of individual species can be used additively in parameterisations of surface resistance[69].

Iodine exists in surface water in two major forms: iodide (I^-) and iodate (IO_3^-)[111]. While the sum concentration of inorganic iodide is roughly constant throughout the surface ocean (~500 nmol dm^{-3})[118–120], the ratio of I^- to IO_3^- varies with depth and location. Since IO_3^- is understood to be the more thermodynamically stable form in seawater[121], it is most abundant throughout the water column with only few nmol dm^{-3} at depth. Despite this, the top ~100 m of the water column regularly show much higher I^- in the region of 100 nmol dm^{-3}, particularly at mid-low lattitudes[122]. This sustained apparent disequilibrium is thought to be driven by biological processes in the upper ocean[120]. This is not fully established, but is supported through experimental observations of an anticorrelation of

iodide with nitrate (NO_3^-)[119,123,124] and subsequent uses of this relationship in models[122,125]. It remains unclear though whether any additional enrichment is present specifically in the SML compared with the water immediately below it[126]. In addition to these depth and latitudinal trends, there is also evidence for I^- speciation to be greater in coastal waters than would be expected from latitude alone[122,127–129], again possibly due to increased biological activity.

1.5 Previous Measurements of Deposition Velocity

Early observations of ozone deposition used large boxes coated in material inert to ozone with a single open face placed on the surface of interest. Ozone would then be supplied to the enclosure and its decay measured[130]. The air within the box could also be agitated in an attempt to mimic atmospheric turbulence. An estimate of R_a within the enclosure could be established by using an artificial surface with such high reactivity, that R_c is effectively zero (e.g. 0.02 mol dm^{-3} KI solution)[131]. Limitations of this approach include the inability of a small enclosure to fully recreate atmospheric turbulence, and the difficulty of creating a surface reactive enough for R_c and R_a to be fully separated. Nevertheless, these works contributed some of the first experimental estimates of the deposition to water: a surface resistance of 1000 s m^{-1}, corresponding to a deposition velocity of 0.1 cm s^{-1} - one of the higher estimations to date.

Table 1.2: Literature reported values of oceanic ozone deposition velocity

Study Number	Technique	v_d / cm s^{-1}	Reference
1	Box Enclosure Decay	0.03 – 0.04	(Aldaz, 1969)[130]
2	Profile Measurements	0.008 – 0.017	(Tiefenau & Fabian, 1972)[132]
3	Wind Tunnel	0.04	(Garland & Penkett, 1976)[133]
4	Box Enclosure Decay	0.025 – 0.09	(Galbally & Roy, 1980)[131]
5*	Tower EC	0.01	(Wesely et al., 1981)[134]
6	Aircraft EC	0.056	(Lenschow et al., 1982)[68]
7	Aircraft EC	0.024	(Kawa & Pearson, 1989)[135]
8†	Static Chamber	0.006 – 0.014	(McKay et al., 1992)[75]
9	Budget	0.03	(Heikes et al., 1996)[136]
10	Literature Review	0.01 – 0.05	(Wesely, 2000)[60]
11	Tower EC	0.148	(Gallagher et al., 2001)[77]
12‡	Tower EC	0.02 – 0.04	(Whitehead et al., 2009)[137]
13	Tower EC	0.025	(McVeigh et al., 2010)[138]
14	Ship EC	0.009 – 0.034	(Helmig et al., 2012)[79]
15	Tower EC	0.013	(Novak et al, 2020)[139]

***Fresh water, Lake Michigan. †Fresh water and humic acid. All other values represent sea water. ‡ High tide values only**

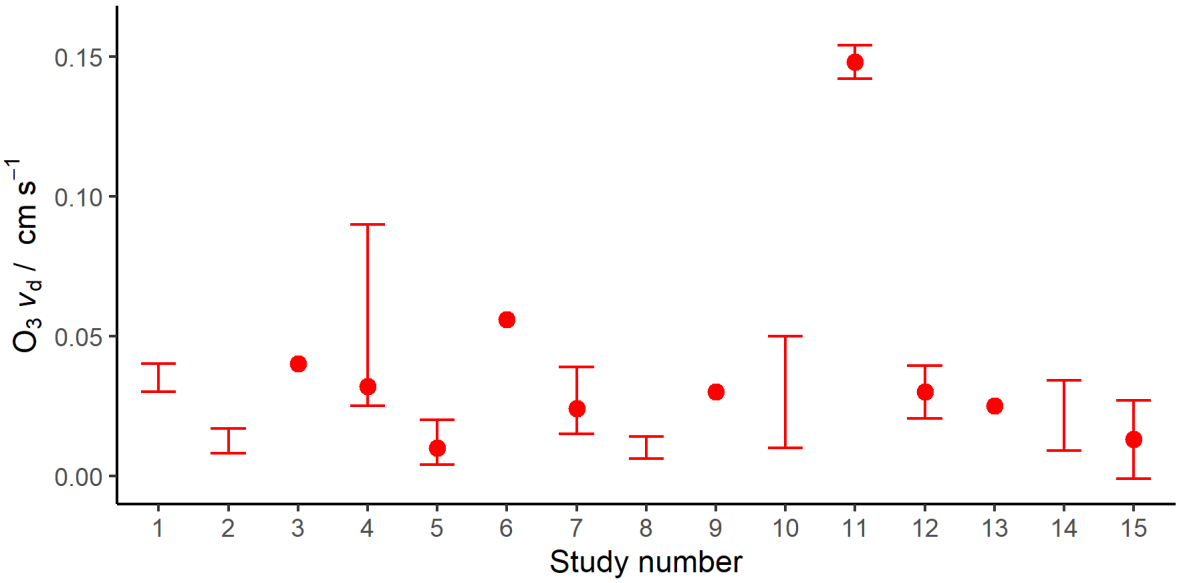

Figure 1.5: Graphical representation of determined v_d across a range of studies. Reference numbers given in Table 1.2. Plotted as the average and range reported in the literature. Studies 11 and 12 reports a standard error rather than a range. A range is reported in study 13, but as that of individual flux periods – the resulting large range (-0.294 to 0.893) is not plotted.

In recent years, eddy covariance (EC) has become the preferred method for measuring fluxes and, by extension, deposition velocities. This is due to the method providing observations of the natural environment itself rather than a simulation in the lab. The technique relies upon the rapid measurement of both vertical wind and the scalar of interest (ozone in this case, though the method is commonly applied to heat and momentum) and is discussed further in Section 1.6. Coastal observatories provide convenient locations for the running of these measurements, provided they are sufficiently close to the shore. Such measurements have been conducted on the north Norfolk coast (UK)[77], west Ireland[138], and north-west France[137]. These studies respectively determined v_d to be 0.148 cm s^{-1}, 0.025 cm s^{-1} and 0.03-0.21 cm s^{-1}, with the latter range from Whitehead et al. owing to low tide exposing the seabed for as far as 3 km away from the tower location. All of these measurements used detectors relying on the chemiluminescent reaction of ozone with a silica gel disk impregnated with a reactive coumarin-47 dye solution. The resulting light is then detected through use of a photo-multiplier tube (PMT)[137]. Although also working on the principle of chemiluminescent detection, the instruments used in the work presented utilise the light produced from the gas-phase reaction of O_3 with NO. This avoids the necessity of long periods of instrument conditioning and regular replacement of spent disks. O_3-NO instruments are discussed further in Section 2.2.

This type of gas-phase chemiluminescence instrument was used in 5 ship-borne EC measurements, representing the largest collection of in-situ ozone flux measurements to date[79,140]. The cruises observed v_d values of 0.009 – 0.034 cm s^{-1}, with sea surface temperature (SST) determined to be the best predictor. It was also noted that measured v_d values increased by an order of magnitude during the TexAQS cruise when coastal/land regions were measured, highlighting the important of careful analysis of land-based results in particular.

Chemiluminescence detectors are not the only option for O_3 flux measurements – the EC method works with any detection method with the capacity to resolve measurements several times per second. Chemical ionisation mass spectrometry (CIMS) has recently been used for this purpose in the work of Novak et al. to measure a v_d of 0.013 cm s^{-1} from a pier in the California, USA[139]. Such instrumentation could stand to greatly reduce the uncertainty inherent to much of the work to date.

1.6 Eddy Covariance (EC) Theory

Eddy covariance (EC) is a measurement technique for determining the flux of some scalar via measurement of that scalar and the vertical wind at a high enough frequency to resolve small, high frequency eddies within the atmosphere. Essentially, it is required to know at any given point in time how much of the relevant scalar is moving up or down, and at what velocity. Much work focused on widespread measurements of CO_2 and water vapour fluxes[141], though with the ubiquitous availability of high-frequency anemometers, an increasing number of trace gases can now be observed.

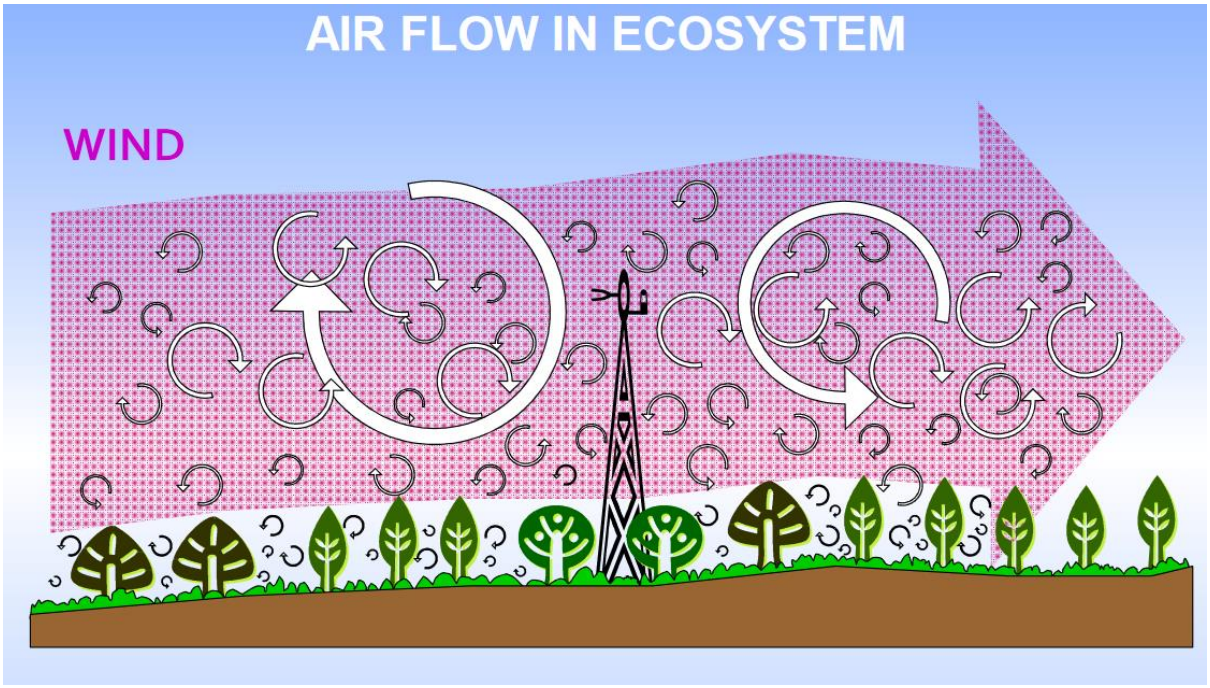

Figure 1.6: Turbulent eddies in the atmosphere from 'A Brief Practical guide to Eddy Covariance' – LICOR: https://www.licor.com/env/pdf/eddy_covariance/Brief_Intro_Eddy_Covariance.pdf

The flux of a given gas is mathematically represented by the mean of the product of the density of air (ρ_a), the mixing ratio of the species of interest (s), and vertical wind speed (w).

$$F = \overline{\rho_a w s} \tag{3}$$

Each term in Eq. 3 can then be broken down via Reynolds decomposition to be presented as a mean over some time and an instantaneous deviation from that mean.

$$F = \overline{(\overline{\rho_a} + \rho_a')(\overline{w} + w')(\overline{s} + s')} \tag{4}$$

$$F = \overline{(\overline{\rho_a}\,\overline{w}\,\overline{s}) + (\overline{\rho_a}\,\overline{w}\,s') + (\overline{\rho_a}\,w'\,\overline{s}) + (\overline{\rho_a}\,w's') + (\rho_a'\,\overline{w}\,\overline{s}) + (\rho_a'\,\overline{w}\,s') + (\rho_a'\,w'\,\overline{s}) + (\rho_a'\,w's')} \tag{5}$$

The second, third and fifth terms on the right-hand side of Eq. 5 will be equal to zero (as each has precisely one deviation term, and the mean of the deviation from the mean will be 0 by definition).

$$F = \overline{(\overline{\rho_a}\,\overline{w}\,\overline{s}) + (\overline{\rho_a}\,w's') + (\rho_a'\,\overline{w}\,s') + (\rho_a'\,w'\,\overline{s})(+\rho_a'\,w's')} \quad (6)$$

Here, important assumptions are made. Assuming fluctuations in air density to be negligible ($\rho_a' = 0$) removes terms 3,4, and 5 from Eq. 6. Lastly, mean vertical wind flow ($\overline{w}$) is assumed to be zero, removing the 1st term and leaving the recognised expression for eddy covariance from where its name derives.

$$F = \overline{\rho_a}\,\overline{w's'} \quad (7)$$

A further assumption is sometimes necessary: that the product of mean air density and the covariance of vertical wind deviations and mixing ratio deviations is equal to the covariance of vertical wind deviations and the density of the gas being studied. This is not necessary for instruments capable of measuring mixing ratios, however.

These assumptions are typically considered valid over ideal, flat, homogeneous terrain. Since many surfaces of interest are less than 'ideal', corrections to account for the inaccuracy of these assumptions can be necessary. For instance, the assumption that mean vertical windspeed in zero is regularly untrue in uneven or sloped terrain. As such, it is common to adjust the co-ordinate system from the anemometer defaults to make this true. Double rotation[142] is a common method in which wind component *u* (positive west-to-east), *v* (positive south-to-north) and *w* (positive upwards) are first rotated about *w* into the mean wind such that the mean of the newly defined *v'* over the averaging period becomes zero. The second rotation is then applied about *v*' until the original *w* component is positioned such that it now averages 0 as required. In this way, winds with non-zero *w* and the effects of uneven anemometer placement are alleviated.

An alternative method – planar fit[143] – uses a long period (typically several days) of wind data from a fixed anemometer to adjust the co-ordinates according to the mean wind profile of a site. This alleviates the issue of very low wind speeds leading to questionable double rotation angles. However, it is typically necessary to apply different rotations in different wind sectors in heterogeneous terrain (e.g. for every 10° sector)[144,145]. This therefore leads to discontinuity in the treatment of wind data at sector boundaries. A proposed method for dealing with this is defining tilt angles as a continuous function of wind direction[146], though this approach is not yet widely used.

Several other adjustments are necessary for appropriate quality control. For detectors requiring gas sample lines, concentration data are inevitably logged with a time delay relative to the relevant wind data, and as such with need realigning. Further filters ensuring reasonable stationarity (no large changes in relevant atmospheric properties, concentrations etc.) and turbulence development are also commonplace, and will be discussed further in Sections 2.4 and 2.5.

1.7 Aims of This Work

Dry deposition of ozone is a crucial element in accurately modelling tropospheric ozone, with oceanic deposition contributing both the single biggest sink and uncertainty of any land class. As such, a better understanding of ozone deposition and reactivity at the sea surface would be greatly beneficial. The work presented here aims to work towards this better understanding by adding to the limited number of ozone eddy covariance methods, linking these with biogeochemical parameters in the ocean surface, and investigating the composition of DOC within the sea-surface microlayer.

Chapter 2 focuses on the flux site, instrumentation, and method specifics. Intermittent timeseries over the course of 3 years are presented and their sources of error and uncertainty interrogated. Chapter 3 explores several biogeochemical aspects of the SML at the field site, measured concurrently with the EC measurements. These parameters, along with meteorology are then used to compare existing ozone models with our experimental results, focusing on the influence of iodide, DOC, and wind speed. Chapter 4 discusses mass-spectrometric analysis of DOC composition within the SML, its changing composition and its effects on ozone.

2. Eddy Covariance Measurements at Penlee Point

2.1 Fieldwork and Site Information

The Penlee Point Atmospheric Observatory (PPAO) is located on a headland on the south-west coast of the UK (50° 19.08' N, 4° 11.35' W), and experiences frequent winds with an oceanic fetch from the south-west making it excellently situated for the observation of air-sea interactions. The building itself is positioned 11 m above mean sea level, and approximately 30-60 meters from the water's edge, depending on tide. An extendable mast on the roof allows for a more elevated sample line 19 m above sea level, which was used for the duration of this work. Due north of the PPAO follows the coastline, with Plymouth Sound to the north-east. Locally, the headland on which the PPAO is built extends about 100 m further to the south-east in the form of a rocky outcrop. The extent of this rocky shoreline lessens towards the south and south-west, where wind is brought in from the English Channel. Moving further around the compass, the shoreline is met again running in a westerly direction. Finally, the north-west sector faces inland up a steep slope from which the site is accessed.

Figure 2.1: The location and local geography of the PPAO. © Google Earth.

As is common in the UK, the PPAO experiences predominantly south-westerly and northerly winds. Figure 2.2 shows the direction, speeds, and frequency of winds at the site from 10th April until 21st May 2018 and is typical for the site. It is clear that opportunities to measure fluxes over the north-west and south-east sectors are infrequent. The land to the north-west is in any case not of interest for measuring ozone deposition to water and would not provide quality flux data over vegetation regardless due to the steep slope causing the land to quickly rise above our observation point. To the south-east, the extension of the rocky outcrop, in combination with almost exclusively low wind

speeds, means there is not a reliably clean marine signature. Wind from the north-east is more commonly observed, but mostly arrives along the coastline, again raising the issue of observing the land more than the sea. The extent of this effect and decisions surrounding data filtering are discussed further in Sections. 2.5 and 2.6. As such, the south-westerly sector is the focus of this work, due to frequent observations of a range of wind speeds with minimal space between the tower and the sea.

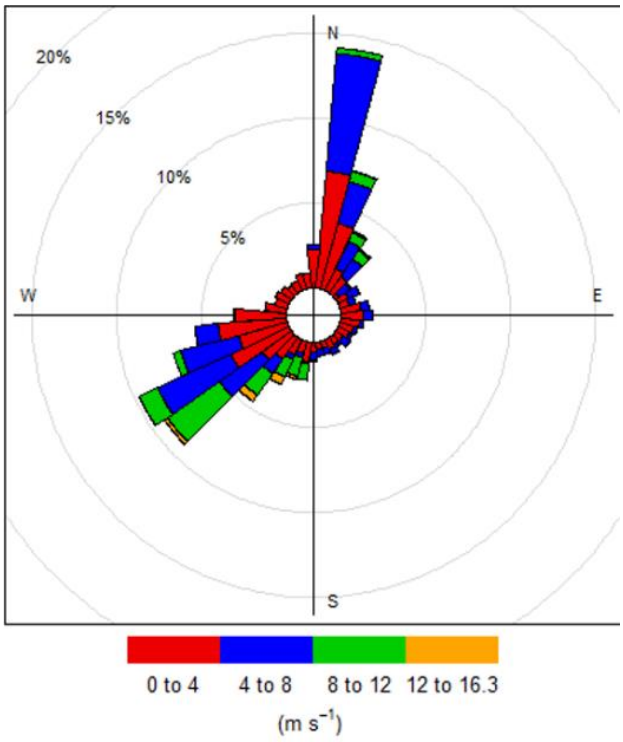

Figure 2.2: Wind directions and speeds at the PPAO from 10th April – 21st May 2018. Radial percentage values indicate the portion of all observed wind that fell within a given sector.

Fieldwork was conducted at the PPAO intermittently from April 2018 onwards, and is due to conclude in September 2021. In this chapter, fieldwork is considered in three periods: deployment 1 (10th April 2018 – 21st May 2018), deployment 2 (10th December 2019 – 31st August 2020) and deployment 3 (20th February 2021 onwards). This is due to instrumentation at the site being altered over the course of the project.

During deployment 1, high frequency ozone measurements (10 Hz) were taken using an Ecophysics CLD86 NO_x detector adapted to detect ozone (CLD86). Wind was also measured at 10 Hz using a Gill WindMaster Pro sonic anemometer, located within centimetres of sample line at the top of the mast - 19 m above mean sea level. A reported hardware bug with this model means a correction to the vertical wind component was applied: +16.6% and +28.9% in magnitude for positive and negative values respectively (http://gillinstruments.com/data/manuals/KN1509_WindMaster_WBug_info.pdf). Also on the roof of the observatory was a Gill MetPak Pro recording humidity, air temperature and

pressure at a lower frequency of 0.25 Hz. A calibrated 2B model 205 dual beam ozone monitor was used as a calibration for the CLD86 to account for any drift in sensitivity. A vacuum pump was used to draw sample air from the top of the mast to the CLD86 through ~10 m of 3/8'' PFA tubing at 13.5 L min^{-1}. This allowed for the retention of turbulent structure within the main sample line, with a Reynolds number of ~3000. An internal pump within the CLD86 then drew ~300 mL off this main sample line, through 1.5 m of 1/8'' PFA tubing. This included a tee to a charcoal filter (open to indoor air) to provide zeroes, and a dryer consisting of 60 cm of Nafion™ tubing coiled within indicating Drierite desiccant. The CLD86 also requires a supply of NO (2% in nitrogen), which was housed on the roof of the observatory and supplied at 1.5 bar at 50 mL min^{-1}, controlled by a critical orifice.

The fundamental nature of this set-up remained consistent across each deployment, though some elements changed. During deployment 2, the same CLD86 instrument was used, though it was operating at approximately a third of the sensitivity seen in 2018. Additionally, the calibration instrument was upgraded from the 2B dual beam instrument to a Thermo 49i, and the WindMaster Pro anemometer replaced with a R3-50, logging wind at 20 Hz (no longer requiring a correction to the vertical wind component). For convenience, the NO supply to the CLD86 was also altered using a mass flow controller (MFC) to provide 5 mL min^{-1} of 10% NO. This allowed for a sufficient total NO flow to the instrument while greatly reducing the time and expense of supplying fresh cylinders to the site.

Deployment 3 varied from deployment 2 mainly in the substitution of the CLD86 for a newer, more sensitive instrument from Air Quality Designs (AQD). Higher flow rates (1 L min^{-1} sample, 20 mL min^{-1} 10% NO) were necessary, and therefore the dryer was upgraded to a 48'' long, ¼'' diameter counterflow Nafion™ using indoor air passed through molecular sieves as the counterflow at 2.5 L min^{-1} to handle this increased flow. The charcoal zero set-up was also removed due to more convenient zeroing options being available with the AQD. Details of the chemiluminescent detectors are presented in the following section.

Table 2.1: Instrumentation used during 3 deployments at the PPAO.

Deployment	Dates	High-frequency ozone instrument	Ozone comparison instrument	Sonic anemometer
1	2018-04-10 – 2018-05-21	Ecophysics CLD86	2B 205	WindMaster Pro
2	2019-12-10 – 2020-08-31	Ecophysics CLD86	Thermo 49i	R3-50
3	2021-02-20 onwards	AQD	Thermo 49i	R3-50

2.2 Chemiluminescent Ozone Detectors

The CLD86 ozone detector was adapted from an Ecophysics CLD86 NO_x analyser since the principle of detection in each case is the same. The reaction of NO with O_3 can form NO_2 in an excited state, which can proceed to emit a photon in the wavelength range 600-3000 nm, with a maximum intensity at ~1200 nm[147,148]. This signal can then be detected with a photomultiplier tube (PMT). In its original incarnation as a NO_x instrument, the CLD86 included an internal ozone generator to produce high concentrations of O_3, far in excess of ambient NO_x concentrations. This therefore made NO the limiting reagent in the formation of excited state NO_2, making the detected light proportional to the NO concentration. The detection of NO_2 itself required prior conversion of NO_2 to NO through a high temperature converter. Therefore, the adaptation to an ozone detector presents some simplification over the original design, in that NO_2 conversion in not needed, nor is a source of ozone. Instead, an external NO supply is used (in this case recommended 1-2% NO in N_2 at 50 mL min^{-1}) to make ozone the limiting reagent, and hence the PMT signal proportional to ozone. A schematic for the CLD86 is shown in Figure 2.3. The internal pump draws ~300 mL min^{-1} of sample air and 50 mL min^{-1} of 2% NO at 1.5 bar, both controlled by critical orifices. These two gas streams are mixed immediately prior to entering the reaction chamber, in which the resulting chemiluminescence is observed by the PMT. The chamber is kept at low pressure (26 bar) and constant temperature (45 °C), while the PMT itself is cooled to -5 °C with a Peltier cooler to reduce dark counts resulting from thermal activity. To avoid any moisture build-up and freezing around the PMT, it is supplied with a constant stream of air, dried by a pressure difference across a Nafion™ membrane.

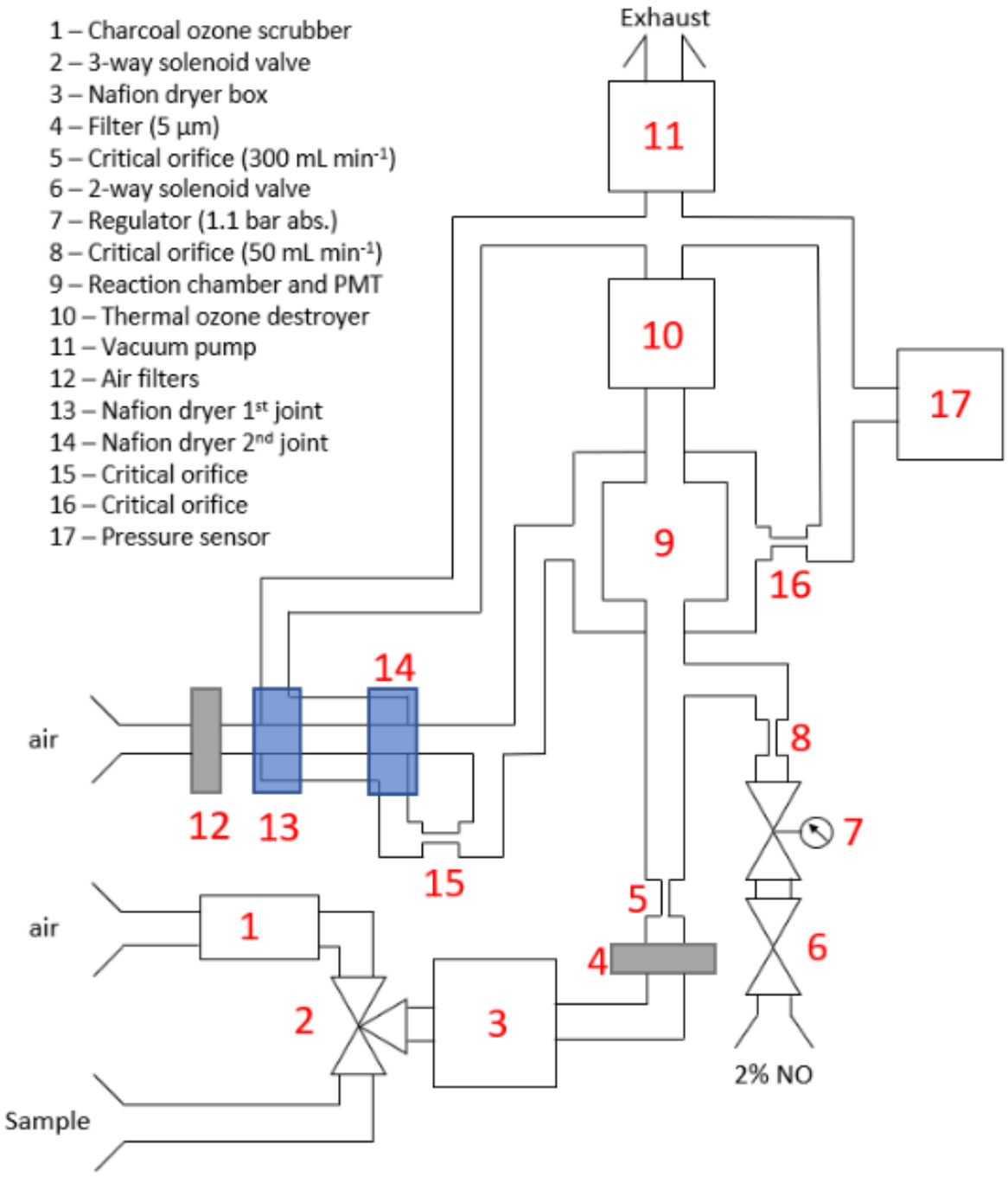

Figure 2.3: Schematic for the CLD86 high frequency ozone detector. The scrubber and dryer (parts 1-3) were made and housed separately from the main instrument.

An important feature of instruments for eddy covariance is their capability to not simply report high frequency concentration values (derived from photon 'counts'), but for these values to be physically distinct. That is to say, the volume of air being observed is different for each recorded value, else the high frequency values are merely (partially) the same observation repeated. Therefore, it is necessary for the residence time within the detection chamber to be suitably low, < 0.1 s for a 10 Hz measurement. In the default set-up for the CLD86, the fixed pressure, flow, temperature, and cell

volume (14 cm³) result in a residence time of 0.062 s, lower than the 0.1 s required for distinct 10 Hz measurements.

Dark counts were measured for the CLD86 by scrubbing ozone in the sample air with a charcoal filter. This yielded dark counts of 480 counts s^{-1}. The instrument sensitivity was 240 counts $ppbv^{-1}$ s^{-1}, determined by comparison to a calibrated 2B model 205 dual beam ozone detector. Figure 2.4 shows the level of agreement between the two instruments for the duration of deployment 1. It also shows no apparent correlation of sensitivity with ambient humidity, providing evidence for the efficacy of the dryer. At 10 Hz, counts during the zero measurement had a standard deviation of 4 counts, corresponding to a mixing ratio 1σ value (via the sensitivity) of 0.167 ppbv.

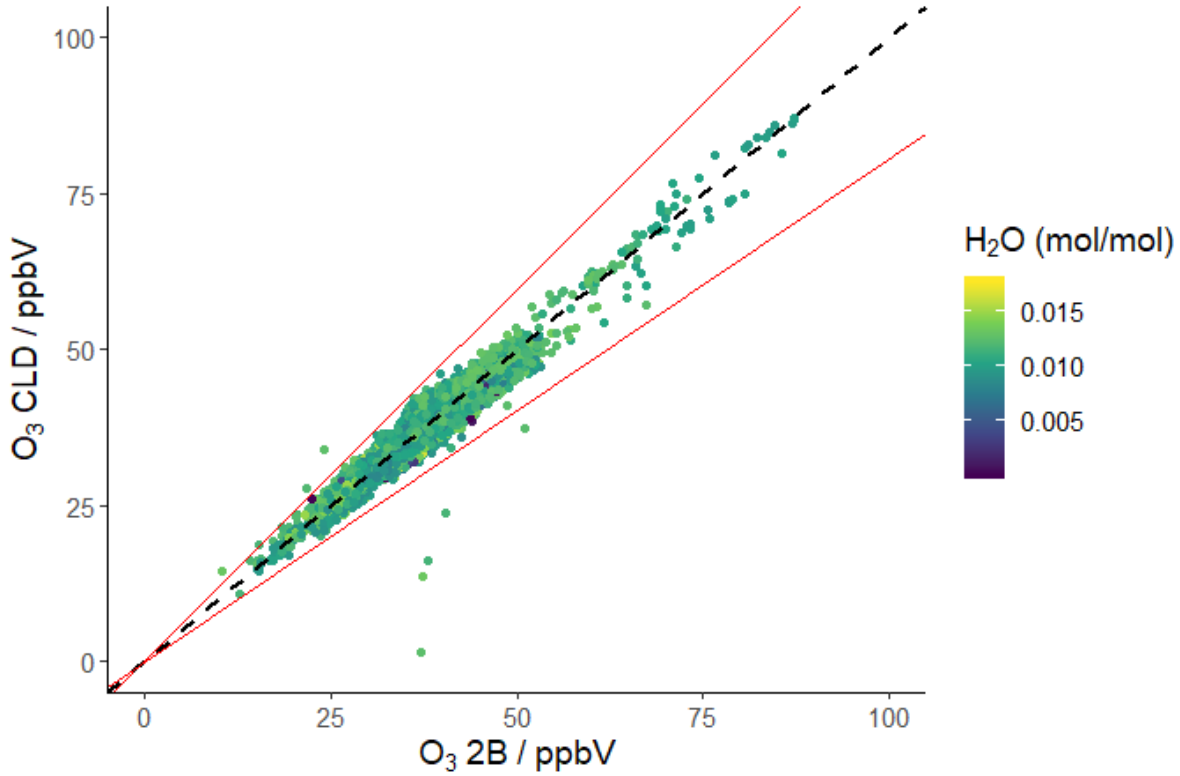

Figure 2.4: Calibration of the CLD86 against the 2B instrument at the PPAO during deployment 1. Each point represents a 20-minute mean ozone value, coloured by ambient humidity. CLD86 ozone values were calculated using the average sensitivity value of 240 counts $ppbv^{-1}$ s^{-1}, and the dashed line represents the corresponding 1:1 agreement. The red lines denote 3σ deviations, and points beyond this were later filtered out (see Section 2.5).

During deployment 2, the sensitivity of the CLD was significantly lower. Calibration using a Thermo 49i as reference gave a lower sensitivity of 86 counts $ppbv^{-1}$ s^{-1}, with dark counts of 210 counts s^{-1}. The 10 Hz counts deviation was 5 counts, resulting in a greater 10 Hz mixing ratio deviation at the lower sensitivity of 0.581 ppbv. Variability in ozone observed in the field was considerably higher than this, both due to natural variability and due to photon counting statistics resulting in greater variability at higher counts. This is discussed further in Section 2.7.

The AQD instrument used during the 3rd deployment presents a significant upgrade to the CLD86. The principles of operation remain the same, utilising the chemiluminescence of the reaction of O_3 with NO. In the AQD however, a more sensitive PMT is used, cooled to -20 °C with a Peltier cooler to reduce dark counts. This cooler is also in a sealed container, removing the need for a dry air supply to avoid water/ice formation. Additionally, both the sample and the NO line are controlled via MFCs allowing for more flexible use. The instrument shows a sensitivity of 1050 counts $ppbv^{-1}$ s^{-1} and dark counts of 900 – 2000 count s^{-1}, varying with the level of cooling achieved by the Peltier.

2.3 Measured Deposition Velocity

Deposition velocities for each deployment, calculated from the mass flux and ozone concentration (Section 1.3, Eq. 1), are presented in Figure 2.5. A single deposition value is obtained for a given averaging period – 20 minutes for deployments 1 and 3, and 60 minutes for deployment 2. These values are then displayed in a histogram for each month. Deployment 1 is presented as a single histogram, as the full deployment lasted only 6 weeks. Due to occasional outliers, median values will be focused on to avoid very few points distorting the monthly average. The median deposition velocity during the first deployment was 0.037 cm s^{-1}. During deployment 2 (discounting January which had very few data points) it varied between 0.024 – 0.038 cm s^{-1}. Finally, deployment 3 varied greatly between 0.008 – 0.031 cm s^{-1}. Time series of deposition velocity and mass flux are shown for each deployment in Figures 2.6 and 2.7 respectively.

These values are of similar magnitude and spread to those obtained by Helmig et al. (2012)[79]: 0.009 – 0.034 cm s^{-1}. However, those measurements were taken at very different locations, spanning from 40°N down to 50 °S. As such, the large variation in SST is expected to have significant influence on the deposition[149]. While SST does vary in the water around the PPAO, it clearly cannot exhibit the same range as observations across such a range of latitudes. Therefore, reactivity of the SML to ozone could provide some explanation, and the biogeochemistry at the PPAO and its expected effects on ozone deposition will be discussed in Chapter 3.

All data shown in Figures 2.5 - 2.7 have been calculated with a number of filters and processing decisions in how the fluxes and subsequent deposition velocities are calculated, as outlined in Sections 2.4 and 2.5.

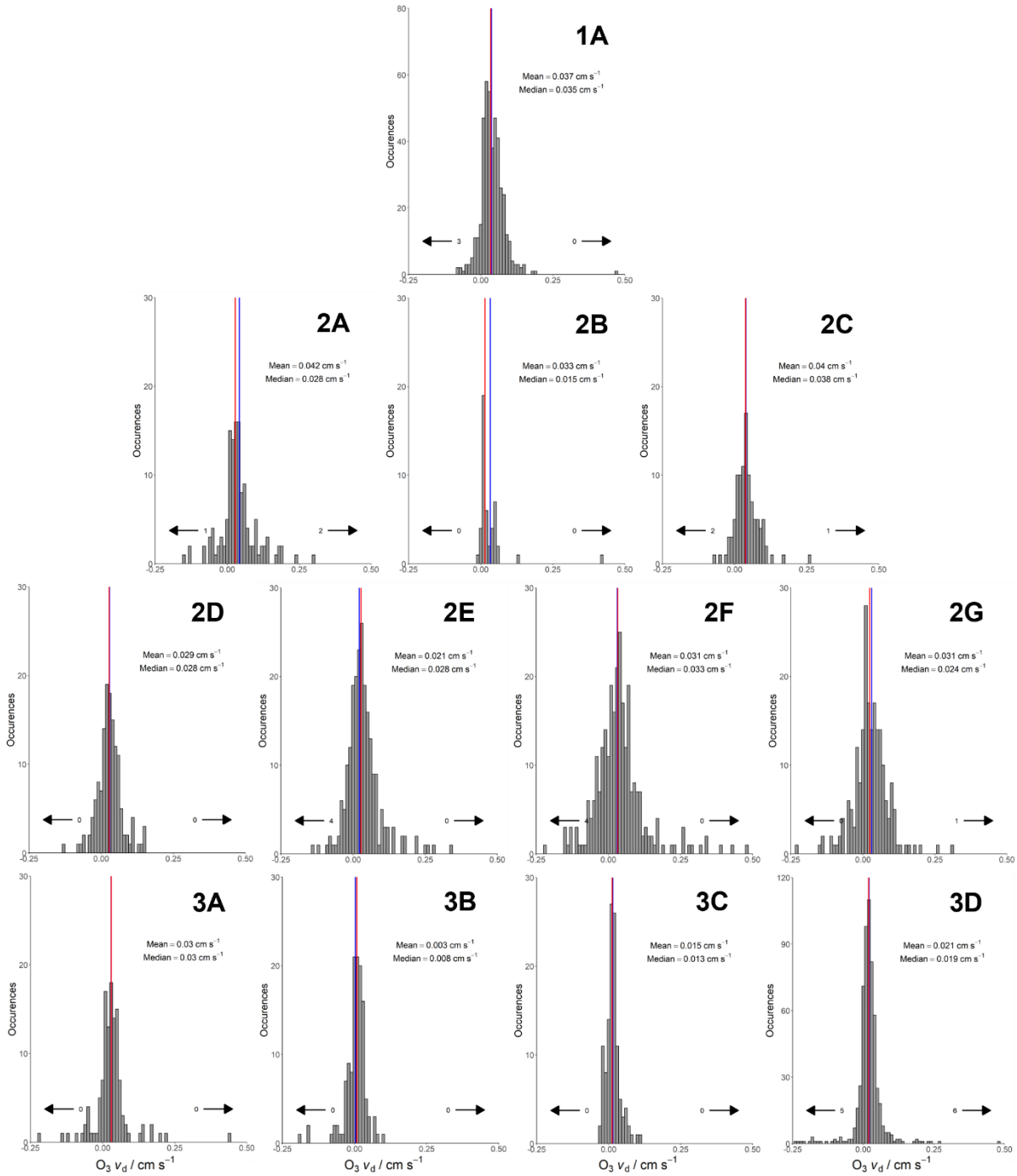

Figure 2.5: Histograms of deposition velocities for each deployment. 1A shows the whole of the first deployment (April/May 2018), 2A-G show the month of December from 2019, as well as January, February, May, June, July, and August 2020, respectively. 3A-D show the months of February to May respectively from 2021 during deployment 3. Values are placed in bins of width 0.01 cm s^{-1}, with means and medians marked by red and blue vertical lines, respectively. The numbered arrows display the number of points lying beyond the limit of the x-axis. Note that the y-axis is extended for 1A and 3D relative to the others due to the larger datasets. Additionally, each single v_d value during deployment 2 was calculated from 60 minutes of high-frequency data, rather than 20 minutes as was the case for the other deployments.

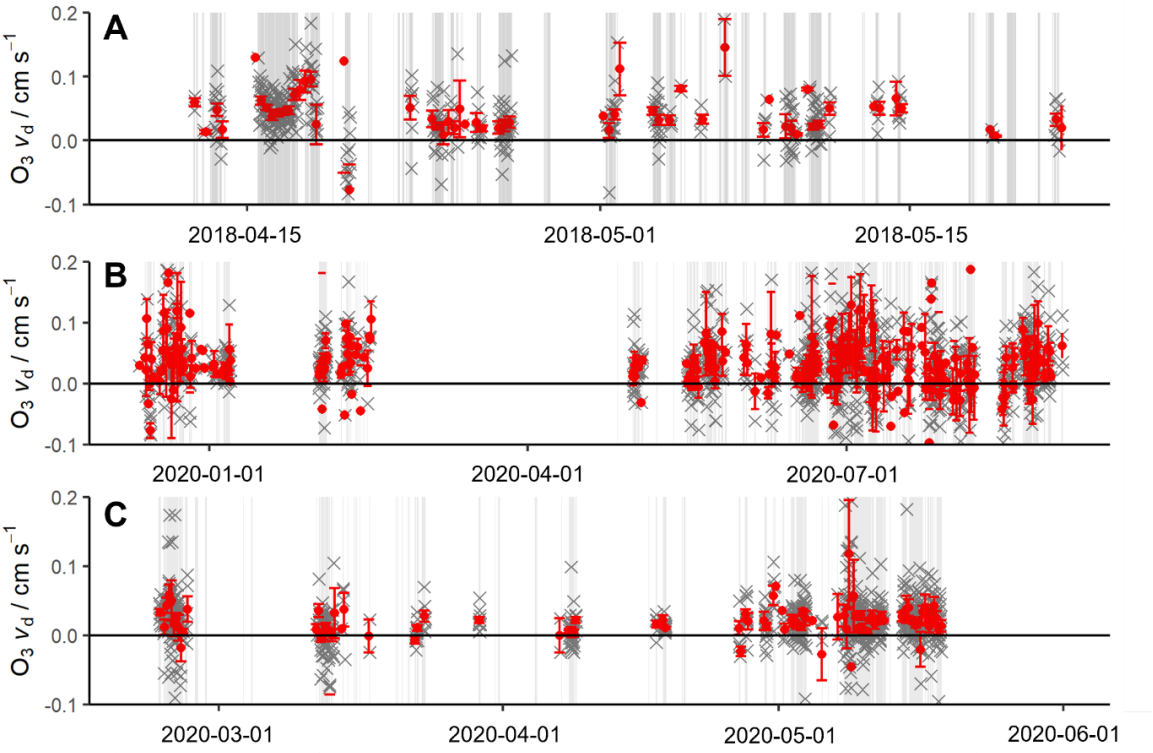

Figure 2.6: Time series of ozone deposition velocity for deployments 1-3 (A-C respectively). Grey crosses represent individual deposition values (20-minute in A and C, 60-minute in B), with red dots for 6-hour means with standard errors. Periods with an accepted wind direction (180-240°) and sufficient data are shaded. The y axis in is limited as -0.1 – 0.2 cm s^{-1} for clarity.

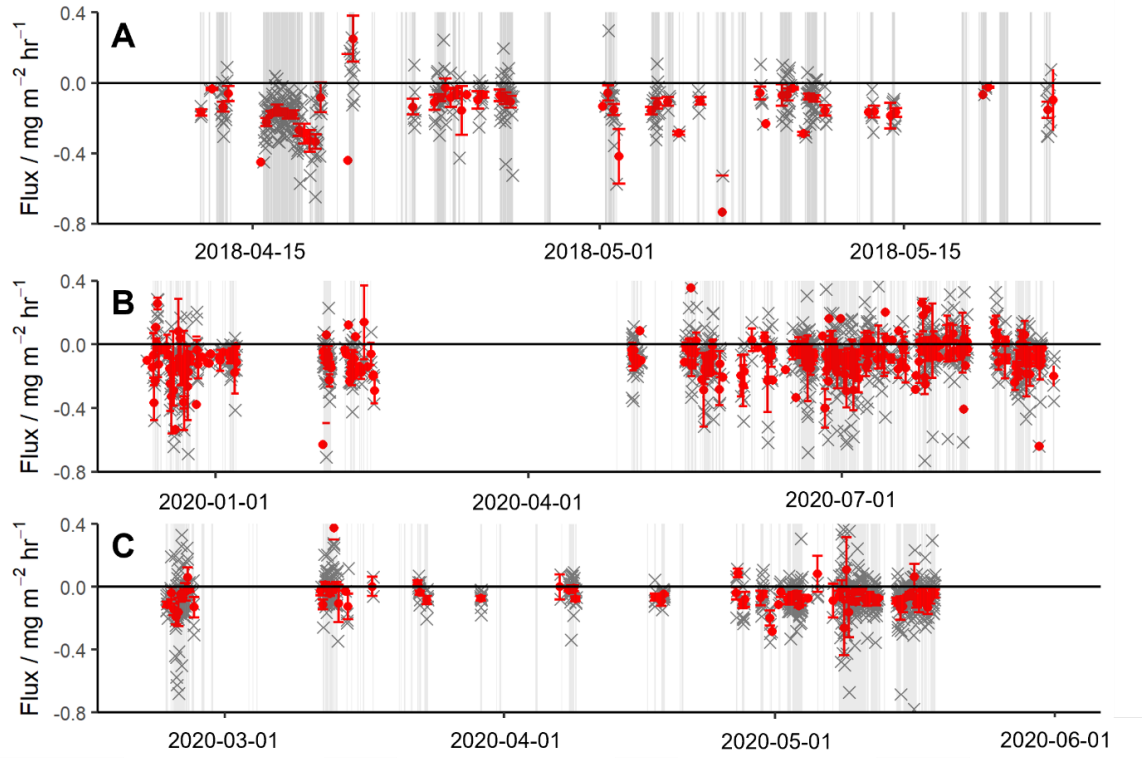

Figure 2.7: Time series of ozone mass flux for deployments 1-3 (A-C respectively). Grey crosses represent individual flux measurements (20-minute in A and C, 60-minute in B), with red dots for 6-hour means with standard errors. Periods with an accepted wind direction (180-240°) and sufficient data are shaded. The y axis in is limited as -0.8 – 0.4 mg m^{-2} h^{-1} for clarity.

2.4 Flux Parameters

Most decisions around the handling of the flux data were made in the context of the first deployment, though some decisions were revised in subsequent deployments. A summary of the whole workflow is given in Figure 2.8.

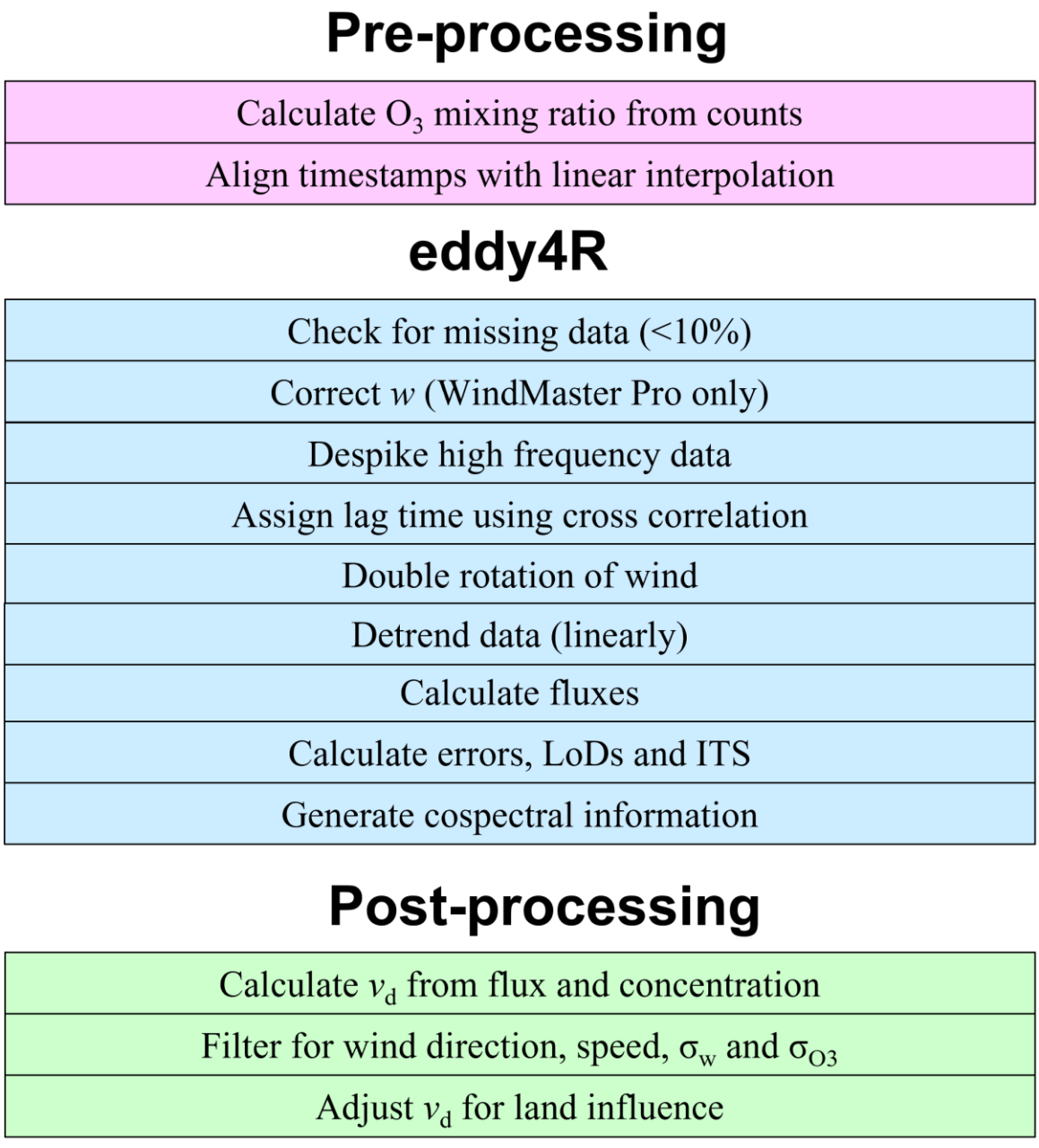

Figure 2.8: Workflow for the processing of eddy covariance data using eddy4R.

Most of the processing was accomplished within the framework of eddy4R, the framework for eddy covariance developed and updated by the National Ecological Observatory network (NEON)[150]. Initially though, it was necessary to determine ozone mixing ratios from raw counts by converting using sensitivity determined through calibration (e.g. Figure 2.4). Then, wind and meteorology data were aligned with the timestamps of the ozone data via linear interpolation. Within the eddy4R workflow, periods with >10% missing data were rejected before correcting the vertical wind component as necessary for data generated by the WindMaster Pro sonic anemometer. Data were then despiked using a median filter despiking method[151,152] before calculating and adjusting for the lag between wind and ozone data (discussed further below). The wind data were then rotated such that the mean vertical wind was 0 for the averaging period, known as double rotation[153]. Fluxes were then calculated from the covariance of the deviations of ozone and vertical wind from a linear detrended mean. Subsequently, errors, LoDs and integral turbulence statistics (ITS) were generated (Section 2.7) along with cospectral information. Outside the eddy4R codebase, deposition velocity was calculated from flux and concentration data, and further filters applied for stationarity and observation of a marine sector. Finally, the effect of land on accepted data was examined using footprint analysis (Section 2.6).

A crucial part of the workflow warranting particular focus is the calculation of lag necessary for aligning the ozone and wind data. This is because while the sonic anemometer logs wind speeds nigh instantaneously, the sample air that 'corresponds' to that measurement must travel down the sample line to the detector, effectively lagging behind the wind data. A rough estimate can be acquired by simply using the flow rates and volumes of the sample lines. During deployment 1, the sample line consisted of 10 m of 3/8'' tubing with a flow of 13.5 L min^{-1} plus 2 m of 1/8'' tubing with a 300 mL min^{-1} flow. This yields a calculated lag of 4.2 seconds.

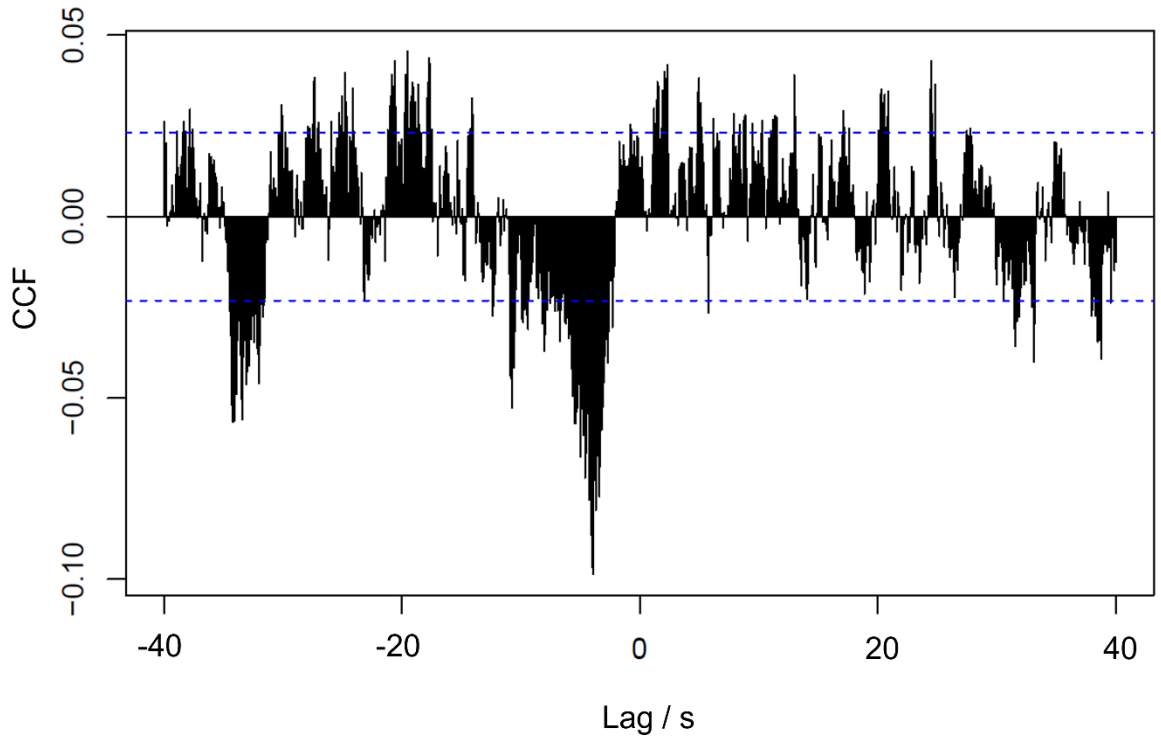

Figure 2.9: Cross-correlation function plotted for 13:00 to 13:20 on 15th April 2018 during deployment 1. The negative peak at -4 s shows that the data is lagging behind the wind data by this amount. Blue dashed lines denote the 95% significance threshold.

In order to ozone calculate a more accurate lag, cross-correlation functions (CCFs) were calculated for the ozone and wind data in 20-minute intervals, with the two datasets shifted in time in many 0.1 second intervals. The CCFs output a series of values from -1 to 1, representing perfect anticorrelation and perfect correlation between the two datasets, respectively. As depositions are observed for ozone over water, an anticorrelation is expected (on average, ozone concentrations are low when vertical wind speed is high/positive, and vice versa). In order to help identify a correlation peak above the noise, a high-pass filter was used to maximise the cross-correlation[154]. Figure 2.9 shows a CCF for a 20-minute period from 13:00-13:20 UTC on 15th April 2018. In instances like this, a strong flux creates a large peak above the noise, the maximum of which can be used to precisely (to 0.1s) determine the lag for the period. However, in cases where flux is small in magnitude, the largest CCF peak may be a result of random correlation in the noise rather than the true flux signal. If the highest magnitude CCF peak was always used, these cases in which flux might truly be near-zero would be incorrectly biased away from zero. Figure 2.10 shows the unfiltered deposition velocity values obtained from deployment 1 if the lag time is freely chosen between 0 and 40 seconds.

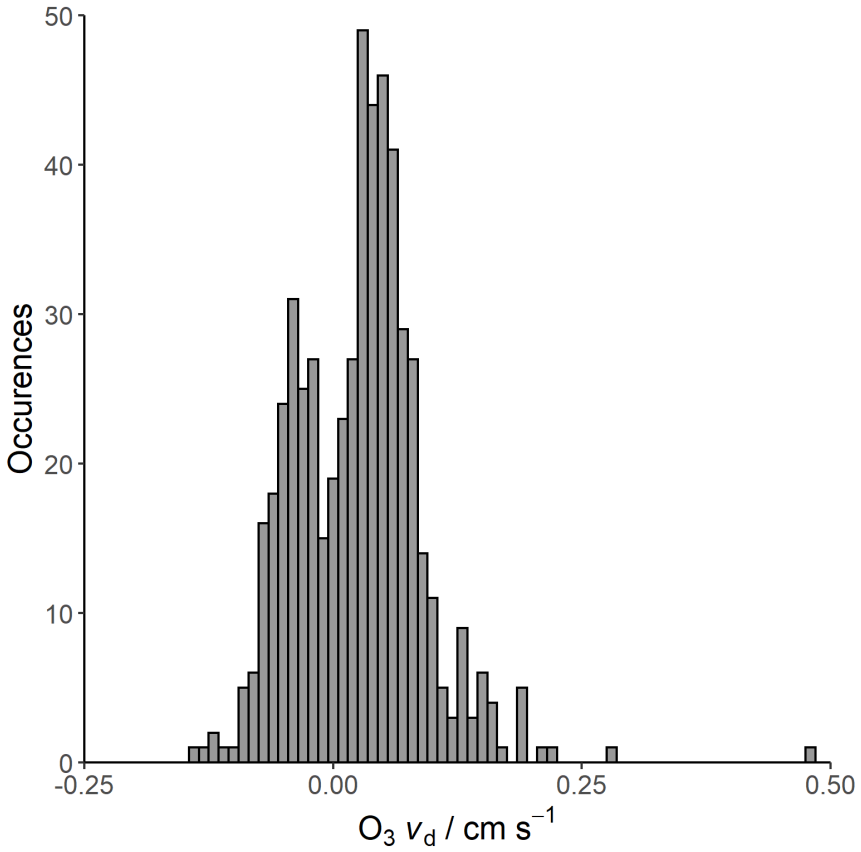

Figure 2.10: Histogram of deposition velocities obtained during deployment 1 if CCFs are allowed to determine lag times for all periods within the bounds 0-40 seconds. The typical Laplace distribution is skewed to very high or very low (negative) values, with the bin at 0 being especially empty.

The lack of data points at or near 0 in Figure 2.10 show a clear biasing of deposition values away from 0. As such, constraints were put on the values of lag that could be accepted as real. CCFs using whole days of data indicated that the lag drifted from 3.9 – 4.1 s over the course of deployment 1. Therefore, any lag identified by the 20-minute CCFs to be between 3.5 and 4.5 seconds was accepted to allow for slight variation in pump strength, pressure etc. Values determined beyond these bounds were instead set to a value from 3.9 to 4.1 s, determined from a linear regression of lags within the bounds. A comparison using a fixed 4 s lag time for the same data led to a modest 5% decrease in the median observed flux. In deployment 2, no clear drift in lag times was identified, and so a fixed value of 5.2 s was used where lags identified from CCFs fell outside the range 4.2 – 6.2 s. In deployment 3, the lags determined from CCF initially appeared to drift wildly, far more than could be physically reasonable. This was later determined to be caused by the timestamp of the AQD ozone data drifting from that of the wind. Lags were therefore determined from a moving function of longer period CCFs.

Another decision in processing flux values was the averaging period over which to calculate single flux values. Averaging times of 10-60 minutes are common[155], and the exact choice is a trade-off. Longer averaging times can be helpful in developing a clear covariance above any noise but risks a lack of stationarity in the averaging period. Shorter averaging periods avoid as many stationarity

issues as longer ones, but the covariances can be less defined or lost in the noise. Additionally, extremely short averaging periods risk failing to capture low frequency turbulence and its contribution to total flux. For deployment 1, an averaging period of 20 minutes was chosen, at which 114 of 432 20-minute periods identified a peak within bounds via CCF. Extending the averaging period to 1 hour was considered but resulted in a 23% reduction in data passing filtering criteria, largely due to stationarity and missing data criteria (discussed in Section 2.5). This 20-minute averaging period was also used for deployment 3, but deployment 2 was changed to use a 60-minute averaging period. This was due to frequent failure to identify acceptable CCF peaks, and a low flux limit of detection at 20-minutes.

The height at which measurements is taken is also important, as it defines the extent of the flux footprint – the size and shape of the surface for which a flux is being observed. A consideration unique to coastal tower flux measurements is that of 'variable' measurement height due to the sea level varying with tide. This effect can be considerable, with the waters around the PPAO having a tidal range of ~6 m. Tidal data from the British Oceanographic Data Centre (BODC) measured roughly 6 km upstream were therefore used to adjust the measurement heights.

Another decision made was the use of linearly detrending for the ozone data. This involves calculating the deviations for a given period from a linear fit to those data rather than a fixed mean, since changing of ambient ozone on that timescale are not uncommon. This does introduce possible loss of flux from low frequency eddies due to linear detrending acting as a low-pass filter[156], but a comparison to the same data generated using a simple block average yielded a small difference in median flux of 1.7% suggesting this is not a major issue. Similarly, a double-rotation approach was used, rather than a sector-wise planar fir with regards to co-ordinate rotation to avoid any discontinuous treatment of data within the south-west sector. For comparison, use of planar fit in place of double rotation increased the median flux observed in deployment 1 by 7%.

2.5 Data Filters

All of the decisions discussed above define decisions made involved in the calculation of flux values and v_d values. A number of filters have then been applied to the calculated deposition velocity data in an attempt to make the dataset accurately represent deposition to the sea surface.

Firstly, over the course of all deployments, there were many brief periods of downtime in the ozone measurement for a variety of reasons, such as replacing the reagent gas cylinder, replacing desiccant or instrument faults. Any missing data within an averaging period could result in questionable flux

values from the period based off of very little data. As such, any period in which either wind or ozone data were missing for more than 10% of entries were rejected.

For the first deployment, periods in which the agreement between the CLD86 and the 2B calibration instrument were beyond the 3rd standard deviation (3σ) of 20-minute calculated sensitivities were also removed. This filter was dropped in subsequent deployments due to non-trivial vertical separation of the two instrument inlets of ~5 m.

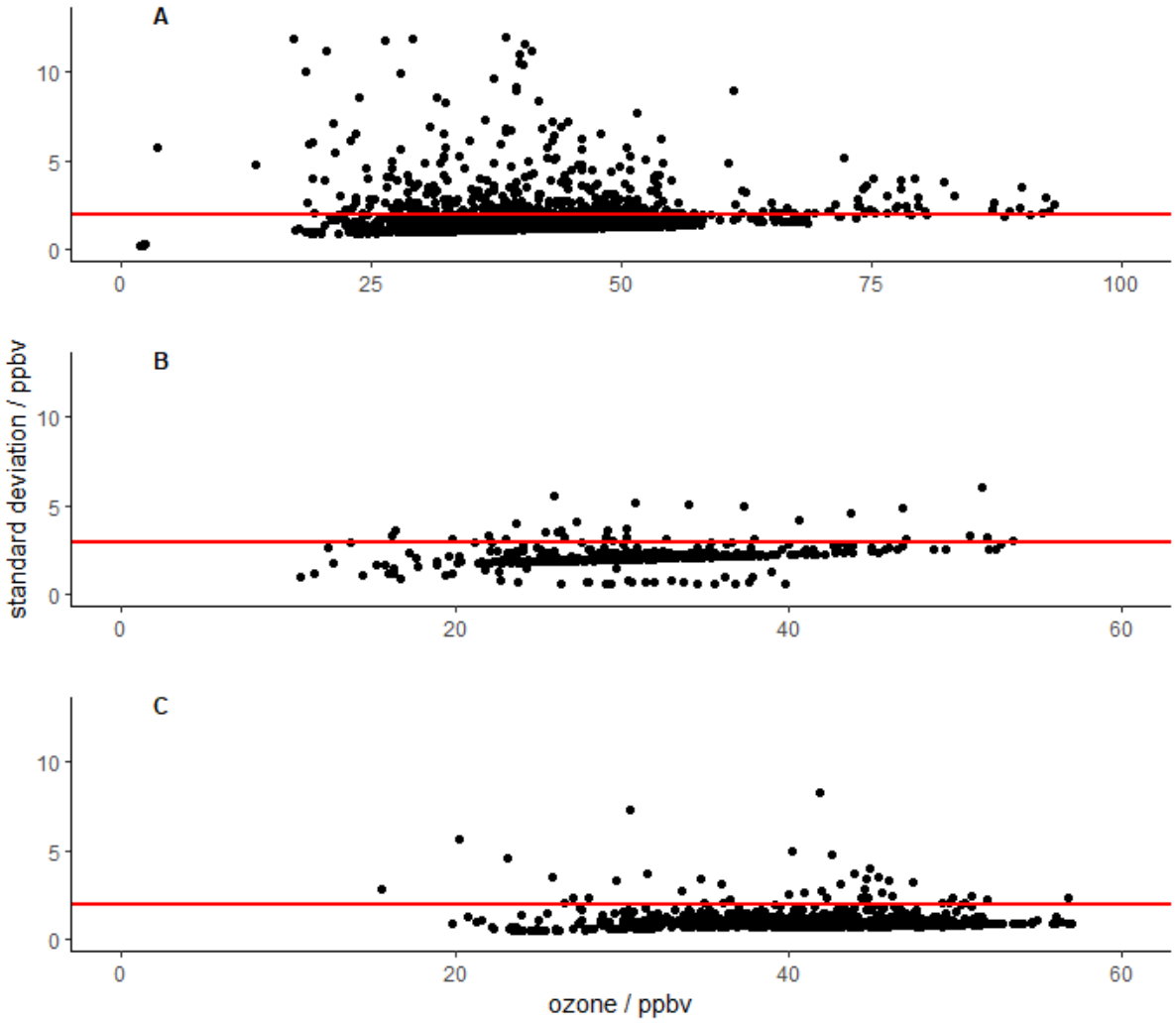

Figure 2.11: Standard deviations in the ozone measurements increasing with ozone mixing ratio. Plots A, B and C show all data from deployment 1, August from deployment 2, and May from deployment 3 respectively. Red lines show the cut-off above which data were rejected, 2 ppbv in A and C, and 3 ppbv in B. Note that the x axis extends to 100 ppbv in panel A due to an episode of very high ozone concentrations.

One major aim of filtering the data was to avoid periods of non-stationarity. That is, periods exhibiting rapidly changing ozone concentrations or wind conditions. To this end, data were rejected if the standard deviation of the wind direction within the averaging period was greater than 10°, as this would significantly alter the area being observed. This most commonly occurred at low wind

speeds. Stationarity in the ozone data was also checked via the standard deviation in the 10 Hz mixing ratio data. In chemiluminescent detectors like the CLD86 and the AQD, the deviation in ozone signal is typically higher at higher concentrations, and this can be seen in Figure 2.11. However, some periods clearly displayed variations considerably above the norm. Therefore, during deployments 1 and 3 data were rejected when the standard deviation of ozone rose above 2 ppbv, similar to the approach taken by Helmig et al. (2012).

During deployment two, the decreased sensitivity of the CLD86 led to large amounts of data being rejected by this filter. The threshold was therefore relaxed to a standard deviation of 3 ppbv, with a view to preferring a reasonable amount of lower quality data than spare temporal coverage of good data. This difference in data treatment is important when considering comparison between deployments. A filter to avoid drift in ozone mixing ratio over the averaging period was also used in deployment 1, removing any periods in which the mixing ratio ended more than 6 ppbv away from the value at the start of the period. However, this filter was dropped for subsequent deployments, as the effect is largely accounted for by linear detrending, and only 3 points were removed by the filter uniquely.

Additionally, the decision was made to only consider deposition in the south-west sector, 180-240° from North. Few data points are present in the south-east sector due to the infrequency of southeasterlies, and observing data from due-west risks observation of flux to the land along the coast rather than the sea. The same is true for the data to the north-east, as Figure 2.2 shows the bulk of the wind data being along the coastline.

A useful tool in considering whether a given period of flux data is affected by land is the roughness length, z_0. It can be calculated by Eq. 8:

$$z_0 = z/e^{\left(\frac{kU}{u_*} - \Psi_m\left(\frac{z}{L}\right)\right)} \quad (8)$$

Where z in the measurement height (adjusted in this case for tidal height), k is the Von Kármán constant (=0.4), u_* is friction velocity (determined directly from the covariance of the fluctuations of horizontal and vertical wind components), and $\Psi_m\left(\frac{z}{L}\right)$ is the integral of the universal function, with dimensionless Obukhov stability z/L calculated from observed heat flux and u_*. $\Psi_m\left(\frac{z}{L}\right)$ is defined as follows[157,158]:

$$\Psi_m\left(\frac{z}{L}\right) = -6\frac{z}{L} \quad for\ \frac{z}{L} \geq 0 \quad (9)$$

$$\Psi_m\left(\frac{z}{L}\right) = ln\left[\left(\frac{1+x^2}{2}\right)\left(\frac{1+x}{2}\right)^2\right] - 2tan^{-1}x + \frac{\pi}{2} \quad for\ \frac{z}{L} < 0 \quad (10)$$

where

$$x = \left(1 - 19.3\frac{z}{L}\right)^{1/4} \tag{11}$$

Roughness length values are proportional to the height of roughness elements present on the observed surface. Due to the flat, smooth nature of the sea, especially under calm conditions, low values of around 2×10^{-4} m are typical for such observations[159]. While they will vary with atmospheric stability and sea roughness, the presence of drastically elevated values suggests the observation of roughness elements on land rather than at sea.

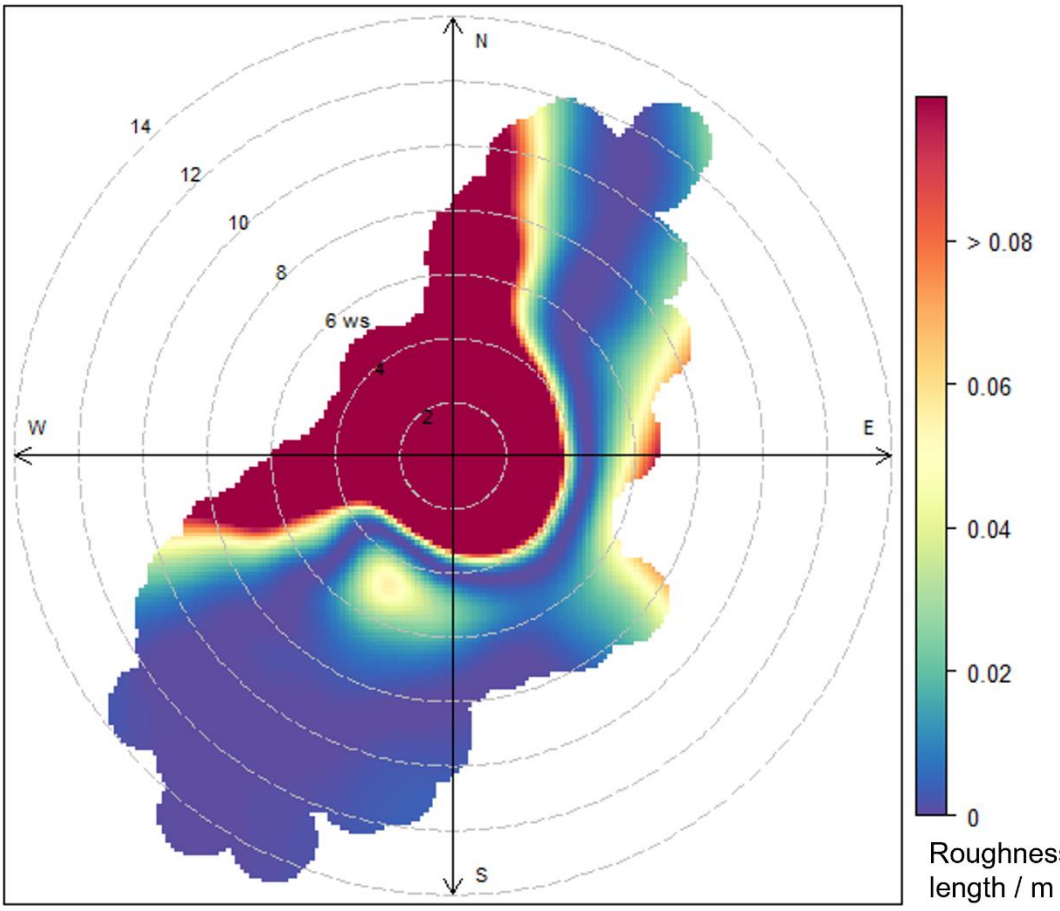

Figure 2.12: Polar plot of roughness lengths at the PPAO during deployment 1. The colour denotes roughness length, with low values ~10^{-3} m in blue and high values above 0.1 m in red. Roughness length values are plotted radially against wind speed/direction. The headland on which the PPAO is built can be seen to cause elevated roughness length at low wind speeds in all directions, and the land in the north-west quadrant causes high roughness regardless of wind speed.

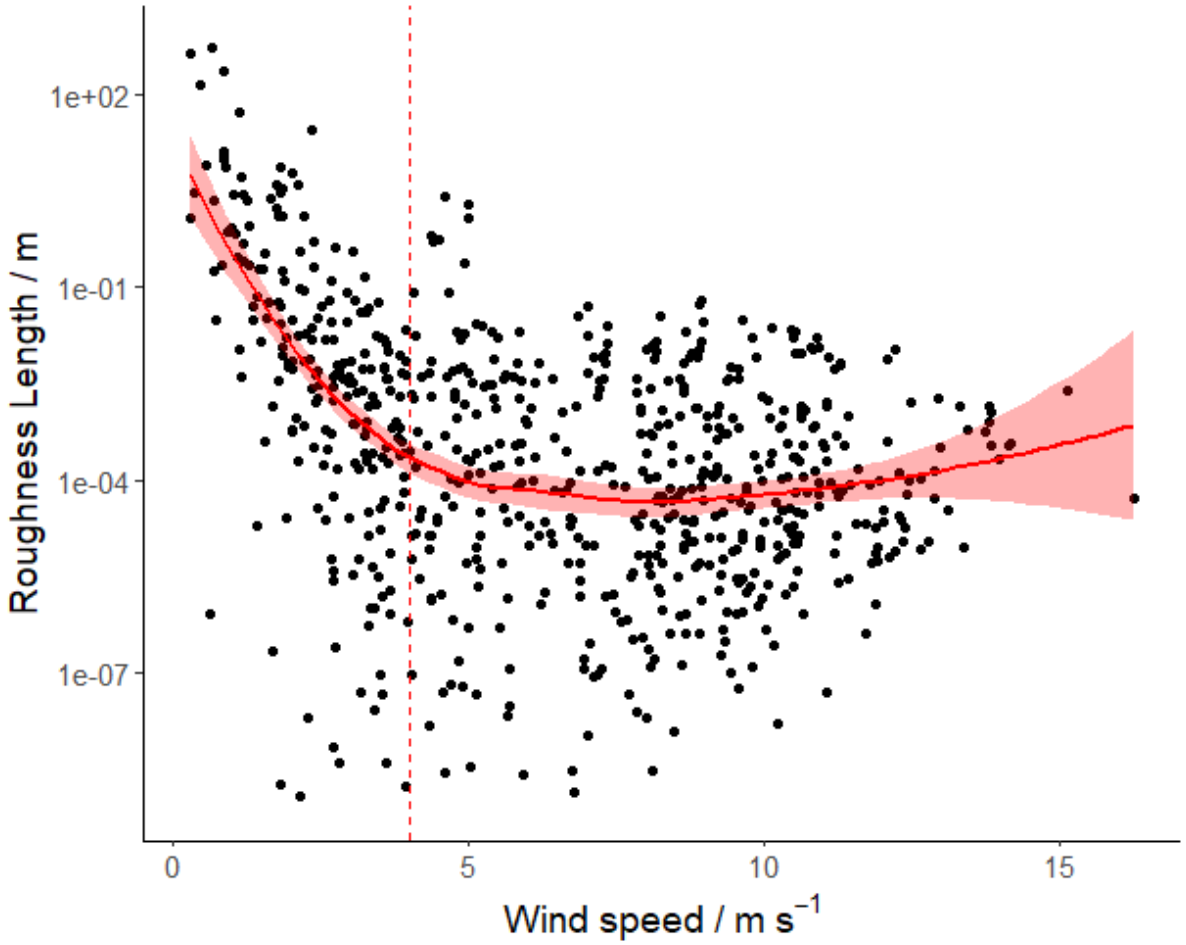

Figure 2.13: Roughness length for each averaging interval in the 180-240° sector for deployment 1 (black dots) with a smoothed local regression (LOESS) line (solid red, 95% confidence interval shaded). Only flux values during period with wind speeds above the threshold of 4 m s^{-1} (dashed red) were accepted. Y axis limited for clarity, with 17 points < 10^{-9} m not shown.

Figure 2.12 shows how roughness length values are higher than could be expected of the sea for almost all wind speeds in the north-west sector, as expected due to the headland. It also indicates that measurements taken at low wind speeds are influenced by roughness elements on the land on which the PPAO is built. The variation of roughness length with wind speed can be seen for the whole of deployment 1 in Figure 2.13.

Below ~4 m s^{-1}, roughness length is elevated beyond what would be expected for oceanic observations. This suggests a need for a windspeed-based filter to ensure as far as possible that observations are representative of the ocean and not land. This is particularly important in the case of ozone, as deposition to land is generally much higher than to the sea; a small area of land could significantly bias the deposition values to be greater in magnitude.

Deposition velocities during the first deployment showed some variation with wind speed. The increase at high winds can be explained by the greater turbulence correlating with faster winds, and is

observed in some, but not all previous measurements[69,79]. The greater deposition at low wind speeds however is harder to explain without land influence affecting the measurements. The need for such a wind speed filter to avoid land influence has been seen at the site before, with CO_2 flux measurements at the PPAO also showing elevation at low wind speeds[160,161]. Given the elevation in both roughness length and deposition velocity below 4 m s^{-1}, this was the threshold decided upon.

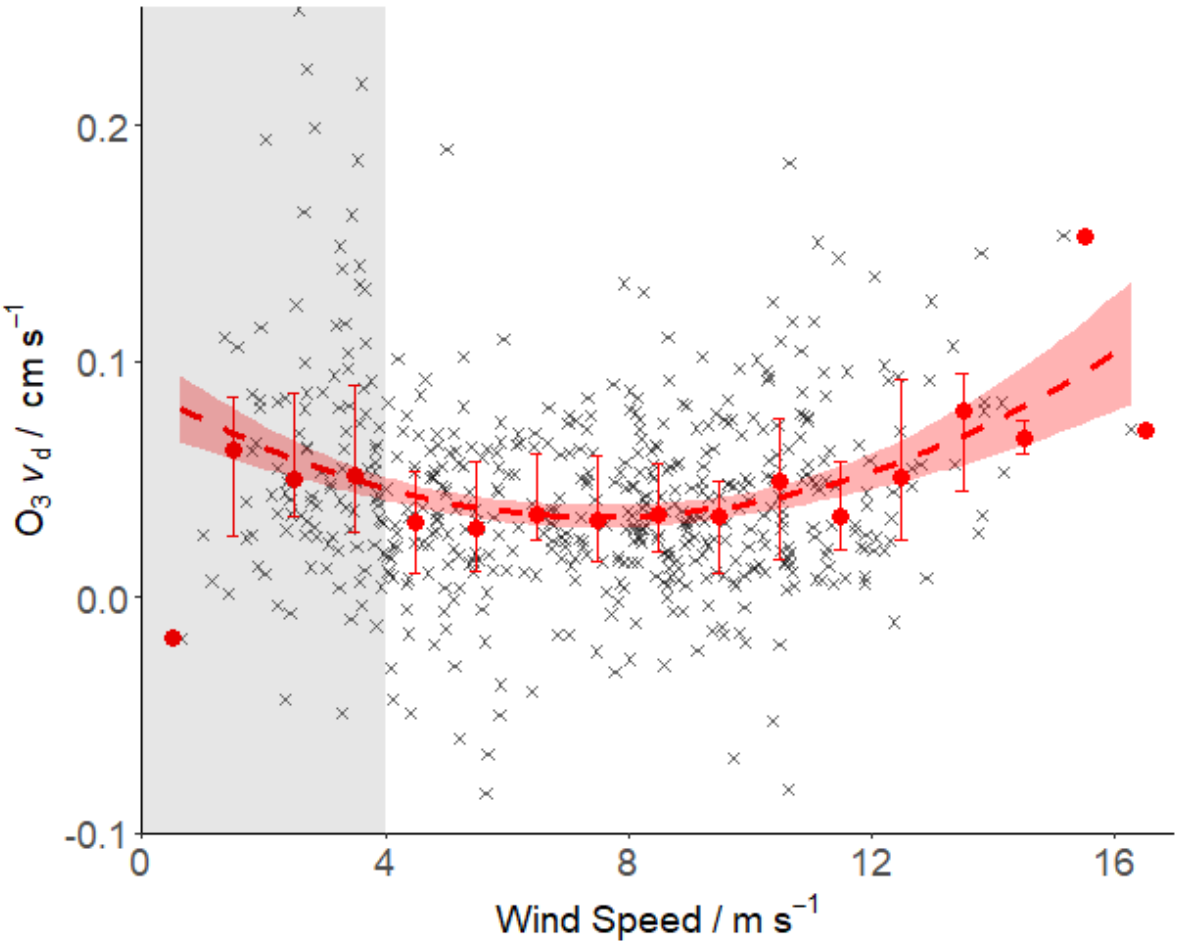

Figure 2.14: Deposition velocity dependence on wind speed. 20-minute values are shown in grey, with bin-averaged medians (1 m s^{-1}) and interquartile ranges shown as red dots with bars. A 2nd order polynomial fit is plotted as a dotted red line with a 95% confidence interval (red shaded area). The grey region below 4 m s^{-1} indicates values removed by the wind speed filter that are not included in the fit.

2.6 Flux Footprint and Land Influence

A flux footprint defines the area of a surface that is being observed during flux measurements, and the relative contributions of points within that area to the measured flux. In the case of emissions, it can intuitively be understood as the probability of a gas molecule emitted at a point on the surface ending up being measured at the detection point and therefore contributing to the measured flux. It therefore necessarily depends heavily on the height of the observation point, with greater elevation extending

the footprint maximum and extent. For deposition, it can be thought of as the probability of the sinks at the surface causing a molecule to move downwards the full distance of the measurement height. A large number of different approaches to calculating flux footprint exist, many of which are computationally laborious to run, especially for long time series. A such, for this work the 'simple' flux footprint prediction (FFP) of Kljun et al. (2015) was used, which itself is a parameterisation of the more complex Lagrangian stochastic particle dispersion footprint model, LPDM-B[162]. This allowed for land coverage within the flux footprint to be approximated for a variety of wind conditions over the course of deployment 1.

As mentioned, measurement height plays a role determining the extent of the flux footprint, with roughness length, friction velocity, Obukhov length, cross wind deviation and wind direction all also defining the dimensions of the footprint. A single footprint can be generated for each averaging period, or the above parameters can be provided for multiple periods to generate an average footprint climatology for all provided data. An example land class analysis of all flux measurements with wind speeds of 4-5 m s^{-1} that passed other criteria is shown in Figure 2.15.

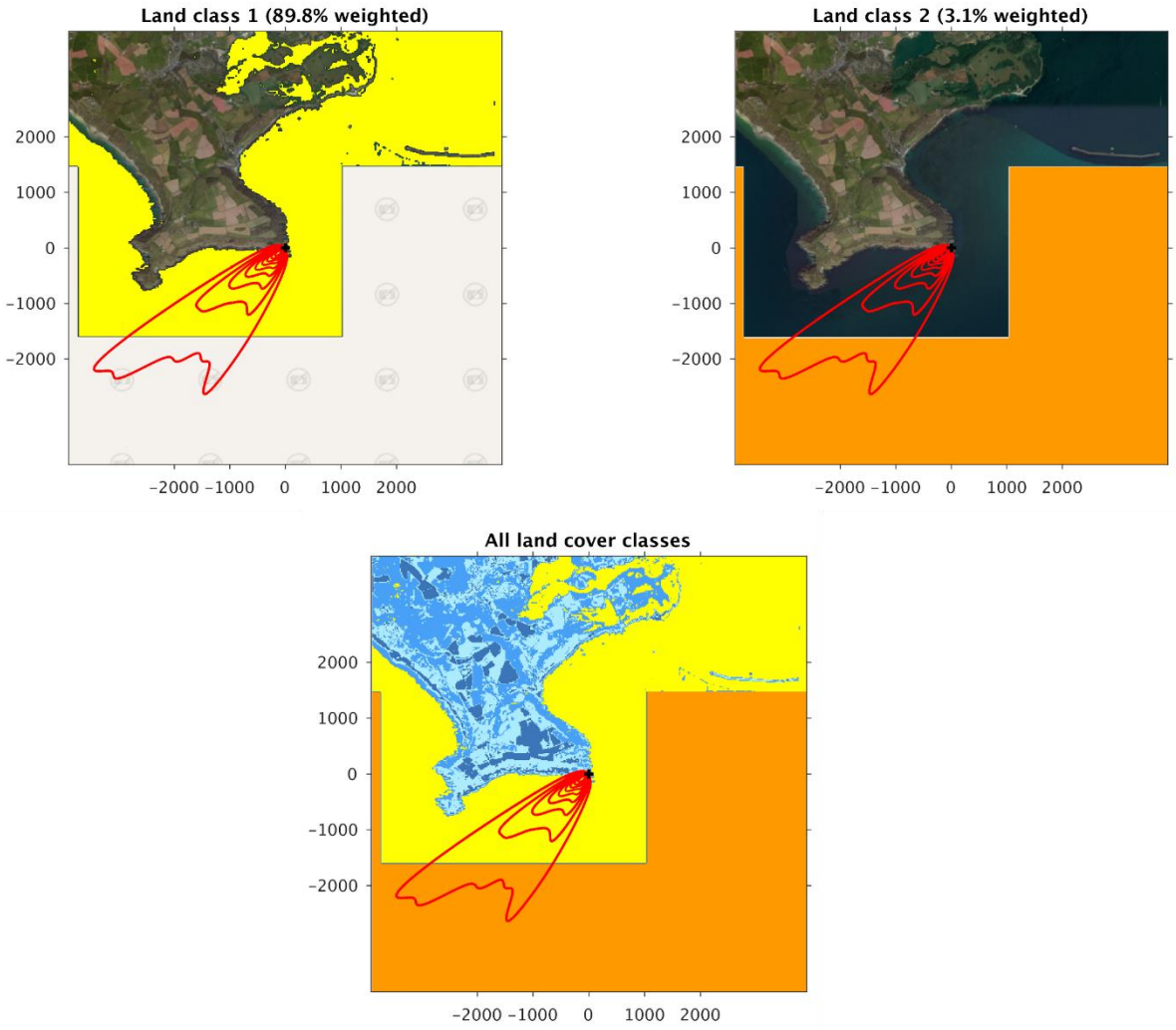

Figure 2.15: Land class footprint analysis of data with wind speeds of 4-5 m s^{-1} from deployment 1. Each contour represents a 10% contribution to the flux, with 90% of the flux contribution coming from the area within the outermost contour. Some satellite imagery is not properly acquired away from the land, but since there is no land within the yellow area, the oceanic contribution can simply be summed from the two parts. In this case, the land contribution was determined to be 7.1%.

The application of this footprint parameterisation is not without its caveats. Most notably, the parameterisation assumes the surface to be homogenous. In this work, this is clearly not the case due to the headland on which the PPAO is built. Additionally, a measurement height of 19 m (adjusted for tide) is used. This value is accurate for the oceanic region of the footprint, but the effective measurement height above the land would be lower. Therefore, the footprint maximum may be closer to the observation point than suggested by these parameterisations. This effect may also be compounded by deposition being greater over land than sea; since the contribution assumes homogeneity, the reality of land near the observation site may also lead to nearer footprint maxima.

With these limitations, truly definitive values for the land within the footprints are not feasible. However, values for footprint with varying wind bins can be used as an indicator for a suitable wind speed threshold to mitigate the effects of land appropriately without discarded vast amounts of data. All data for deployment 1 that passed the stationarity, direction and missing data filters were sorted into 1 m s^{-1} wind speed bins, and a land percentage value obtained for each bin.

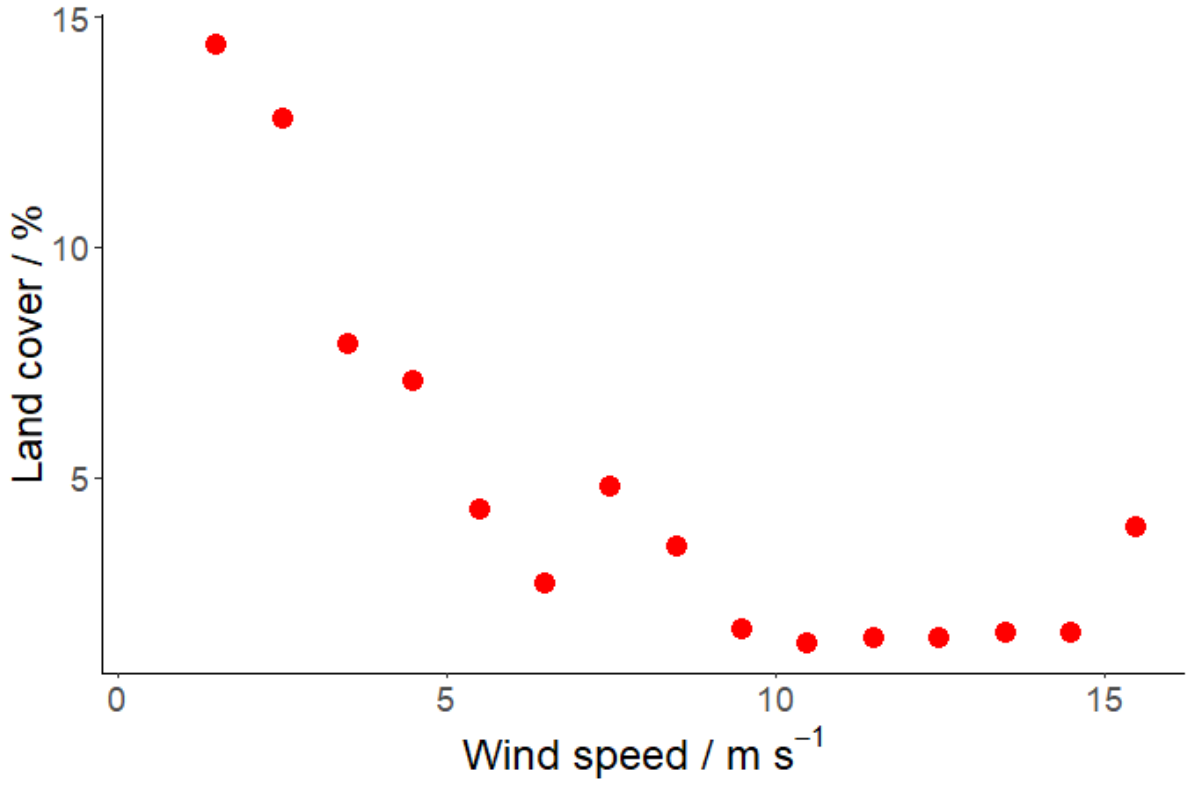

Figure 2.16: Land cover percentage within the average flux footprint for 1 m s^{-1} wind speed bins as calculated with the Kljun et al. (2015) flux footprint parameterisation. The presence of land within the footprint area was greater during periods of low wind speed and atmospheric instability.

From Figure 2.16, there is a strong drop-off in the amount of land within the footprint beyond 3 m s^{-1}. Though the land cover between the 3-4 m s^{-1} and 4-5 m s^{-1} bins is similar, the roughness length values from Figure 2.13 still imply some influence of land on the wind. Therefore, a lower limit of 4 m s^{-1} for windspeed was used for accepted data, corresponding to an approximate land area within the footprint of 7.5%.

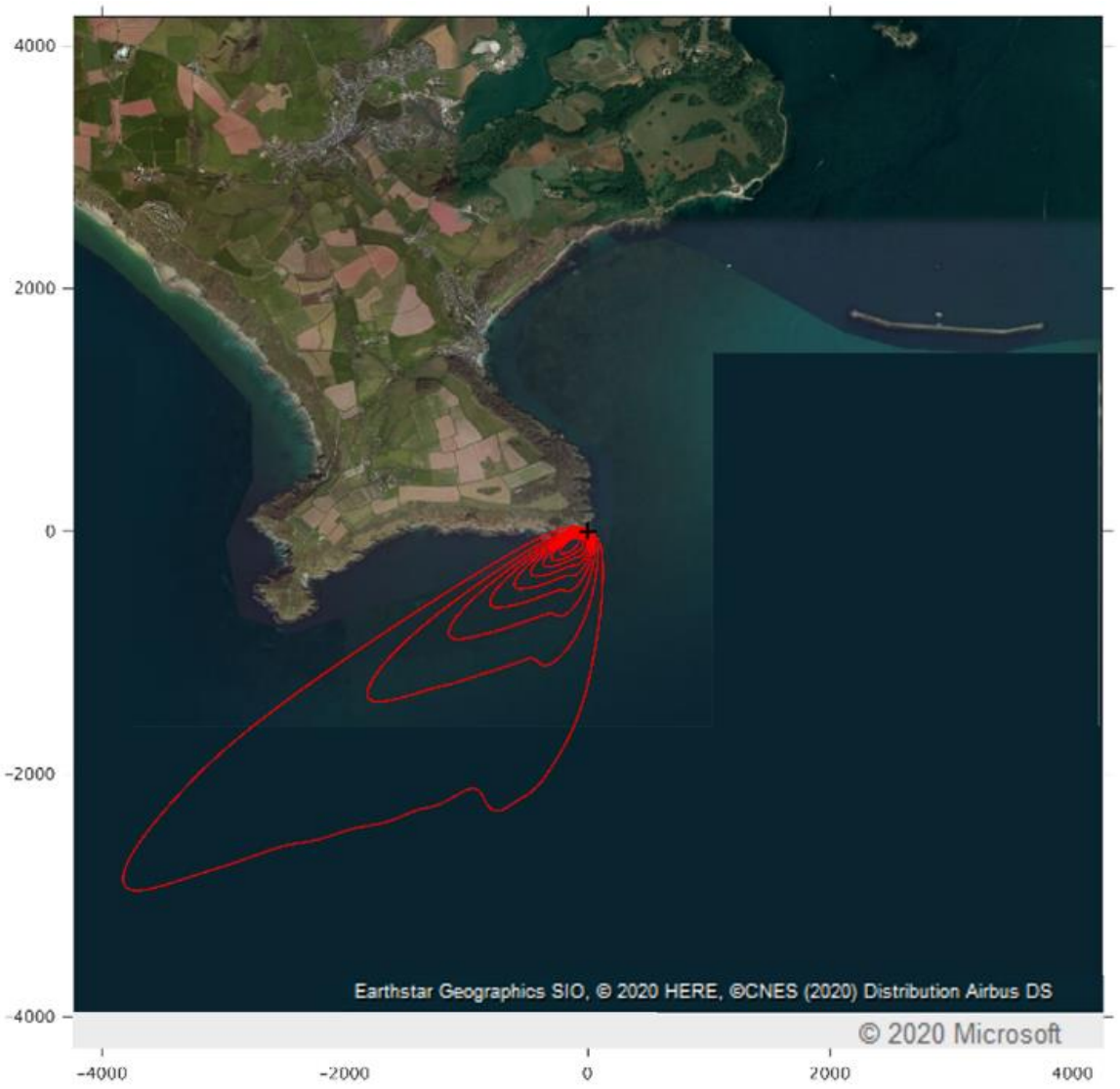

Figure 2.17: Footprint for all accepted data at the PPAO from deployment 1. Each contour represents an area contributing 10% to the total flux. The majority of contribution is from within a few hundred metres of the tower, though in extreme conditions the outmost contour (90% contribution) extends 4 km from the point of observation.

Due to the position of the PPAO, zero land influence is unattainable. The applied wind speed filter aims to strike a balance between having data that accurately represents oceanic flux, while retaining enough individual data points to actually interrogate variations with meteorology and SML composition (see Chapter 3). As such, some bias in the accepted deposition velocities will remain. A footprint for all accepted data during deployment 1 is shown in Figure 2.17, in which the land area in estimated to be 3.9%. A worst-case estimate of the amount this could affect the observed depositions can be obtained by simply weighting a typical grassland deposition velocity (~0.25 cm s^{-1}) by this area. This attributes 0.00975 cm s^{-1} of the total 0.035 cm s^{-1} for the first deployment to land, leaving a deposition to water estimate of 0.025 cm s^{-1} - a reduction of 28%.

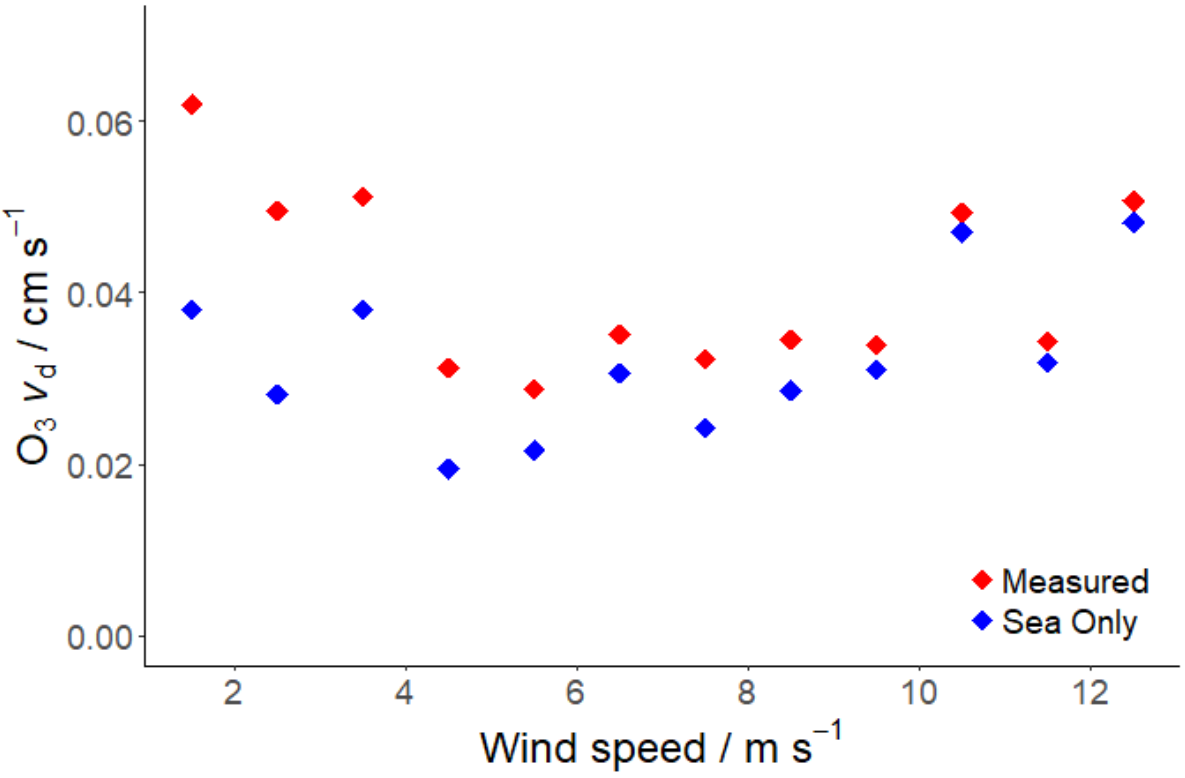

Figure 2.18: Median deposition velocities in 1 m s^{-1} wind speed bins for combined land and sea surfaces as measured (red) and for sea only (blue) during deployment 1. Sea only values were calculated by subtracting the land contribution, estimated from the land cover and land deposition determined by least square regression. Bins were only used up to 13 m s^{-1} as the bins beyond that contained only 4 observations between them.

In reality, the headland is a mixture of grass, semi-paved areas, and rocky shoreline. It is reasonable to expect deposition to the land to be lower than the above estimate. Though flux measurements over the land to the north-west could not be reasonably measured (due to lacking winds and the steep slope rising rapidly above the observation point), a value for land and sea can be estimated by calculating a least square solution for the footprint land cover in Figure 2.16 and the median deposition velocities that correspond to those bins (Figure 2.14). Using all data from 2–13 m s^{-1} yielded values of 0.167 ± 0.080 cm s^{-1} and 0.034 ± 0.016 cm s^{-1} for land and sea respectively, suggesting a lesser effect from land than estimated previously. The sea-only value is clearly still brought up to some extent by the lowest wind bins. Deposition velocity values were adjusted by subtracting the v_d value obtained here for the land multiplied by the land contribution for the given wind bin from Figure 2.16 from the observed v_d for each averaging period, the overall values of which are given in Table 2.2.

Table 2.2: Median v_d values for each period before and after adjusting for land influence

Period	Unadjusted median v_d / cm s^{-1}	Adjusted v_d / cm s^{-1}
Apr/May 2018	0.035	0.030
Dec 2019	0.028	0.027
Jan 2020	0.015	0.013
Feb 2020	0.038	0.033
May 2020	0.028	0.023
Jun 2020	0.028	0.021
Jul 2020	0.033	0.026
Aug 2020	0.024	0.021
Feb 2021	0.030	0.026
Mar 2021	0.008	0.007
Apr 2021	0.013	0.010
May 2021	0.019	0.017

In deployment 1, this suggests the land is contributing ~14% to the unadjusted v_d. The adjustment varies in magnitude across deployments, as periods with greater average wind speeds will be less affected. These adjusted values should be most representative of the deposition over the water and will be used in Chapter 3 for comparisons to existing models.

2.7 Flux Uncertainty

Given the scatter present in data across all deployments, it is important to consider the errors associated with the flux and deposition values. The significance of the data can be considered in a number of ways, as can the random error – uncertainty in the flux measurements due to variations, both artificial and natural, between the time periods of observations.

As an initial check, the distribution of deposition velocities obtained when using an improbably lag time can be used to identify to test whether the measured deposition velocities are statistically significant. Histograms of the accepted deposition velocities from deployment 1 as well as those values from the data 'disjoined' by a fixed lag time of 40 s are shown in Figure 2.19.

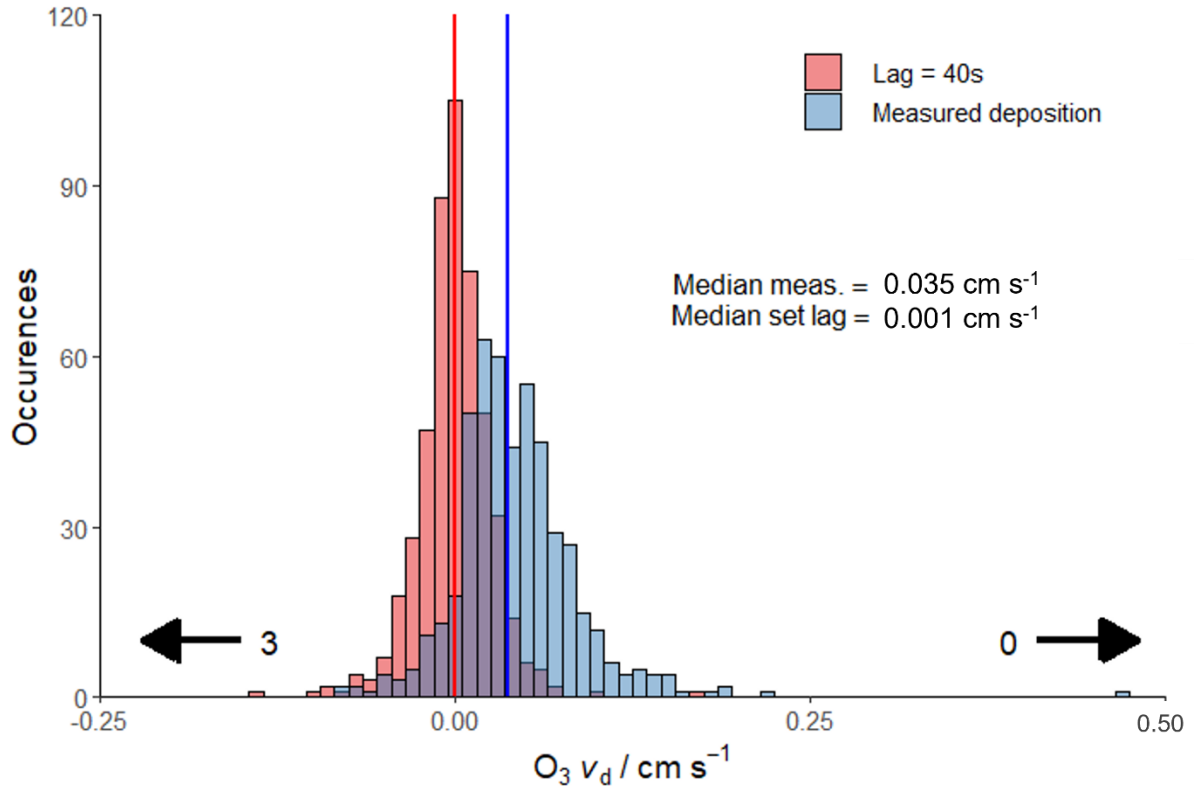

Figure 2.19: Two histograms of deposition velocities from deployment 1: the accepted values in blue, and the values obtained when using a fixed, unrealistic lag time of 40 s in red. Median values for each distribution are shown by vertical lines of their respective colours.

Firstly, a Kolmogorov-Smirnov test determined the accepted deposition values to be significantly different from the values generated with incorrect lags, rejecting the null hypothesis that both sets of data could have been taken by chance from the same distribution. With a lag so much greater than what is realistically observed, no meaningful correlation between vertical wind and ozone would be expected to generate flux, and hence deposition. The closeness of the median of the disjoined depositions to 0 suggests a reasonable accuracy; that the data processing and subsequent filtering are not, on average, biasing the deposition velocity high or low. It is apparent however that considerable scatter exists within the data that is not caused by a true variation in flux. This error can be assessed in a number of ways.

As mentioned, at an extreme lag time (away from the true value) there is not expected to be any 'real' correlation between vertical wind and ozone concentration. That is to say that any correlation observed is a result of random noise in the covariance. As such, an empirical limit of detection (LoD) for a given flux measurement can be established by measuring many covariance values at improbable lag times (150 – 180 s) and taking the standard deviation in those values, as per Langford et al. (2015)[163] who define random error as:

$$RE_{RMSE} = \sqrt{\left(0.5\left(\left(\sigma_{f_{w'c'}[-\Gamma]}\right)^2 + \left(\overline{f_{w'c'}[-\Gamma]}\right)^2 + \left(\sigma_{f_{w'c'}[+\Gamma]}\right)^2 + \left(\overline{f_{w'c'}[+\Gamma]}\right)^2\right)\right)} \quad (12)$$

where $\sigma_{f_{w'c'}}$ and $\overline{f_{w'c'}}$ are the standard deviation and mean of the cross covariance within the time window Γ. The RE defined in Eq. 12 can be considered as a 1σ LoD based on random noise or multiplied up to give different confidence intervals. This cross-covariance function used is akin to the cross-correlation shown in Figure 2.9, except quantitatively measuring mass flux. Note that this yields mass flux values, which are presented with those for each deployment in Table 2.3.

Table 2.3: Average mass flux values and limits of detection (1σ) for each deployment (deployments 1, 2 and 3 shaded white, grey, and blue, respectively). Since LoDs were determined individually for each averaging period, a percentage is also given for the number of fluxes beyond the corresponding determined LoD.

Period	Median flux / mg m^{-2} h^{-1}	Total accepted observations	Median 1σ LoD / mg m^{-2} h^{-1}	Values above 1σ LoD / %	Values above 2σ LoD / %
Apr/May 2018	-0.1222	432	0.0580	80.8	59.7
Dec 2019	-0.0874	134	0.0696	74.6	50.0
Jan 2020	-0.0475	47	0.0435	53.2	34.0
Feb 2020	-0.1112	106	0.0649	75.4	45.3
May 2020	-0.0850	140	0.0541	72.1	48.6
Jun 2020	-0.0670	225	0.0481	76.0	51.6
Jul 2020	-0.0537	275	0.0438	69.8	45.8
Aug 2020	-0.0577	208	0.0494	69.2	48.1
Feb 2021	-0.0908	124	0.0428	77.4	56.4
Mar 2021	-0.0250	125	0.0482	56.8	30.4
Apr 2021	-0.0502	116	0.0317	73.3	49.1
May 2021	-0.0631	584	0.0337	73.3	51.4

Since the distributions of fluxes/deposition velocities crosses 0, there are inevitably some measurements which fall below the limit of detection. In general, however, approximately 70% of individual flux values exceed their 1σ limit of detection except where fluxes were particularly low (January 2020 and March 2021). Recalling the different instrumentation used between deployments, measurements in 2021 suggest that the more sensitive AQD results in lower LoDs. Additionally, LoDs for deployment 2 are similar to those from deployment 1, despite the CLD86 being less sensitive during deployment 2. This is a result of the increase in averaging interval from 20 minutes to 60 minutes. For comparison, calculating 20-minute fluxes and LoDs for August 2020 results in a

median 1σ LoD of 0.0718 mg m^{-2} h^{-1}, with only 60.8% and 28.2% of values exceeding the individual 1σ and 2σ LoDs respectively.

An alternative method for calculating random sampling error is that of Mann and Lenschow (1994)[164], which uses the integral turbulence timescale (ITS), represented as τ_{wca}. Physically, this represents the size of eddy accounting for most of the flux, and can be estimated by integrating the cross-correlation function of ozone and vertical wind (such as in Figure 2.9) from the peak onwards:

$$\tau_{wca} = \int_0^\infty r_{w'c'}(t)\, dt \tag{13}$$

where $r_{w'c'}$ is the cross-correlation function at time *t*. In theory, the CCF should rapidly decay to zero from the peak, but in reality, the presence of noise causes the CCF to fluctuate around zero. This therefore presents a choice over what period to perform integration. In this work, the integration stops at the first instance of the CCF crossing 0, though fixed time periods can also be used. With τ_{wca} defined, the authors define relative errors as:

$$\frac{\sigma F}{F} = \left(\frac{2\tau_{wca}}{T}\right)^{0.5} \left(\frac{1+r_{w'c'}^2}{r_{w'c'}^2}\right)^{0.5} \tag{14}$$

The random error values calculated using Eq. 13 and Eq. 14 are presented in Table 2.4 alongside the LoDs from the Langford method as well as errors calculated by a very similar method using ITS from Fairall et al. (2000)[165]:

$$\sigma F = \sigma\overline{w'c'} \approx \frac{Q\sigma_w\sigma_c}{\sqrt{T/\tau_{wca}}} \tag{15}$$

where *w*' is instantaneous vertical wind velocity fluctuation, *c*' is instantaneous ozone fluctuation, σ_w is the standard deviation in vertical wind velocity, σ_c is the standard deviation in ozone concentration, *T* is length of the averaging interval in seconds, and τ_{wca} is the integral timescale for the instantaneous covariance time series *w'c'*. This is partially a rearrangement of Eq. 14; the ITS and averaging period term is the same, but simple standard deviations of wind and ozone are used in place of correlation coefficients. A factor, Q, with a value of 1–2 is sometimes also included in the numerator of Eq. 15 to reflect uncertainty in this relationship[166]. Eq. 14 effectively has a factor of $2^{0.5}$ applied, and so that value is used here for consistency. As an alternative to the cross-correlation method discussed above, the integral timescale τ_{wca} can instead be determined from a flux co-spectrum peak frequency:

$$\tau_{wca} = \frac{1}{2\pi f_{max}} \tag{16}$$

or empirically according to:

$$\tau_{wca} = \frac{bz}{U} \tag{17}$$

where z is measurement height in meters, U is mean wind speed, and b is a value that varies with atmospheric stability. Ideally, a cospectrum for each averaging interval would provide a clear peak and thus a value for τ_{wca} for each measurement. In practice however, individual cospectra are very noisy due to the small fluxes relative to our detection limits. Therefore, a sample of data from deployment 1 (17th April 2018) were used to generate a clearer cospectrum (Figure 2.20).

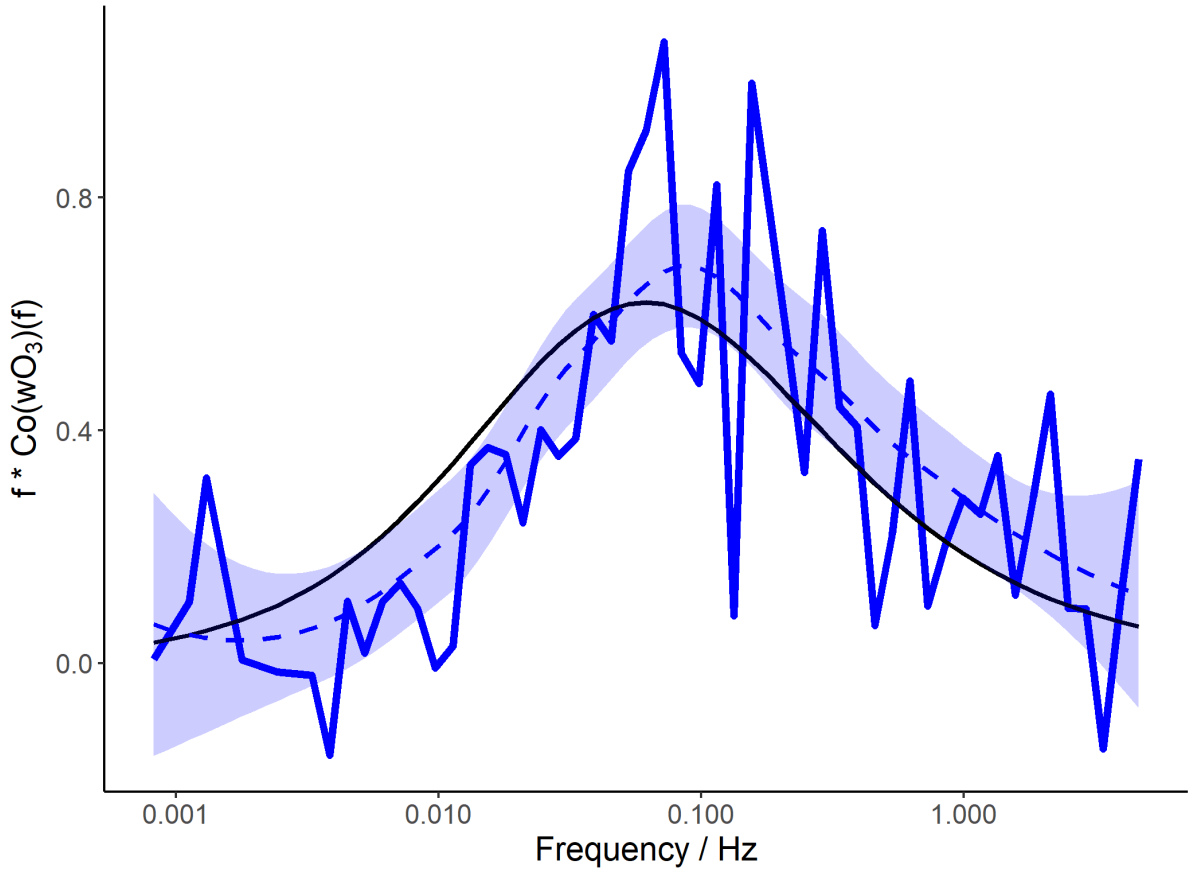

Figure 2.20: Average ozone flux cospectrum for the 17th of April, normalised to area = 1, shown in blue with a smoothed local regression (LOESS, dashed line) and 95% confidence interval (blue shading). Wind speeds were 10.3 – 12.3 m s^{-1} and dimensionless Obukhov lengths were 0.14 – 0.17, representing near neutral, slightly stable conditions. Expected co-spectral shape predicted by Kaimal et al (1972) shown in black.

The peak of the cospectrum in Figure 2.20 (0.07 Hz) can be used to calculate τ_{wca} using Eq. 16, giving a value of 2.2 s. This value however reflects a certain environment, and would vary with wind speed and atmospheric stability. Effective measurement height due to tide could also have an effect. Therefore to alleviate these variations, a value of b in Eq. 17 was calculated back from the obtained τ_{wca}, giving 1.5. This seems to agree reasonably well with existing measurements, where the value of b has been reported variably as 0.3–3 for near neutral conditions[166,167] and on the order of 10–12 for convective/unstable conditions[166,168]. Therefore a value of b = 1.5 was used in Eq. 17 with the correct heights and wind speeds to calculate an uncertainty for each averaging interval. Though the value of b varies with stability, the stability conditions across all deployments were typically near-neutral.

Values of the dimensionless stability parameter z/L typically range from -5 to 5, with negative values indicating instability, positive values stability, and near-zero values neutrality. Observed interquartile ranges for the z/L were -0.139 – 0.135, -0.136 – 0.074 and -0.172 – 0.066 for deployments 1, 2 and 3 respectively. The resulting values of σF from the Mann and Lenschow method and the Fairall method are given in Table 2.4 alongside those LoDs determined from Langford method previously.

Table 2.4: Median limits of detection determined by the Langford method and median random uncertainty values (σF_{O3}) calculated according to Eqs. 14 and 15. Deployments 1, 2 and 3 shaded white, grey, and blue, respectively. Note again that deployment 2 used an averaging period of 60 minutes, rather than 20 minutes as in deployments 1 and 3. Due to an error, a Mann and Lenschow error value for January 2020 was not calculated.

Period	1σ LoD (Langford) / mg m^{-2} h^{-1}	σF_{O3} (Mann & Lenschow) / mg m^{-2} h^{-1}	σF_{O3} (Fairall) / mg m^{-2} h^{-1}
Apr/May 2018	0.0580	0.0808	0.3352
Dec 2019	0.0696	0.1031	0.4400
Jan 2020	0.0435	-	0.2822
Feb 2020	0.0649	0.0915	0.4083
May 2020	0.0541	0.0769	0.3418
Jun 2020	0.0481	0.0695	0.2952
Jul 2020	0.0438	0.0619	0.2853
Aug 2020	0.0494	0.0725	0.3424
Feb 2021	0.0428	0.0660	0.2295
Mar 2021	0.0482	0.0743	0.3054
Apr 2021	0.0317	0.0362	0.1646
May 2021	0.0337	0.0483	0.1946

Both sets of values of σF_{O3} are higher than the 1σ LoDs determined from the Langford method, though far more so in the case of the Fairall values. That said, while the Langford method does assess random error to formulate a LoD, it does do in a fundamentally different way to the other two methods; it examines the noise surrounding the covariance peak rather than the shape of the peak itself. It is therefore expected for the values to be slightly different. The method of Fairall does give random error values aproxiamtely 4 times that of Mann and Lenschow though. One principle difference between the two is the method in which the ITS is calculated - from a cospectrum in the former and from CCF in the latter. Comparing the values for τ_{wca} from each method however revealed good consistency. The IQR of τ_{wca} values for May 2021 were 1.17 – 3.93 s and 2.20 – 3.18 s as determnied from Eqs. 13 and 17 respectively. Rather than the ITS, the source of the difference between the two methods stems from the simplified use of standard deviations of ozone and wind in

Eq. 15. This causes higher random error values than the use of the correlation coefficients, possibly as a result of much of the deviations originating from random noise that may produce little correlation.

Random errors from all 3 methods do however follow a similar pattern, with December 2019, February 2020 and March 2021 having higher LoDs and uncertainty than other months within the same deployment. It should be noted that the values of σF_{O3} are an estimation; Lenschow and Kristensen (1985)[167] used a Q value of 2 in Eq. 15 to obtain an upper limit on random uncertainty. All approaches point to the standard deviation in ozone concentrations and in vertical wind driving the flux uncertainty. An amount of this variation is natural, though there is potential for instrument white noise to play a part. Visually, the lower errors and ozone standard deviations obtained during deployment 3 with the more sensitive AQD instrument suggests that white noise is important, and this can be quantified using autocovariance. Autocovariance is calculated is the same way as cross-covariance, except the same data (in this case ozone mixing ratio) is used rather than 2 different datasets. Since white noise is random, it will only contribute to the variance at zero time offset. Therefore, the white noise component in a variance can be estimated as the difference between the first and second points in an autocovariance spectrum, such as Figure 2.21.

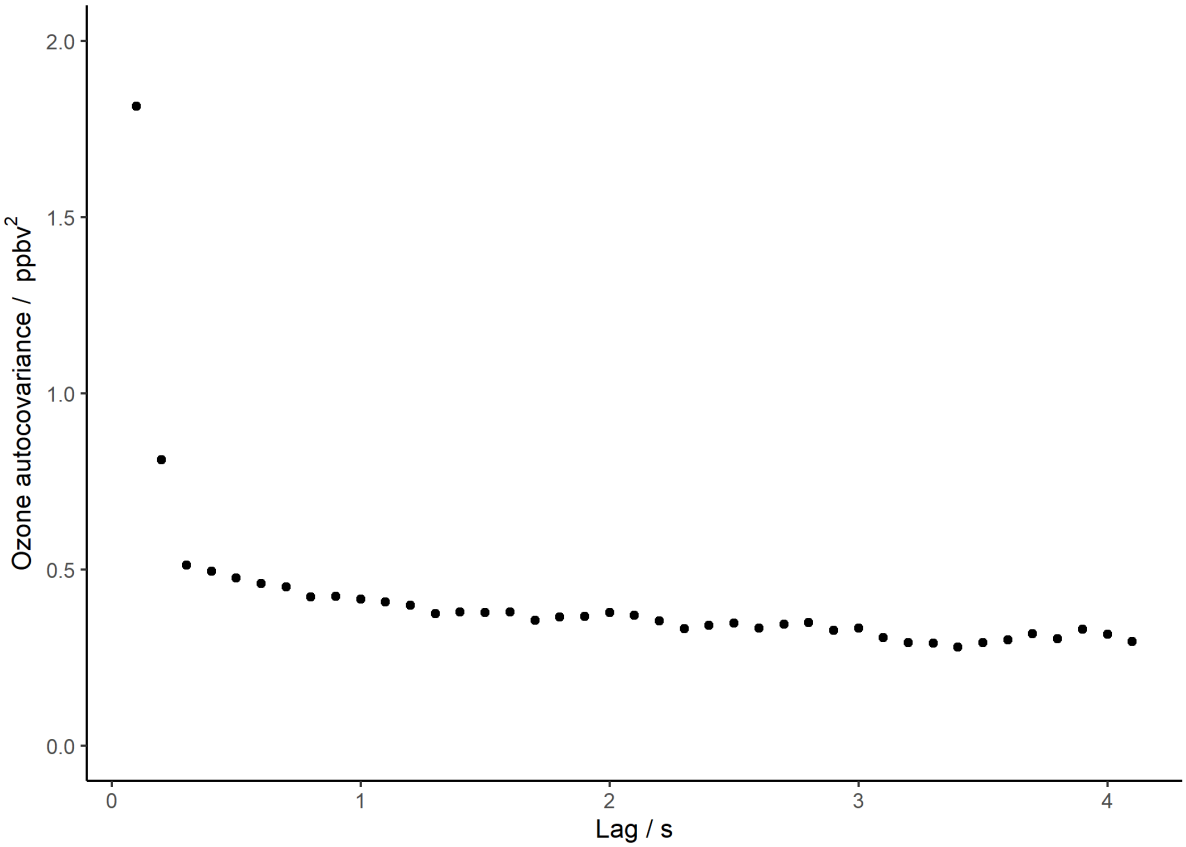

Figure 2.21: Autocovariance spectrum for ozone data from 19th April 2018 at 3pm during deployment 1. The contribution of instrument noise can be approximated as the difference between the first 2 points along the x axis.

In deployment 1, the method above suggested that between 45 and 98% of ozone variance (10^{th} – 90^{th} percentile) was caused by white noise in the instrument. While this is obviously a major proportion, the extent to which it influences the covariances, and hence fluxes, ought to be somewhat less due to its random nature leading to little correlation with wind. To examine this, a 1σ LoD was determined using the wind data from deployment 1, but using artificial ozone data with a fixed standard deviation of 1.4 ppbv (the mean deviation observed for the real ozone data). The resulting median 1σ LoD was 0.0388 mg m^{-2} h^{-1}, suggesting that white noise in the ozone data may be responsible for as much as 67% of the 0.0580 mg m^{-2} h^{-1} 1σ LoD obtained with the real data. This represents an upper estimate for contribution from white noise by assuming effectively all the variation in ozone mixing ratio was a result of noise. Since this is a large portion of the overall observed LoD, the quality of the ozone instrument used remains an important factor for this work, and an improvement in instrument sensitivity could considerably reduce the uncertainties associated with the fluxes.

2.8 Conclusions

Eddy covariance measurements were successfully conducted at the PPAO in 3 deployments spanning from April 2018 until May 2021. Fluxes were calculated using 20 minute averaging periods during deployments 1 and 3, and a 60 minute averaging period in deployment 2 to help compensate for a drop in instrument sensitivity. In order to best observe the marine sector, only periods with southwesterly winds in the 180-240° from north sector were accepted, with filters also applied to the standard deviations of ozone and wind direction to avoid periods of non-stationarity.

Observations at low wind speeds yielded results unexpected for a marine environment; deposition velocity increased at low wind speed contrary to existing obervations and models. Roughness length also increased more than expected, implying the wind data was being affected by the land on which the observatory is built. Therefore a windspeed threshold of 4 m s^{-1} was applied to all data in an effort to avoid the presence of land from influencing the observations. Due to the position of the PPAO, zero land influence in the fluxes is impossible, and so the extent to which remaining observations may be biased upwards by land was assessed using a footprint parameterisation, defining the area being observed during a given flux period. A v_d of 0.167 ± 0.080 cm s^{-1} was estimated for the land around the PPAO, and together with the land cover present in footprints at different wind speeds, this was used to adjust the remaining data to represent deposition solely to water. These are the values taken forward for comparisons to models in Chapter 3.

The amount of random uncertainty in individual flux averaging periods was also assessed in a number of ways. Overall, uncertainty was high on each single flux period relative to the flux magnitude across all deployments, with both random sampling error and instrument noise playing a role. Flux values

from individual averaging intervals are therefore of limited value. Data are therefore grouped into monthly datasets from which links to meteorology and biogeochemistry can be investigated in Chapter 3.

3. Biogeochemistry at the PPAO: Implications for Ozone Deposition Models and Observations

3.1 Introduction

Iodide in seawater is known to react with ozone, and dissolved organic carbon (DOC) is thought to be similarly important. Long-term measurements of ozone deposition at the PPAO presented an opportunity to simultaneously collect samples from the surrounding waters to characterise the chemical make-up of the surface being observed. In this chapter, measurements of both iodide and DOC are reported, and used with existing ozone deposition models to assess their importance at the PPAO. The extent to which models and observations depend upon meteorological conditions such as water temperature and wind speed are also investigated.

3.2 Methodology

3.2.1 Seawater Sampling

Seawater samples were collected approximately weekly near Penlee Point from the 11th of November 2019. The majority of samples were collected within the estimated flux footprint depending on the direction of the prevailing wind at the time. Some samples were also collected from the L4 buoy located approximately 8 km south of the PPAO (see Figure 3.1).

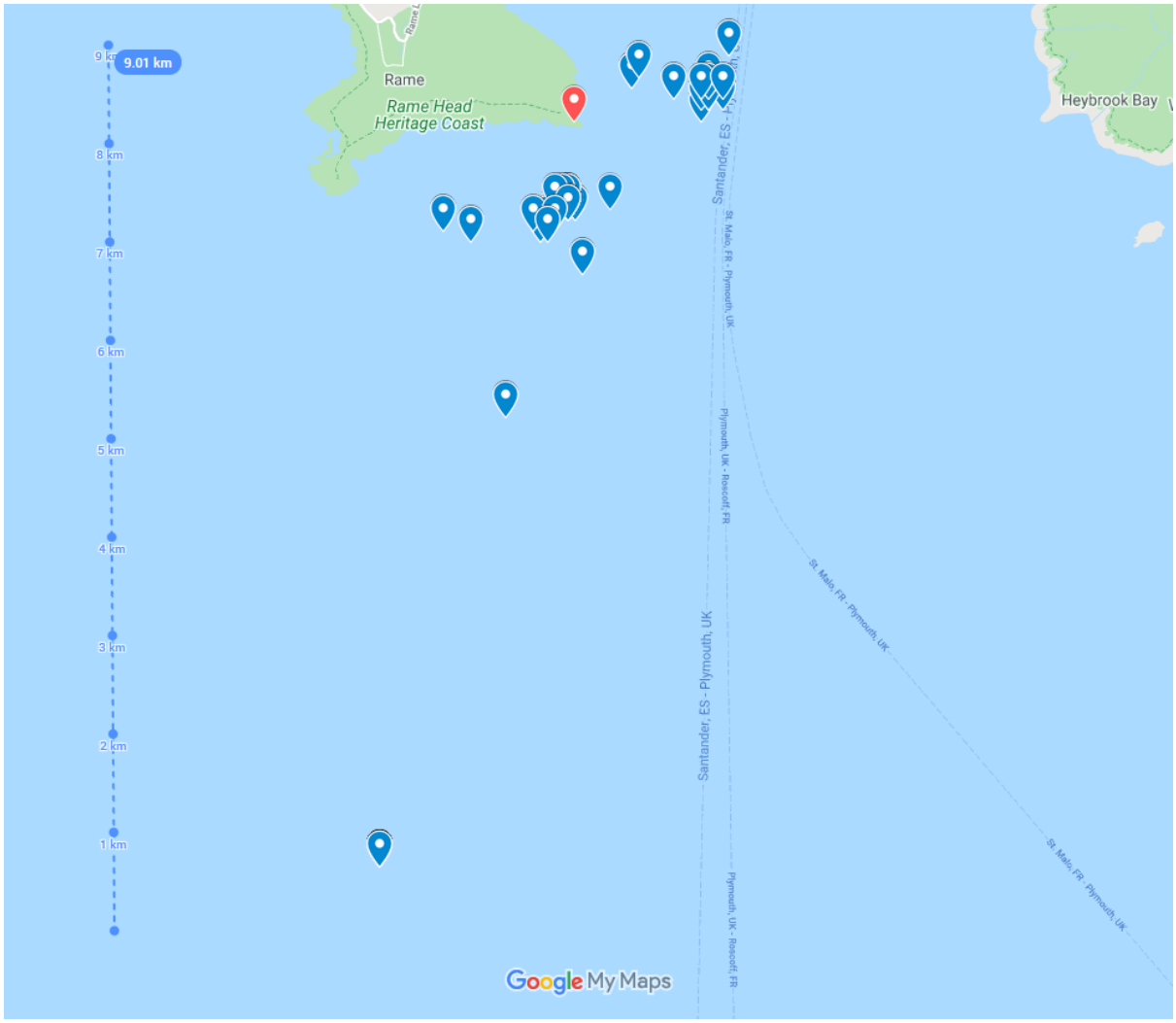

Figure 3.1: Locations of water sample collections since 11th November 2019 (blue) near the PPAO (red). Samples are collected a few kilometres upwind of the PPAO where possible. Some samples were collected during routine visits to the L4 buoy (southern-most point). © Google

Each week, samples were taken from both the underlying water (ULW) and the SML. The underlying water was collected at ~3 m (depending on ocean swell) below the surface using the underway system onboard the Plymouth Quest, a research vessel at PML. The only exception to this was the collection of ULW by hand using the PML Explorer, a smaller RIB, when the Quest was unavailable on 28th November 2019. The collection of SML samples is more complex. Common methods of collection include either the use of a Garrett screen[169] or a glass plate[170], the former of which was used in this case in order to maximise the volume of water available for analyses. A Garrett screen is comprised of an area of steel mesh held flat within a frame, similar to a sieve. This is submerged in the water with the flat surface parallel to the water surface, before being drawn slowly upwards out of the water. Upon leaving the water, the water at the surface adheres to the pores in the mesh due to surface tension, allowing for the collection of a thin layer of water - the SML. This can then be drained into a collection vessel. The thickness of the layer of water collected can be estimated by dividing the total

volume of water collected by the number of times the screen was drawn up. For the SML samples around the PPAO, the sample thickness was 647 ± 55 µm (mean and standard deviation).

Samples were collected for many different measurements, being filtered through glass fibre filters and frozen for shipment to York for analysis. Those of inorganic iodine and dissolved organic material are of particular significance in the modelling of ozone deposition (Section 3.2.4) and will be covered in the sections that follow.

3.2.2 Inorganic Iodine Analysis

As mentioned in Section 1.4, inorganic iodine exists throughout the ocean predominantly as iodide (I^-) and iodate (IO_3^-), the former of which is understood to be particularly reactive to ozone at the air-sea interface[70].

Accurate concentrations of iodide in sea water can be determined by cathodic stripping square wave voltammetry[171], in which iodide is first concentrated on a mercury drop electrode via electrolytic deposition. Following this, the voltage is varied in a cathodic sweep, and the measured current in each step reflects the aqueous concentration of iodide from reduction at the mercury electrode. In this work, a standard addition method was used with a Metrohm 663 VA Stand with IME663 interface and potentiostat. Potential was varied from -0.1 V to -0.7 V in 0.002 V steps, with a pulse size of 0.2 V and current measurements taken at 25 Hz. The system used a hanging drop mercury electrode, an auxiliary electrode of either platinum or glassy carbon, and a reference electrode of Ag/AgCl in 3 mol dm^{-3} KCl. 12 ml of sample with 90 µL of 0.2% v/v Triton™-X100 in water were purged with nitrogen in the glass reaction cell for 5 minutes. A series of 6 measurements were then taken, with a peak around -0.28 to -0.25 V (light blue in Figure 3.2). A series of 3 standard addition of KI standard (2×10^{-5} mol dm^{-3}) were then made, typically 30 – 70 µL depending on the initial signal strength. Repeated measurements were made after each addition, from which a linear fit could be interpolated backwards to determine the initial iodide concentration of the sample. A typical series of measurements on a sample are shown in Figure 3.2.

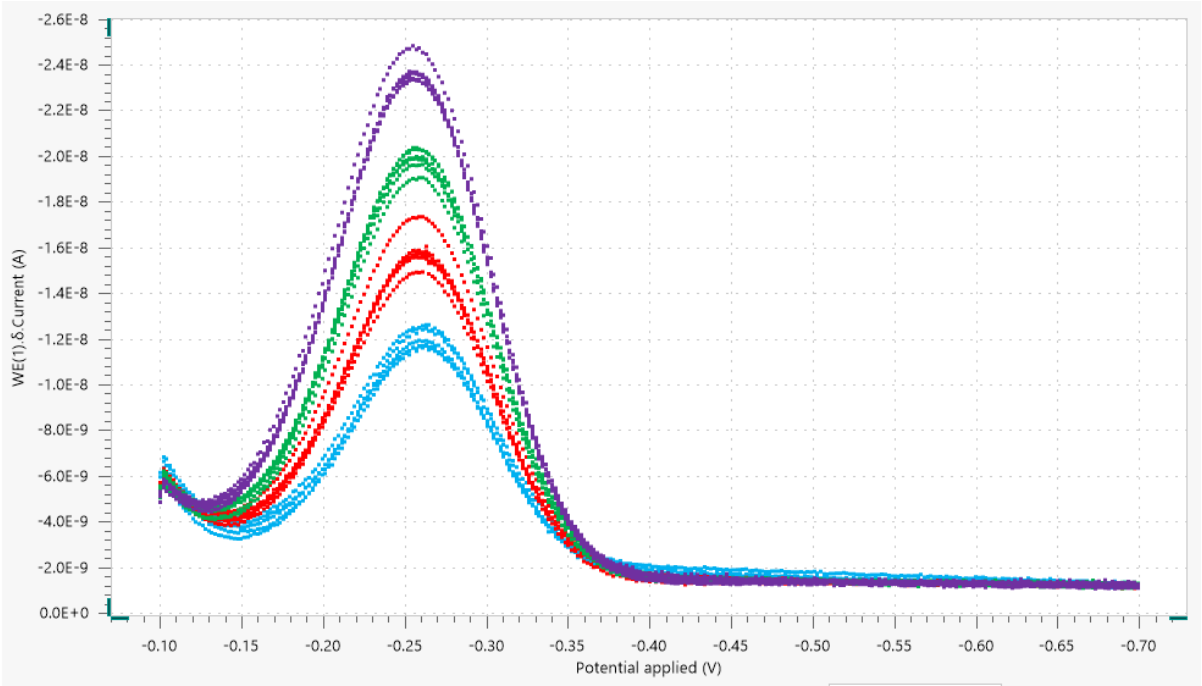

Figure 3.2: Measured current peaks from cathodic stripping square wave voltammetry measurements for a typical iodide sample. Light blue, red, green, and purple lines represent the original sample, and the 1st, 2nd, and 3rd standard additions respectively. Each point is a measurement in a sequence, with 6 sequences being measured at each addition.

3.2.3 Dissolved Organic Carbon (DOC) Analysis

Dissolved organic carbon (DOC) refers to the fraction of total organic carbon (TOC) which passes through a glass fibre filter, typically of pore size ~0.4 µm. A complex mixture of many distinct chemical compounds, it has been shown to be of comparable important in determining the reactivity of ozone at the sea surface as iodide[74,172]. Therefore, quantification of DOC present in the samples collected within the flux footprint is essential to consider when predicting the reactivity of the sea surface towards ozone. This was achieved by measuring the remaining carbon in the samples after filtering using an Elementar vario TOC cube. This works by heating the sample (680 - 1200 °C) in an oxidising atmosphere, converting carbon-containing compounds into CO_2, which in turn is quantified by IR spectrometry. Since the percentage mass of carbon vs other elements in the dissolved organic material (DOM) is not known, only DOC values are reported here as 'moles/mass of pure carbon', converted between using the molar mass of carbon (12 g mol^{-1}).

3.2.4 Ozone Deposition Models

Two related models for ozone deposition are examined in this work. Both formulate values for the 3 resistances, R_a, R_b and R_c, described in Section 1.3 (Eq. 2), and differ in their determination of the most important R_c term. The first model is the 1-layer model of Fairall et al. (2007)[76], and the second the revised 2-layer model of Luhar et al. (2018)[149].

For consistency, R_a and R_b are calculated in the same way for both models. From Chang et al. (2004)[69], the atmospheric resistance, R_a is defined as

$$R_a = \frac{U(z)}{u_*^2} \tag{18}$$

Where $U(z)$ is the windspeed at the measurement height (19 m) and u_* is the friction velocity (both m s^{-1}). The laminar resistance R_b is defined as

$$R_b = \frac{5}{u_*} Sc^{\frac{2}{3}} \tag{19}$$

Where u_* is again friction velocity, and Sc is the Schmidt number, taken to be 0.7. As expected, these resistance values are small in relation to the surface resistance, R_c. Median values of R_a and R_b for deployment 1 were 115 s m^{-1} and 15 s m^{-1} respectively, whereas R_c values were in the thousands. This is in agreement with the observation of Lenschow et al. (1982) that R_c constituted 93-97% of total resistance[68]. In both models, R_c is defined as the reciprocal of the product of the dimensionless solubility of ozone in water (α) and the waterside deposition velocity (v_{dw})

$$R_c = \frac{1}{\alpha v_{dw}} \tag{20}$$

Where the two models differ is in their determination of v_{dw}. In the one-layer model, turbulent diffusivity in the ocean (K_t) is defined as scaling linearly with depth

$$K_t(z) = \kappa u_{*w} z \tag{21}$$

Where κ in the von Karman constant (=0.4), u_{*w} is the waterside friction velocity, and z is depth. Using the conservation budget equation for the mass of a chemical concentration in water[165], a solution for v_{dw} is presented which encompasses solubility, molecular diffusion, turbulent transfer, and the reaction of ozone with iodide.

$$v_{dw} = \sqrt{aD}\frac{K_1(\xi_0)}{K_0(\xi_0)} \tag{22}$$

Where a is the chemical reactivity of ozone with species in the water, D is the diffusivity of ozone in water, and K_1 and K_0 are modified Bessel functions of the second kind of order 1 and 0 respectively. ξ_0 is defined as

$$\xi_0 = \frac{2}{\kappa u_{*w}}\sqrt{aD} \quad (23)$$

The linear scaling of turbulent diffusivity with depth in Eq. 21 is a consequence of the prevention of large eddies forming at the surface due to the air-sea boundary. As such nearer to the surface, the vertical transport of ozone is conducted solely by molecular diffusivity, with turbulence playing a bigger role at greater depths. In the extreme case where all ozone reacts away before reaching a depth at which turbulence is relevant, the solution for ν_{dw} proposed by Garland et al. (1980)[70] is reached:

$$\nu_{dw} = \sqrt{aD} \quad (24)$$

The 2-layer model of Luhar et al. defines a reaction-diffusion sublayer (with a depth δ_m of ~3 μm) in which the effects of turbulence are negligible, and a second layer beneath in which turbulence scales as in the case of the 1-layer model. This is reasoned to be due the overestimation of K_t by Eq. 21 in the SML due to turbulent diffusion diminishing more rapidly in the viscous sublayer (~1 mm depth)[149]. Considering this reaction-diffusion sub-layer, the 2-layer scheme defines ν_{dw} as

$$\nu_{dw} = \sqrt{aD}\left[\frac{\psi K_1(\xi_\delta)cosh(\lambda)+\psi K_0(\xi_\delta)sinh(\lambda)}{\psi K_1(\xi_\delta)sinh(\lambda)+\psi K_0(\xi_\delta)cosh(\lambda)}\right] \quad (25)$$

Where the terms ψ, ξ_δ and λ in Eq. 25 all vary according to the reaction-diffusion sublayer depth, δ_m:

$$\psi = \sqrt{1+\frac{\kappa u_{*w}\delta_m}{D}} \quad (26)$$

$$\xi_\delta = \sqrt{\frac{4a}{\kappa u_{*w}}\left(\delta_m + \frac{D}{\kappa u_{*w}}\right)} \quad (27)$$

$$\lambda = \delta_m\sqrt{\frac{a}{D}} \quad (28)$$

Luhar et al. (2018) found a fixed reaction-diffusion sublayer depth of 3 μm resulted in good agreement between their model and the experimental values determined on a series of oceanic ozone flux measurements[79]. They propose the possibility of a more realistic variable δ_m by scaling it to the reaction-diffusion length scale, l_m:

$$l_m = \sqrt{D/a} \quad (29)$$

In order to compare well to the oceanic flux observations of Helmig et al. (2012), it was necessary to multiply l_m by a factor of 0.7. In subsequent work with the 2-layer model, Pound et al. (2019)[173] considered this a result of the overestimation of iodide by the use of the iodide model of Macdonald et al. (2014)[85], and found good agreement with the cruise data using the iodide model of Sherwen et al. (2019)[174] and a variable δ_m defined with no adjustment factor:

$$\delta_m = \sqrt{D/a} \quad (30)$$

It is necessary to derive or parameterise a number of inputs for the models. Firstly, waterside friction velocity u_{*w} can be calculated from measure atmospheric u_*, assuming atmospheric surface stress and waterside surface stress are equal[175]:

$$u_{*w} = \sqrt{\frac{\rho_a}{\rho_w}} u_* \tag{31}$$

Where ρ_a and ρ_w are the densities of air and water respectively. The dimensionless solubility of ozone in water, α, and the molecular diffusivity of ozone in water, D are parameterised from SST by Eq. 32[176] and 33[177].

$$\alpha = 10^{-0.25-0.013(SST-273.16)} \tag{32}$$

$$D = 1.1 \times 10^6 e^{\left(\frac{-1896}{SST}\right)} \tag{33}$$

Lastly, the chemical reactivity term, a, determines the rate of ozone deposition and the relative roles of turbulence and diffusion. This term is discussed in detail in Section 3.3.3.

3.3 Results

3.3.1 Seasonal Iodide Time Series

Although water samples within the flux footprint were only collected from November 2019 onwards, a number of ULW samples (0.5 m depth) were collected from the L4 site prior to the onset of the eddy covariance measurements. These present the chance to create a yearly profile for the site, on the proviso that the difference in site and sample depth lead to acceptably small differences. While the majority of water sampling after November 2019 was conducted within the flux footprint, a small number of samples were taken at the L4 site for comparison. The resulting iodide measurements for this period are shown in Figure 3.3, split by water layer and sampling location.

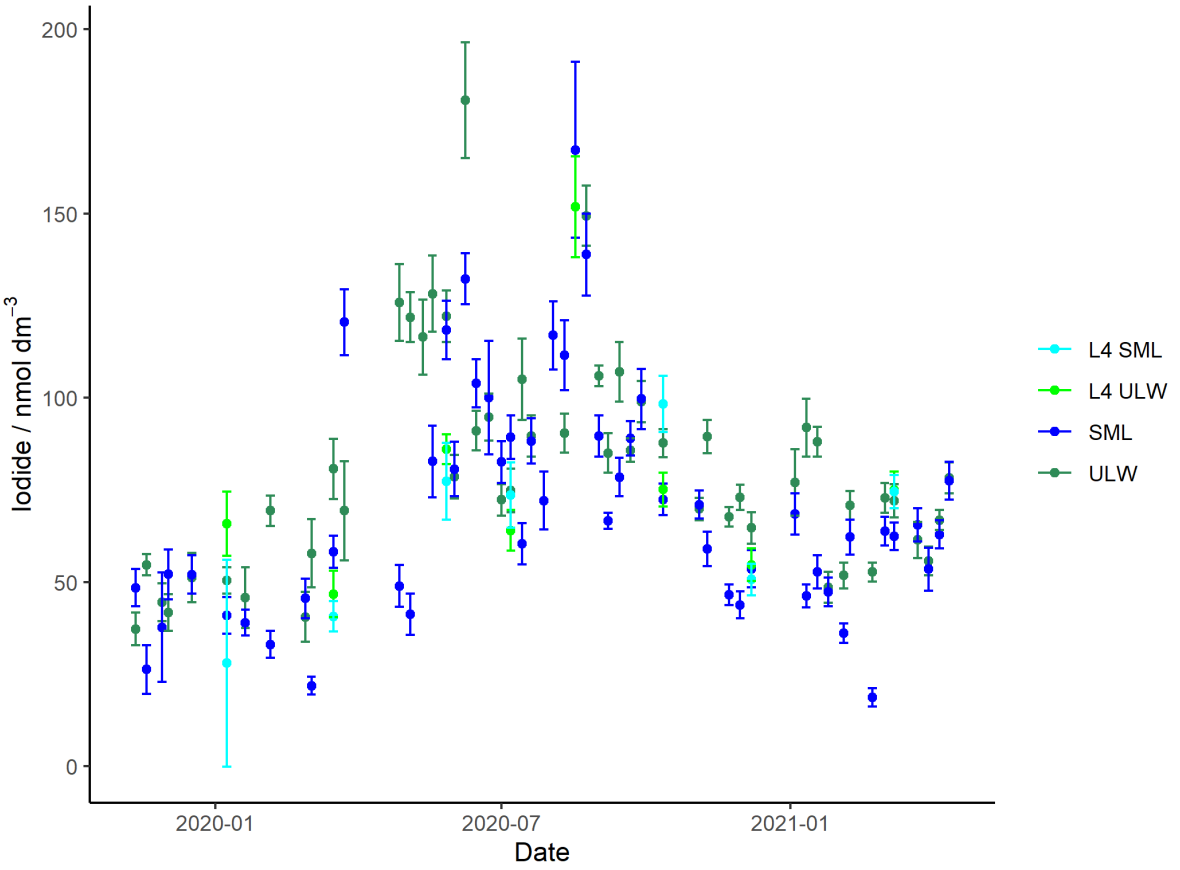

Figure 3.3: Iodide measurements within the flux footprint or at the L4 buoy since November 2019. SML samples are shown in blue, light and dark for L4 and the footprint respectively. ULW samples are shown in green, also light and dark for L4 and the footprint area. Error bars denote the RMSE of the linear fit acquired from the standard additions used to determine initial iodide concentration.

A couple of things become apparent from Figure 3.3. Firstly, though there are few samples at L4, none of them deviates particularly from the footprint samples taken in a similar period. This suggests that iodide measurements at the L4 site are likely to be reasonably representative of the footprint area on the basis of location alone. The second observation is that ULW samples tend to be slightly higher in iodide than SML samples taken on the same day at the same site, though the values are frequently within error. Lastly, there is a clear increase in iodide concentrations from around April, persisting into the summer. This coincides with increasing SST and the occurrence of annual phytoplankton blooms in the waters around the PPAO (Figure 3.4), suggesting a biological cause.

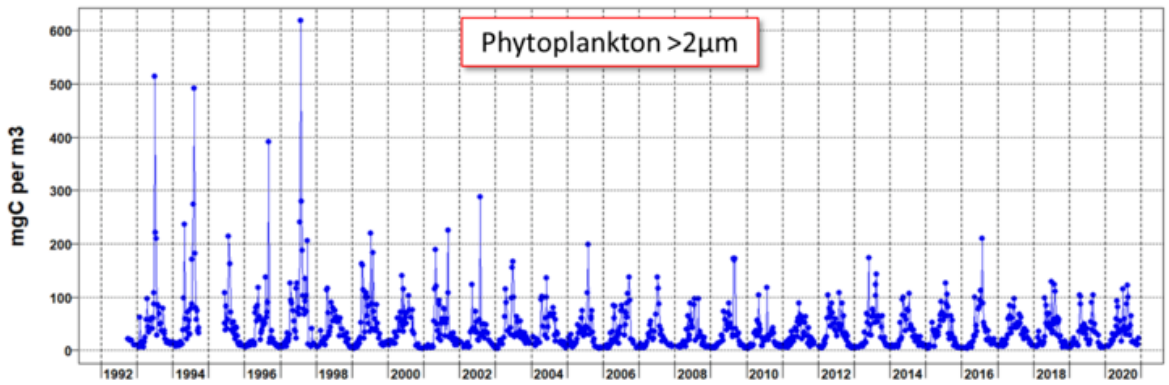

Figure 3.4: Historic phytoplankton carbon concentration at L4. Abundance increases during spring each year, falling again each autumn to a winter low. https://www.westernchannelobservatory.org.uk/l4_phytoplankton.php

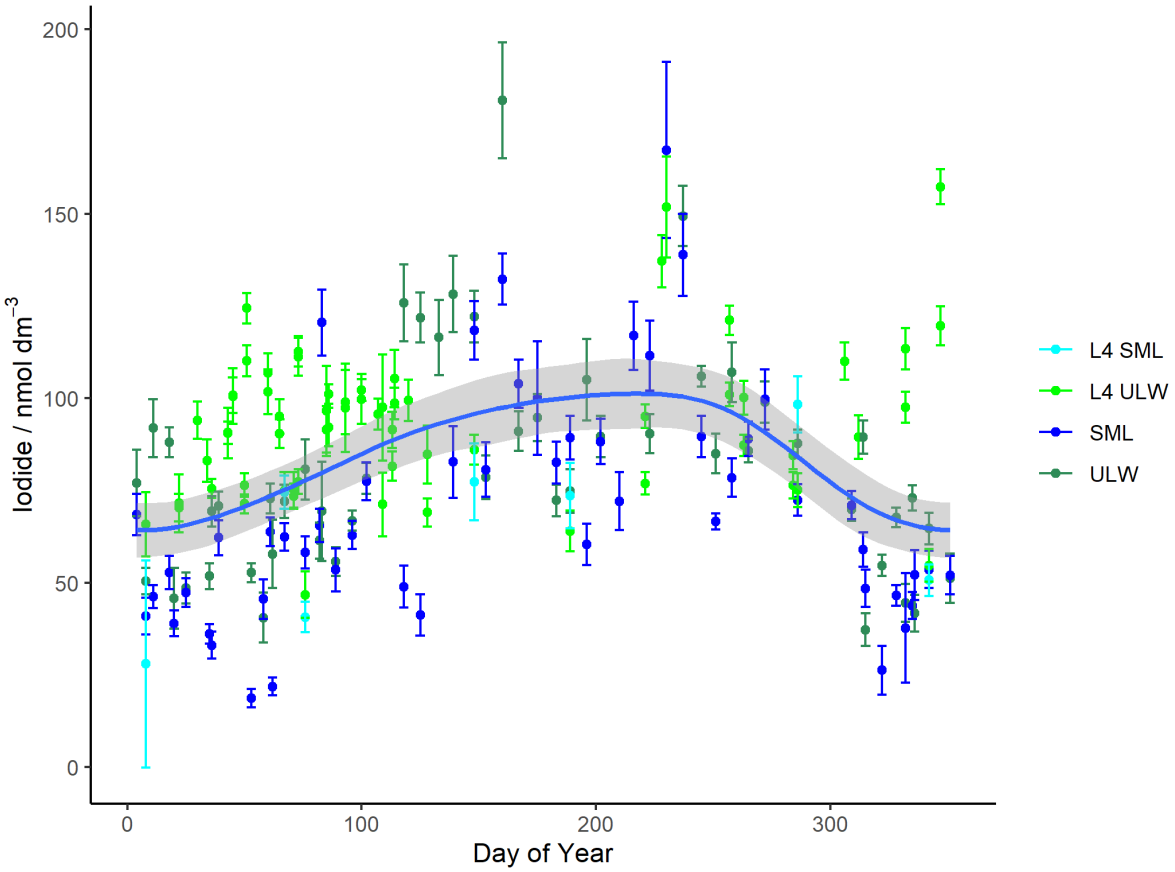

Figure 3.5: All iodide data since 2016 from the flux footprint and the L4 site plotted by day of the year. SML samples are shown in blue, light and dark for L4 and the footprint respectively. ULW samples are shown in green, also light and dark for L4 and the footprint area. Error bars denote the RMSE of the linear fit acquired from the standard additions used to determine initial iodide concentration. A general additive model (GAM) fit is shown as a solid blue line, wrapping around at the end of the year with RMSE shaded in grey.

Figure 3.5 shows all of the iodide observations since 2016 plotted on the day of year they were sampled to create a yearly profile, with a fit created by a general additive model (GAM) to allow for smooth, non-linear variation. This was generated using the 'mgcv' package in R, where the contribution to the linear predictor is some function (rather than a linear term for a linear regression for instance). A plate regression spline was used for the smoothing function, in which the contribution of a number of functions are summed to generate the smooth. Inclusion of the L4 data from 2018 and before leads to higher average iodide values - a mean concentration of 81 nmol dm^{-3} for all samples and 74 nmol dm^{-3} for samples post 2018. This is because all of the samples at L4 prior to 2019 were ULW samples which were on average higher than the SML samples. This is particularly apparent from February to April where the L4 measurements are most numerous. In these months, the GAM clearly sits above almost all SML observations, and as such its use in the prediction of iodide values to coincide with flux observations would not give concentrations representative of the SML in which the ozone-iodide reaction takes place. As this is apparently a consequence of higher iodide in the ULW, a GAM using only SML data (L4 and footprint, from 2019 onwards) will be used for iodide prediction for use in models (see section 3.3.4).

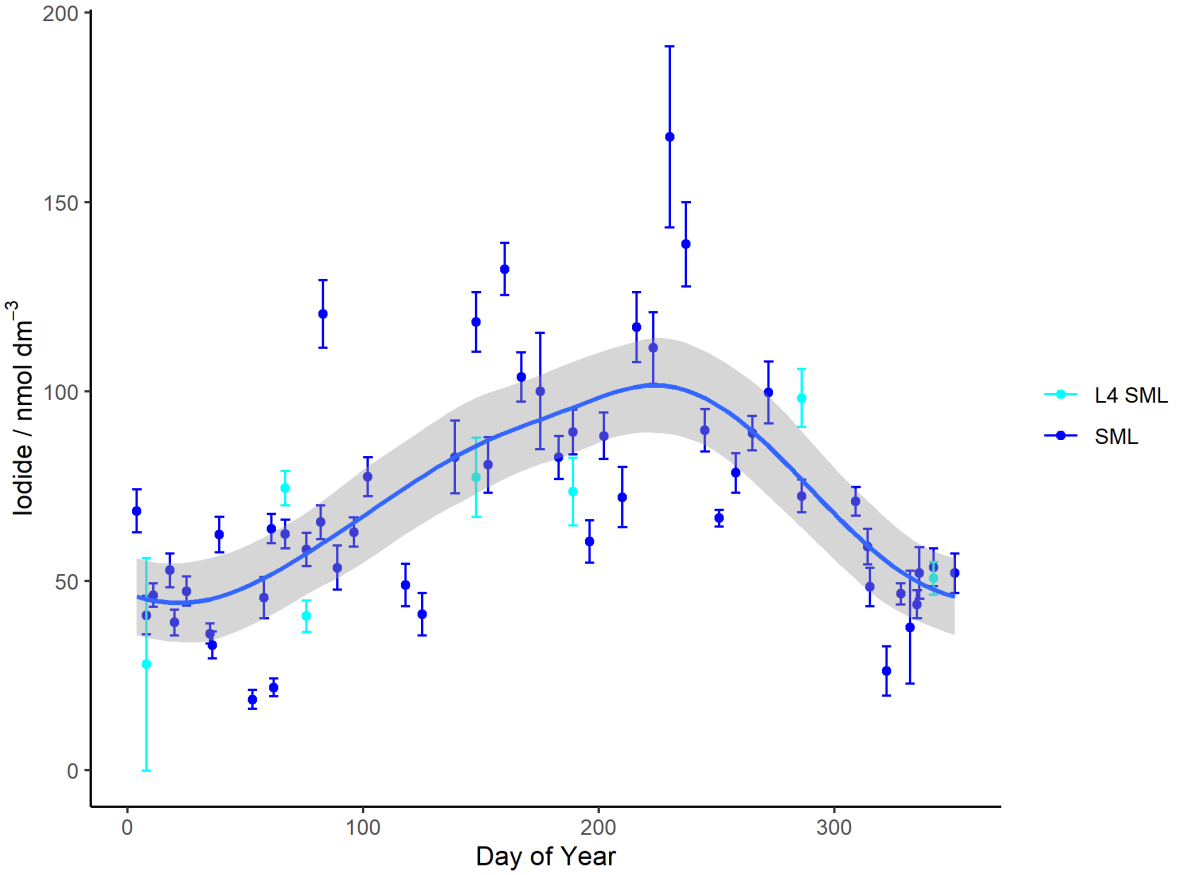

Figure 3.6: All iodide data from SML samples from the flux footprint and the L4 site (dark and light blue respectively). Error bars denote the RMSE of the linear fit acquired from the standard additions used to determine initial iodide concentration. A general additive model (GAM) fit is shown as a solid blue line, wrapping around at the end of the year with RMSE shaded in grey.

The GAM from Figure 3.6 gives much lower iodide values over the winter period (~50 nmol dm^{-3} down from ~65 nmol dm^{-3}) and better represents iodide in the SML, albeit with fewer data points to produce the model. Values in the range of 50 – 100 nmol dm^{-3} are in the typical region for oceanic iodide values. Chance et al. (2014)[85] report variable iodide concentrations in coastal region of ~30-150 nmol dm^{-3} (IQR), which these observations fit within. Sherwen et al. (2019)[174] used a collection of historical global iodide data with a machine learning regression approach to generate a high-resolution (0.125° × 0.125°) map of oceanic iodide. The monthly values generated for the nearest sector to the PPAO varied from 66 – 112 nmol dm^{-3}, again in a similar range to the observations presented here. The seasonality observed at the PPAO is not reflected in this model, though agreement over the summer period is good (see Figure 3.7).

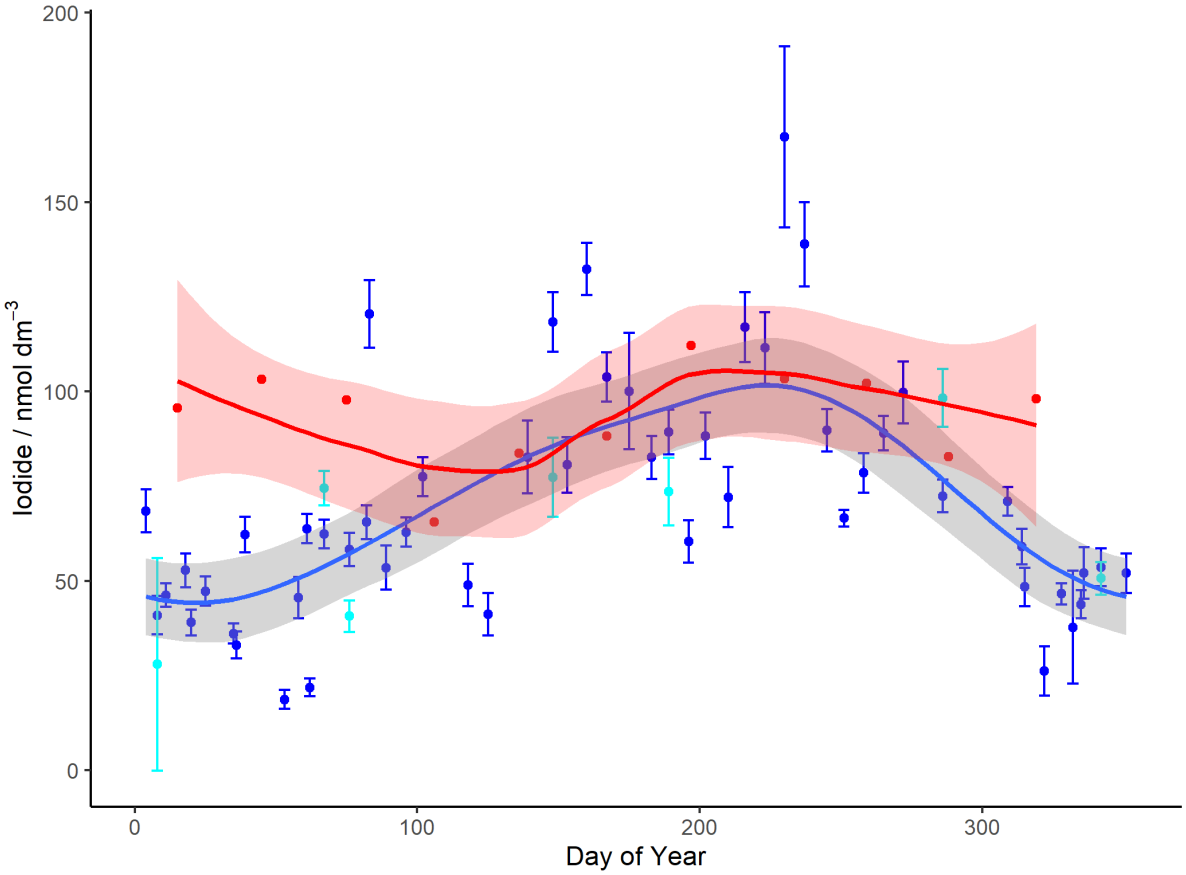

Figure 3.7: All iodide data from SML samples from the flux footprint and the L4 site (dark and light blue respectively) compared with monthly values from the model of Sherwen et al. (2019) (red), with a local regression fit, RMSE (shaded red). Error bars denote the RMSE of the linear fit acquired from the standard additions used to determine initial iodide concentration. A general additive model (GAM) fit is shown as a solid blue line, wrapping around at the end of the year with RMSE shaded in grey.

3.3.2 Seasonal Dissolved Organic Carbon Time Series

Fewer DOC samples have been analysed to date than iodide samples, but those completed are shown in Figure 3.8, plotted according to the day of year of sampling similarly to Figures 3.5 – 3.7.

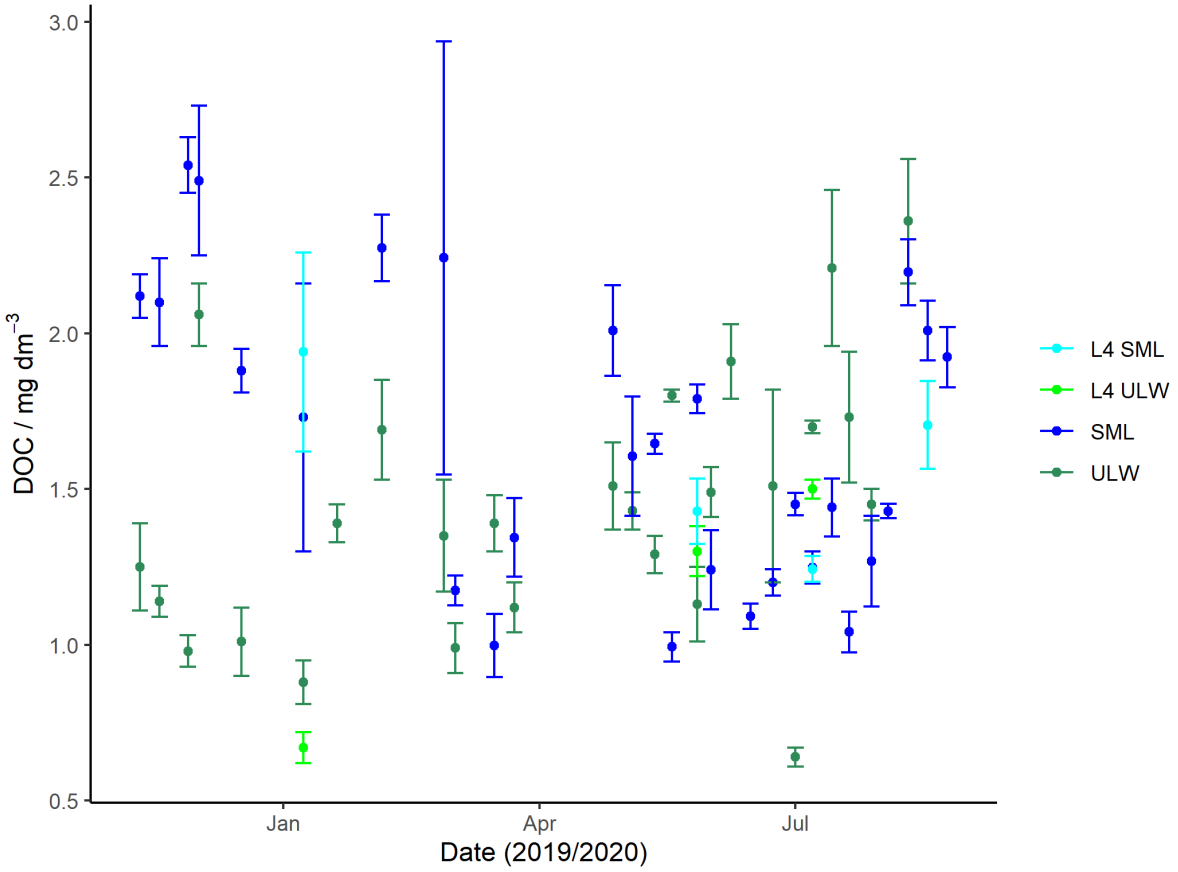

Figure 3.8: All DOC data from SML and ULW samples analysed since November 2019. SML samples are shown in blue, light and dark for L4 and the footprint respectively. ULW samples are shown in green, also light and dark for L4 and the footprint area. Error bars denote the standard deviation of replicate samples.

DOC concentrations across all sample types typically fall within 1.14 – 1.79 mg dm^{-3} (IQR), equating to molar concentrations of 95 – 149 µmol dm^{-3} (measured as moles of carbon, mass =12 g mol^{-1}). For comparison, Hansell et al. (2009)[178] report a range of typical seawater DOC values of 40 – 80 µmol dm^{-3}. The concentrations in the waters around the PPAO are generally above this global range, but this is not unexpected; higher DOC levels are often observed in coastal waters compared with open ocean due to increased biological production[179]. Interestingly, while DOC in the ULW seems to increase gradually over the course of the phytoplankton blooms occurring in spring/summer, this change is not matched in the SML. If anything, DOC within the SML appears to fall, from being considerable enhanced in the SML in December 2019 to being comparable, or even lower than the ULW in the summer. This is a surprising observation – DOC is typically higher in surface waters than deeper waters (on the scale of meters)[180]. As with the iodide data, concentrations in the SML are of

greatest relevance to the deposition of ozone, and so a GAM using only these data will be used for the prediction of DOC at the time of eddy covariance measurements.

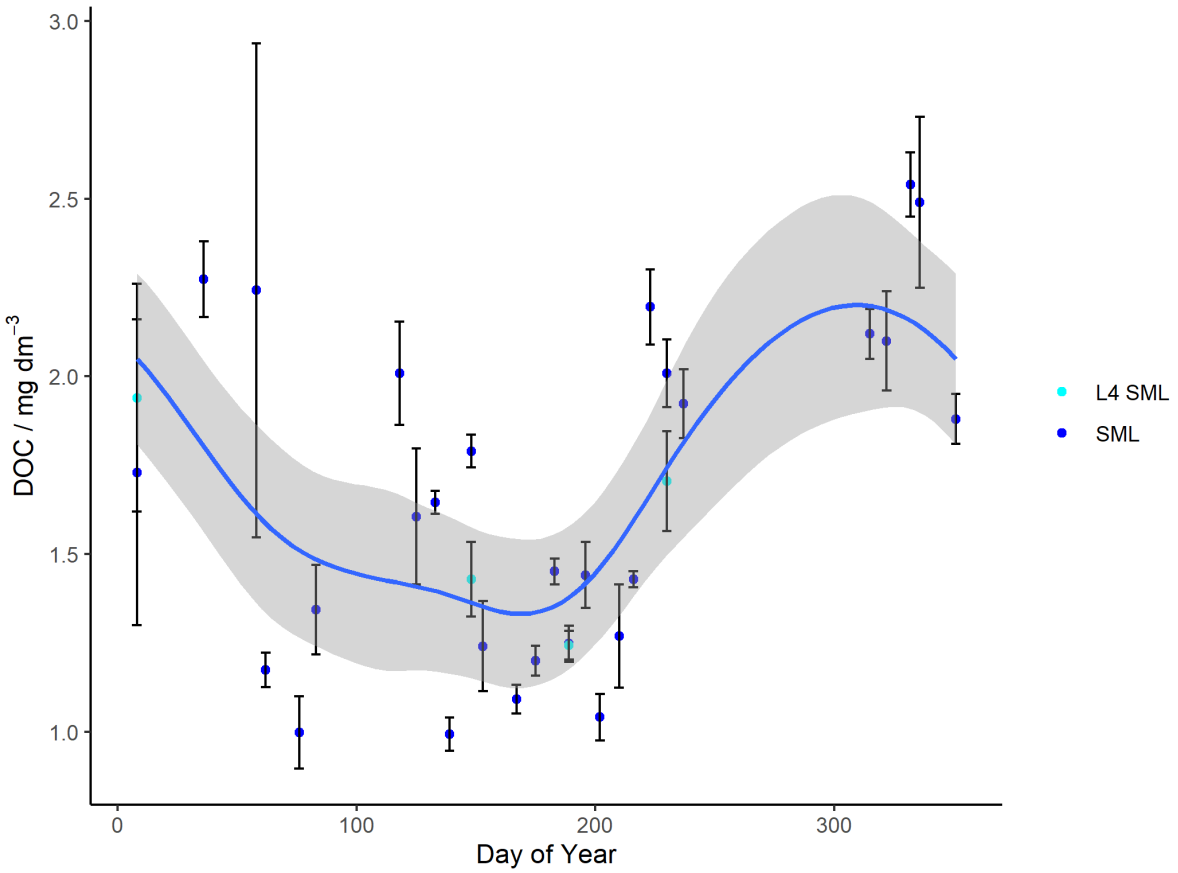

Figure 3.9: All DOC data from SML samples analysed since November 2019, plotted against day of the year. Samples are shown in light and dark blue for L4 and the footprint respectively. Error bars denote the standard deviation of replicate samples. A GAM fit is shown as a blue line, with RMSE shaded grey.

There are obvious limitations here, with no observations yet recorded for the autumn period and few, uncertain points in January/February. The general reactivity of DOC to ozone is also more complex and less understood than that of iodide given its variable composition. In the following section, the 1-layer model of Fairall et al. (2007) and the revised 2-layer model of Luhar et al. (2018), described in Section 3.2.4, will be examined both with and without contribution to reactivity from DOC.

3.3.3 Importance of Chemical and Physical Parameters in the Control of Ozone Deposition

Chang et al. (2004) present the first order rate constant for loss of ozone as

$$a = \sum_i k_i C_i \tag{34}$$

Where k_i and C_i are the 2nd order rate coefficient and the concentration respectively of species *i*. In the case where only the iodide-ozone reaction is considered, this is simply [I^-] multiplied by its 2nd order rate coefficient. A few values for this rate coefficient are reported in the literature, with Magi et al. (1997) reporting a series of values displaying a temperature dependence[72]. For consistency, in this work we use the temperature dependant value of k_{I^-} from Magi et al., as was used by Luhar et al.:

$$k_{I^-} = e^{\left(\frac{-8772.2}{SST}+51.5\right)} \tag{35}$$

It is likely that DOC reactivity to ozone is a major contributor to a, comparable in magnitude to that of iodide[74]. However, as DOC is a collection of thousands of different compounds, a single rate coefficient doesn't truly exist, as it would vary depending on the composition of the DOC. Still, some estimations have been made for the sake of having a rough value to work with; Shaw and Carpenter (2013) experimentally determined a value of 2.6×10^{-7} dm³ mol^{-1} s^{-1}, which they considered to be an upper limit due to their extraction of a more reactive portion of DOC[97]. Coleman et al. (2010) empirically determined a value of 3.44×10^{-6} dm³ mol^{-1} s^{-1} based on data fitting[181], and Sarwar et al. (2016) found using a 2nd order coefficient of 4.0×10^{-6} dm³ mol^{-1} s^{-1} led to an acceptable 1st order rate coefficient with their DOC concentrations[74]. A value between the two latter values, 3.7×10^{-6} dm³ mol^{-1} s^{-1}, was used by Luhar et al. where DOC was considered, and as such the same will be used here. Again, all molar values use the molar mass of carbon, 12 g dm^{-1}.

The primary drivers of variation in ozone deposition models are the chemical reactivity (iodide and, where used, DOC concentrations), SST (via its effects of diffusivity, solubility, and the iodide-ozone rate coefficient), and friction velocity. The extent of the variation introduced by these parameters varying is displayed in Figure 3.10.

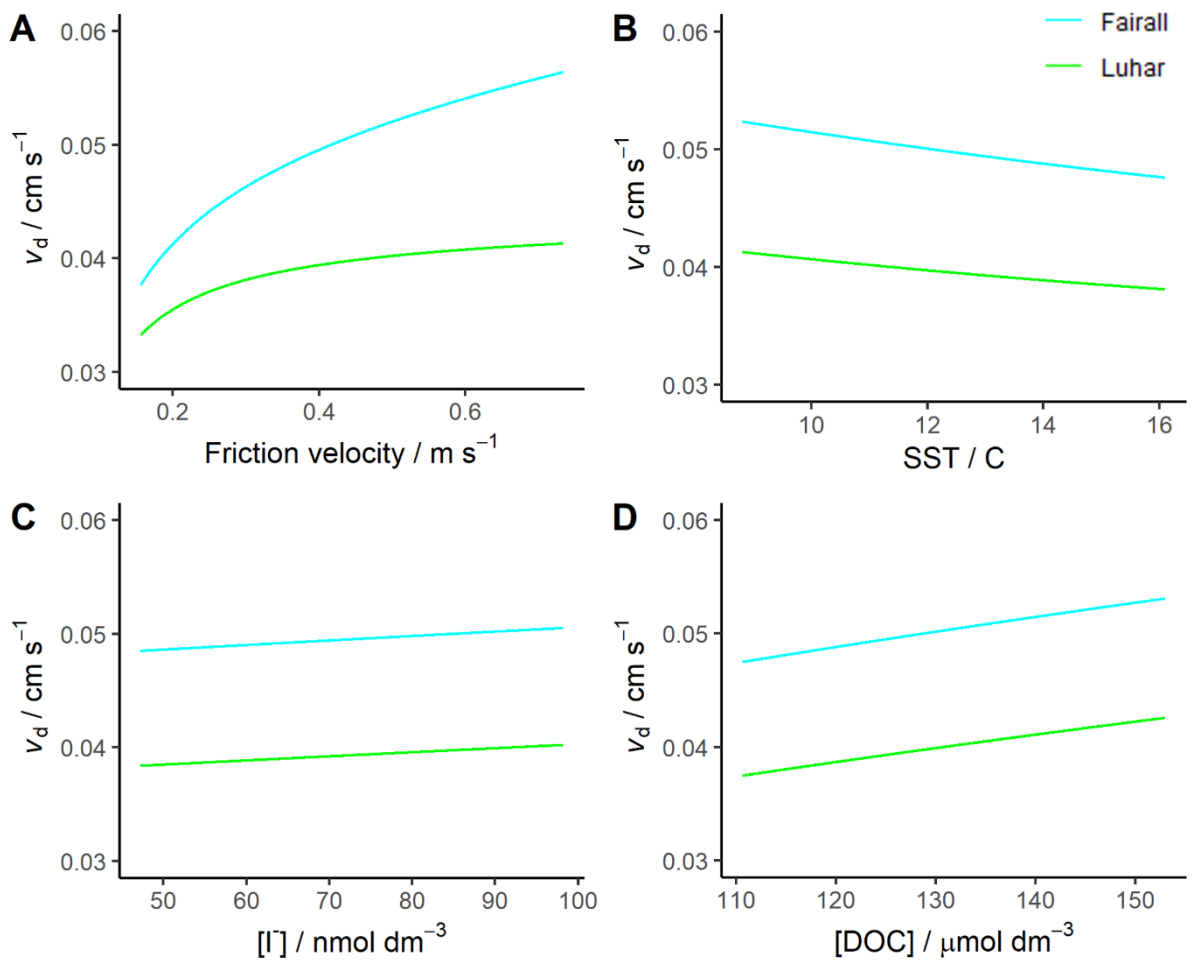

Figure 3.10: The dependencies of the 1-layer (light blue) and 2-layer (light green) models on friction velocity (A), SST (B), iodide (C), and DOC (D). In each case, all model inputs besides the one being varied were fixed at the mean of the values determined for all accepted flux measurements across all deployments. These were $u_* = 0.40$ m s^{-1}, SST = 12.6 °C, [I$^-$] = 76.5 nmol dm^{-3}, and [DOC] = 126.3 µmol dm^{-3}. Varied inputs are presented from their respective 10th – 90th percentiles across all deployments.

An obvious difference between the two model approaches is the considerably higher values generated by the 1-layer model. Luhar et al. found this model to overestimate deposition considerably, especially in cooler waters (like those around the PPAO). This is unsurprising because the reaction-diffusion sublayer in the 2-layer model effectively slows the vertical movement on ozone in the very surface layer due to the absence of any contribution from turbulence. It is also apparent that, for the chosen DOC-ozone rate constant value, DOC plays a substantial role that is even greater than that of iodide. This can be seen from the variation of v_d across the observed DOC concentrations in Figure 3.10D being greater than that caused by observed iodide variations (Figure 3.10C). It is likely due to the considerable variation and high levels of DOC seen at the sample site due to its coastal location. It is interesting to observe the negative correlation between v_d and SST, when Luhar et al. found SST to be one of the strongest predictors of ozone uptake globally[149]. This is probably a consequence of SST

being a strong predictor of iodide concentration globally, on a large spatial scale (such as the cruises of Helmig et al. (2012) to which Luhar et al. compared their model). As such, the model of Luhar et al. parameterised iodide from SST, where we use experimental observations. Indeed, in the samples from the PPAO, iodide concentrations increased with SST (see Figure 3.11), but were not parameterised from SST, so the effects of temperature (on solubility and diffusion) can be separated from the chemical reactivity of iodide. In Figure 3.10B, SST has been varied while iodide has been kept fixed, and measurements were made at a single fixed location. Luhar et al. observed a near-constant surface resistance at low SST when only iodide reactivity (not DOC) was considered, increasing at higher SST. This is likely due to their parameterisation of iodide using SST. In Figure 3.9, since iodide is fixed, the temperature dependence of the iodide-ozone rate constant is not sufficient alone to counteract the change in solubility. Indeed, upon inclusion of a DOC term, Luhar et al. found a negative correlation between their modelled surface resistance and SST, only beginning to trend upward around 20 °C.

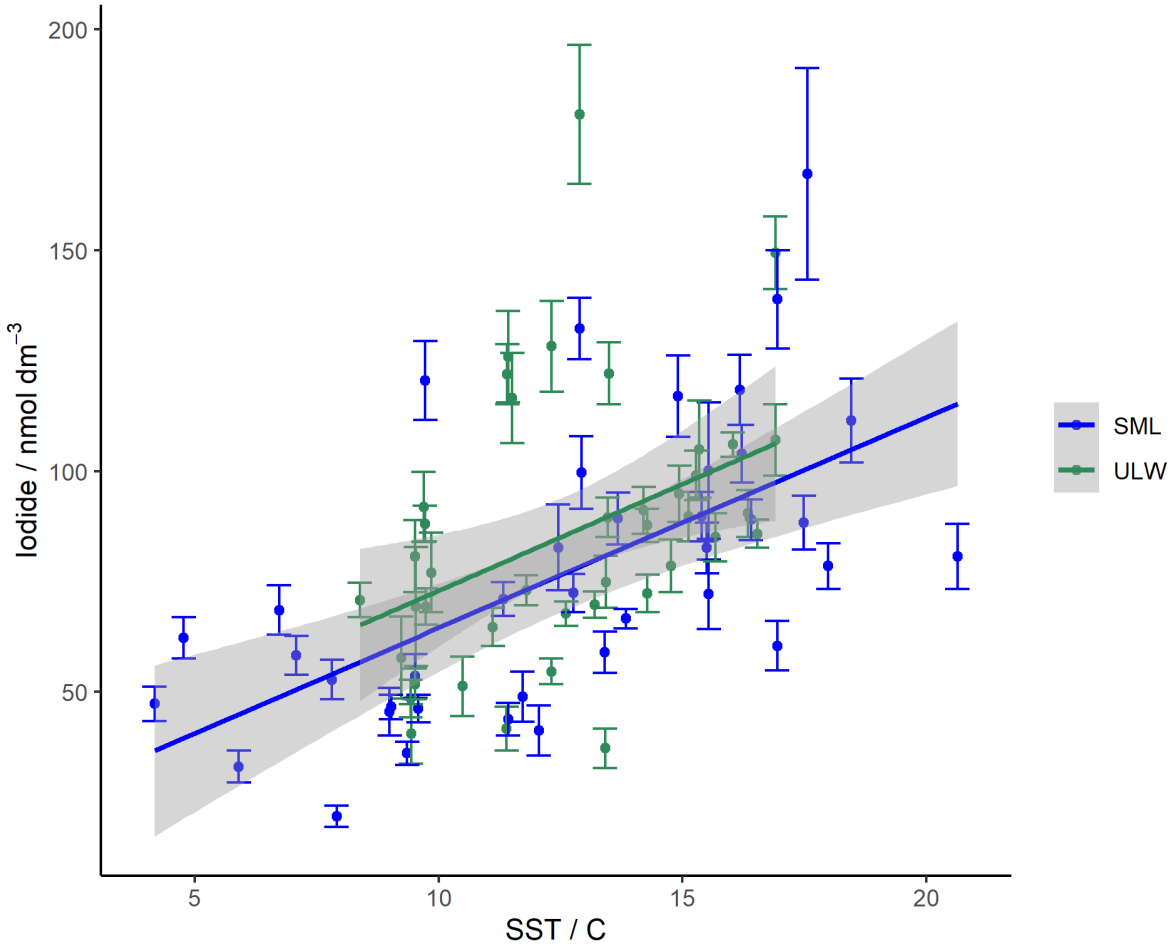

Figure 3.11: Iodide concentrations for samples measured within the flux footprint plotted against SST with linear fits. Both SML (blue) and ULW (green) samples show an increase with temperature.

The final major contributor to model variation is friction velocity, closely linked over the ocean to wind speed. There has been considerable variation in reports of the wind speed dependence of ozone

deposition; the cruises of Helmig et al. variably showed either an apparent strong dependence (TexAQS06), or the complete absence of any (STRATUS06/GasEx08)[79]. The difference in the treatment of waterside turbulence in the models is reflected here by the models not merely being offset, but having different gradients. The 2-layer model flatten rapidly, with relatively little dependence compared with the 1-layer model. The variation of measured deposition velocity with friction velocity and their relation to these models will be discussed in Section 3.4. It should also be mentioned that, while wind speed exists as in input for the modelling of R_a independently from friction velocity, the overall contribution of R_a to v_d is so small that this factor has not been addressed here.

3.3.4 Comparison of Modelled and Observed v_d

Ozone deposition velocities predicted by the 1-layer and 2-layer models were generated for each eddy covariance measurement in each deployment that passed quality criteria. Time series for each deployment are shown in Figure 3.12, each with reactivity represented by iodide alone, or by iodide together with DOC. A summary of the values for each deployment is also given in Tables 3.1 - 3.3. There is a clear difference in magnitude between the models. The 2-layer, Luhar model consistently predicts v_d values lower than the 1-layer, Fairall model. The bigger difference by far, however, is that induced by the inclusion of DOC in the determination of the reactivity term (Eq. 34).

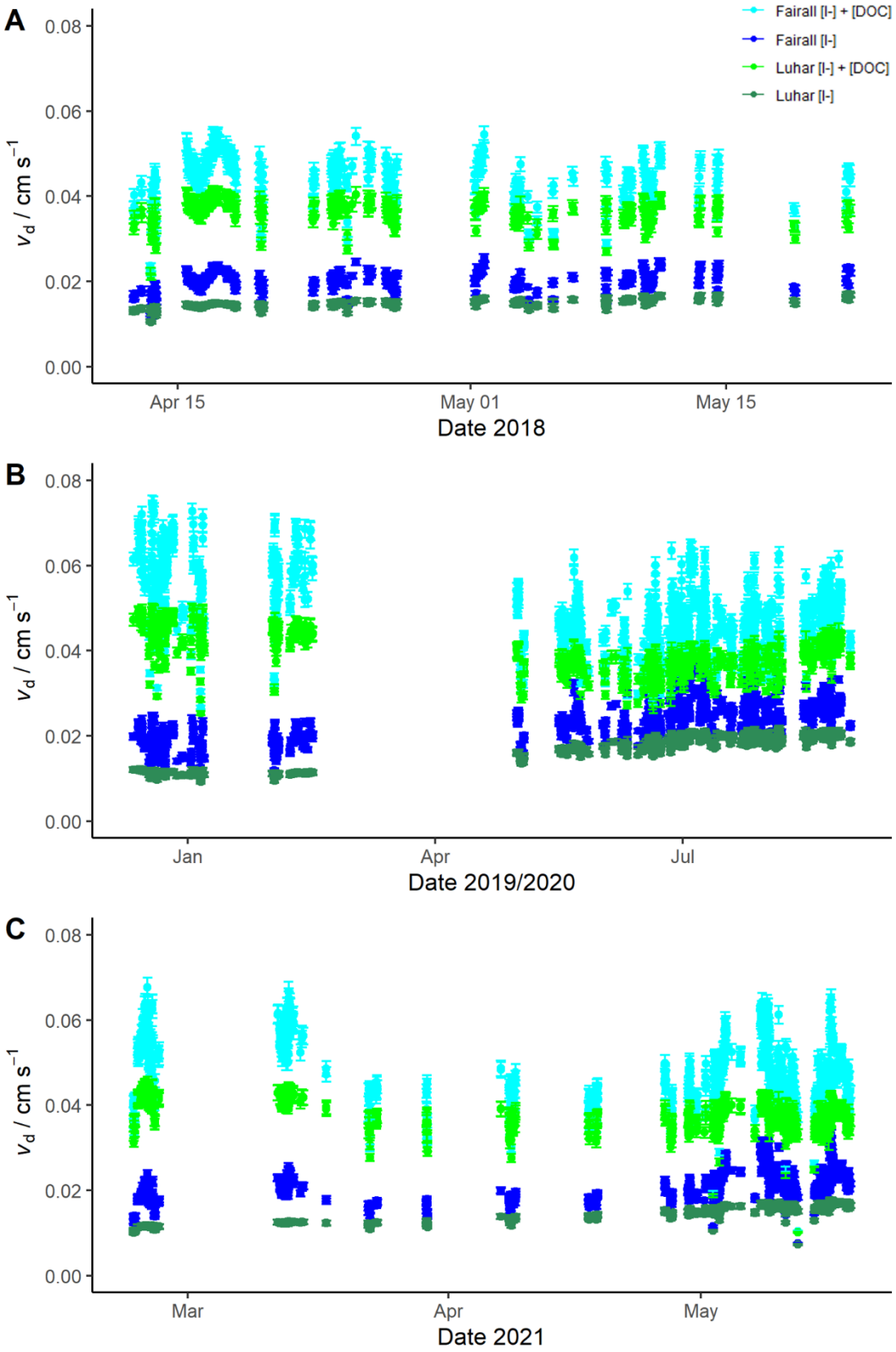

Figure 3.12: Time series of model values obtained for each experimental observation of deposition velocity across deployments 1-3 (A-C). The 1-layer model is shown in light/dark blue, including DOC reactivity and not doing so respectively. The 2-layer model is shown in light/dark green, also with and without DOC reactivity considered. Error bars on each point reflect the uncertainty introduced into the model by the RMSE of the iodide and DOC GAMs used to determine their respective concentrations (Figures 3.5 and 3.8).

Table 3.1: Summary of model values obtained for deployment 1. All values in cm s^{-1}

Model	Min	1st Quart	Median	Mean	3rd Quart	Max
Fairall [I-] + [DOC]	0.022	0.042	0.045	0.045	0.048	0.055
Fairall [I-]	0.012	0.019	0.020	0.020	0.022	0.026
Luhar [I-] + [DOC]	0.021	0.036	0.037	0.037	0.039	0.041
Luhar [I-]	0.010	0.014	0.015	0.015	0.015	0.017

Table 3.2: Summary of model values obtained for deployment 2. All values in cm s^{-1}

Model	Min	1st Quart	Median	Mean	3rd Quart	Max
Fairall [I-] + [DOC]	0.027	0.043	0.049	0.049	0.054	0.075
Fairall [I-]	0.011	0.021	0.024	0.024	0.027	0.038
Luhar [I-] + [DOC]	0.025	0.036	0.039	0.039	0.043	0.05
Luhar [I-]	0.009	0.012	0.018	0.017	0.02	0.022

Table 3.3: Summary of model values obtained for deployment 3. All values in cm s^{-1}

Model	Min	1st Quart	Median	Mean	3rd Quart	Max
Fairall [I-] + [DOC]	0.010	0.042	0.047	0.048	0.054	0.068
Fairall [I-]	0.008	0.019	0.021	0.021	0.023	0.033
Luhar [I-] + [DOC]	0.010	0.036	0.038	0.038	0.041	0.045
Luhar [I-]	0.007	0.013	0.016	0.015	0.016	0.018

It is apparent that the large scatter in the experimental observations of v_d across all deployments is far greater than the variation in the model results brought about by seasonal changes in iodide, DOC, temperature, and shorter scale variation in wind conditions. As shown in Section 2.3, a clearer picture of deposition velocity becomes apparent with binning data together in time – as a whole deployment in the case of the shorter deployment 1, or into monthly bins where the deployment continued on longer. The observations can therefore be compared to the models in the same context. Since model values have been determined for each accepted experimental observation, the model inputs such as I^- and DOC will be weighted to the relevant time period in cases where, for instance, only the start or the end of a given month is available. These comparisons are presented in the form of histograms in Figure 3.13.

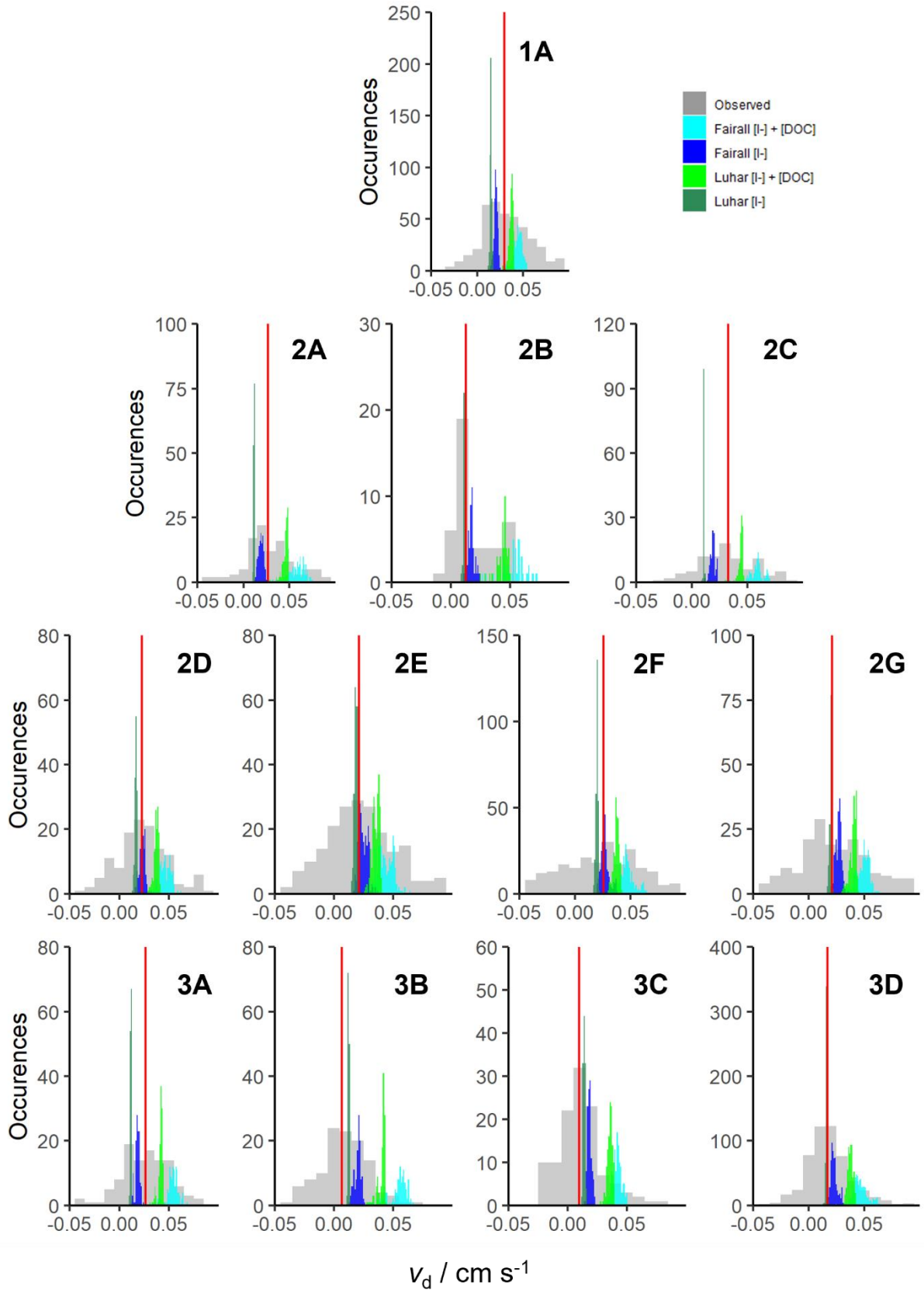

Figure 3.13: All model results displayed over the distribution of experimental values (grey). Deployment 1 is shown in 1A, deployment 2 is split into December of 2019 and January, February, May, June, July, and August of 2020 (2A-G) and deployment 3 is split into February, March, April, and May of 2021 (3A-D). The experimental median for each period is shown in red. Model data are plotted in 0.001 cm s^{-1} bins, whereas experimental values are in 0.01 cm s^{-1} bins. The y axis therefore displays one tenth on the values in a given bin for models. The x axis is also limited to -0.05 - 0.10 cm s^{-1} for clarity.

Each model has a much narrower distribution than the experimental data for reasons already discussed. The 2-layer model without DOC reactivity has an especially narrow distribution, compared to the 1-layer model for the same reactivity. The distribution of both models widens noticeably with the introduction of DOC into the reactivity term. This reflects the large variability in seasonal DOC at the site introducing greater variability on top of that already present from friction velocity, iodide and SST.

The experimentally determined medians for each period mostly lie around the distribution of the 1-layer model without DOC, with some exceptions. The median deposition velocity for deployment 1 (1A) lies beyond the iodide-only 1-layer model values, lying between them and the values obtained by the 2-layer model with DOC reactivity included. The same is true of February 2020 (2C), with those two periods showing the highest average deposition velocities observed over the course of all deployments. This is also true to a lesser extent of February 2021 during deployment 3 (3A). Conversely, March of 2021 displayed the lowest median deposition velocity, falling below even the model values of the iodide-only 2-layer model. The average median experimental and model values can be compared conveniently as a time series, shown in Figure 3.14 and summarised in Table 3.4.

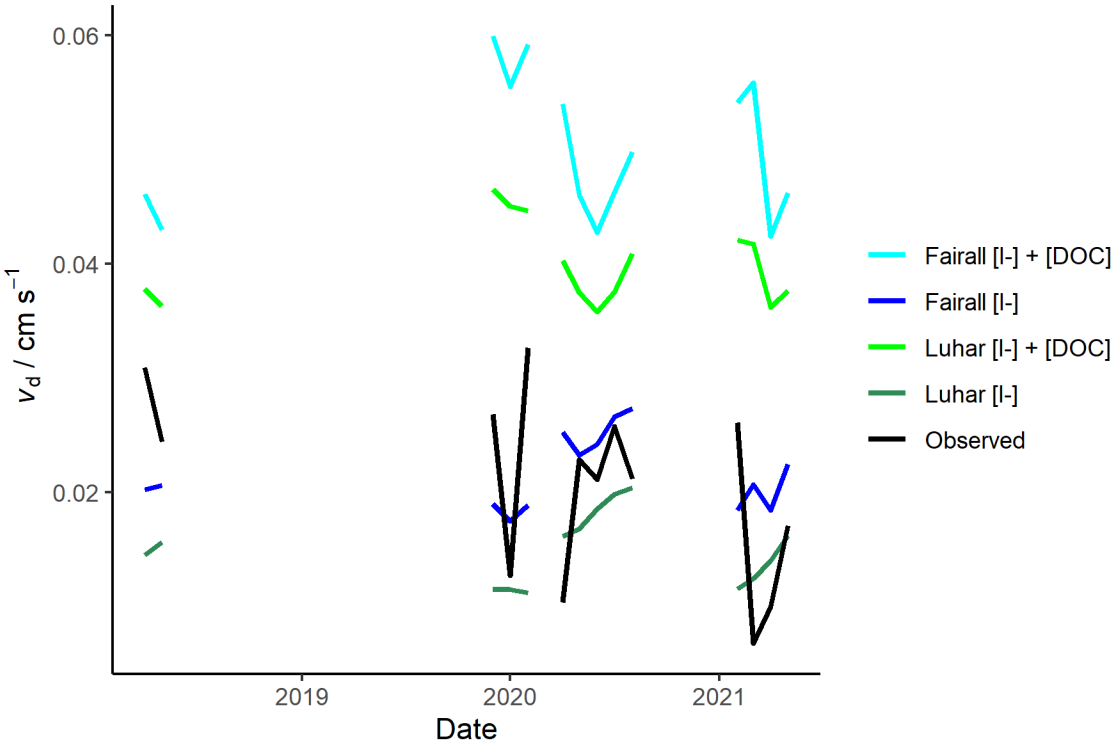

Figure 3.14: Time series of the monthly median deposition velocities obtained across all deployments experimentally (Black) and modelled by the 1-layer (blue) and 2-layer (green) models, with and without DOC reactivity (light and dark respectively).

Table 3.4: Median measured and modelled deposition velocities, by month. Deployment 1 in white, 2 shaded grey, and 3 shaded blue.

Date	Observed	Fairall [I^-]	Fairall [I^-] + [DOC]	Luhar [I^-]	Luhar [I^-] + [DOC]
Apr / 2018	0.031	0.020	0.046	0.015	0.038
May / 2018	0.024	0.021	0.043	0.016	0.036
Dec / 2019	0.027	0.019	0.060	0.012	0.046
Jan / 2020	0.013	0.017	0.055	0.011	0.045
Feb / 2020	0.033	0.019	0.059	0.011	0.045
Apr / 2020	0.010	0.025	0.054	0.016	0.040
May / 2020	0.023	0.023	0.046	0.017	0.037
Jun / 2020	0.021	0.024	0.043	0.019	0.036
Jul / 2020	0.026	0.027	0.046	0.020	0.038
Aug / 2020	0.021	0.027	0.050	0.020	0.041
Feb / 2021	0.026	0.018	0.054	0.012	0.042
Mar / 2021	0.007	0.021	0.056	0.012	0.042
Apr / 2021	0.010	0.018	0.042	0.014	0.036
May / 2021	0.017	0.022	0.046	0.016	0.038

Overall, the observations are closer in magnitude to that of either model in the absence of DOC reactivity. However, a number of elements in the structure of time series where models include DOC are interesting. Examining deployment 1 as 2 parts split by month, the deposition velocity in May is slightly below that in April. Where the models only use iodide reactivity, they predict an increase in deposition during that period. However, the inclusion of DOC, while it leads to a greatly elevated deposition velocity compared to observations, does reverse the trend to be more similar to the observations. Over the winter period of deployment 2 (Dec 2019 – Jan 2020), the observations drop in January and rise again in February, although it should be noted that January has few observations accepted compared with the other months of deployment 2. Still, this drop is predicted by the 1-layer model in both cases, with and without DOC reactivity. In contrast, the 2-layer model shows a slight decrease over the same period with no increase going into February. Given the significant difference in the way the two models respond to changes in friction velocity (see Figure 3.10A), this could be a possible cause. Indeed, the monthly median u_* values for December 2019 and February 2020 are 0.53 cm s^{-1} and 0.56 cm s^{-1} respectively, whereas the median u_* in January 2020 was only 0.37 cm s^{-1}. Lastly a sharp decline in deposition velocity is observed from February to March 2021 in deployment 3. While this isn't reflected well in any of the models, the cases where DOC reactivity is considered do predict a sharp drop, followed by a small rise – it just arrives a month later than is observed. A

limited number of observations of DOC concentrations over this period (see Figure 3.9) could mean that the apparent drop in DOC is occurring at a different time to what is predicted by the GAM.

A more quantitative assessment of the models' performance against observations can be obtained by a direct linear comparison plot. With a linear fit, a gradient closer to 1 suggests a good fit for overall magnitude of v_d predicted. Such a comparison is shown in Figure 3.15.

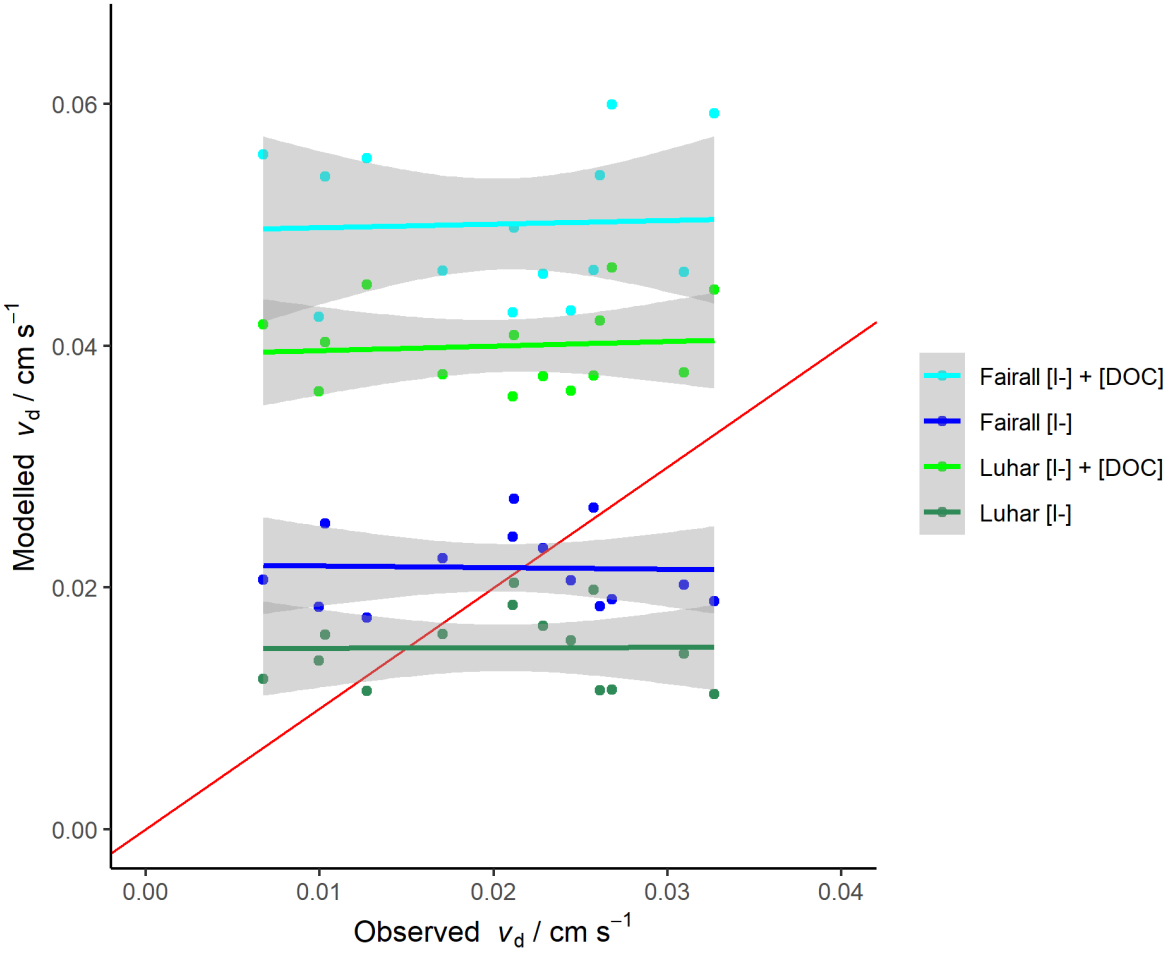

Figure 3.15: Monthly median modelled depositions velocities plotted against monthly median observations. 1:1 line shown in red. Each model is presented with a linear regression line with RMSE shaded.

Figure 3.15 shows the modelled values in the absence of DOC reactivity to lie far closer to the observations. No model has a strong gradient, and this may still be a consequence of the uncertainty of the experimental data. Still, the most positive gradients of +0.038 and +0.030 are obtained for the 2-layer and 1-layer model respectively with the reactivity of DOC considered. In the absence of DOC, the 2-layer model against observations gives a gradient of 0.003, while the 1-layer model actually has a negative gradient without DOC of -0.014. Clearly the uncertainties on these fits are huge, and the magnitude of the gradients small. While no firm answer can be drawn with certainty, these results do suggest that while the magnitude of the contribution of DOC is clearly excessive when considered as

has been done here, it could account for some of the variation not explained by iodide reactivity alone. The matter of magnitude comes about from the expression for total reactivity in Eq. 34 (Section 3.3.3). It has assumed that the two components - DOC and iodide - behave wholly independently of one another in the SML concerning their reaction with ozone. There is a good likelihood that this is not the case; Martino et al. (2012) examined the deposition of ozone to solutions of iodide and DOC, both separately and combined, and found that deposition velocity in the combined system was only 80% of that expected from the sum of the individual experiments[172]. It is also possible that the presence of DOC in the system introduces factors affecting ozone beyond chemical reactivity. Both models depend on the solubility and diffusivity of ozone in water for the calculation of R_c. Though concentrations of DOC are only of the order of ~100 μmol dm^{-3}, the hydrophobic or surfactant-like behaviour of some of its components could alter the rate of transfer of ozone into the water column.

3.4 Friction Velocity Dependence

Given the varied reports of its importance in previous measurements, the relationship between our observations and measured friction velocity will be examined in particular. Previous oceanic, ship-based ozone flux measurements reported by Helmig et al. (2012) give mixed results[79]. The variation of their deposition velocity observations with wind speed as presented in their publication is shown in Figure 3.16.

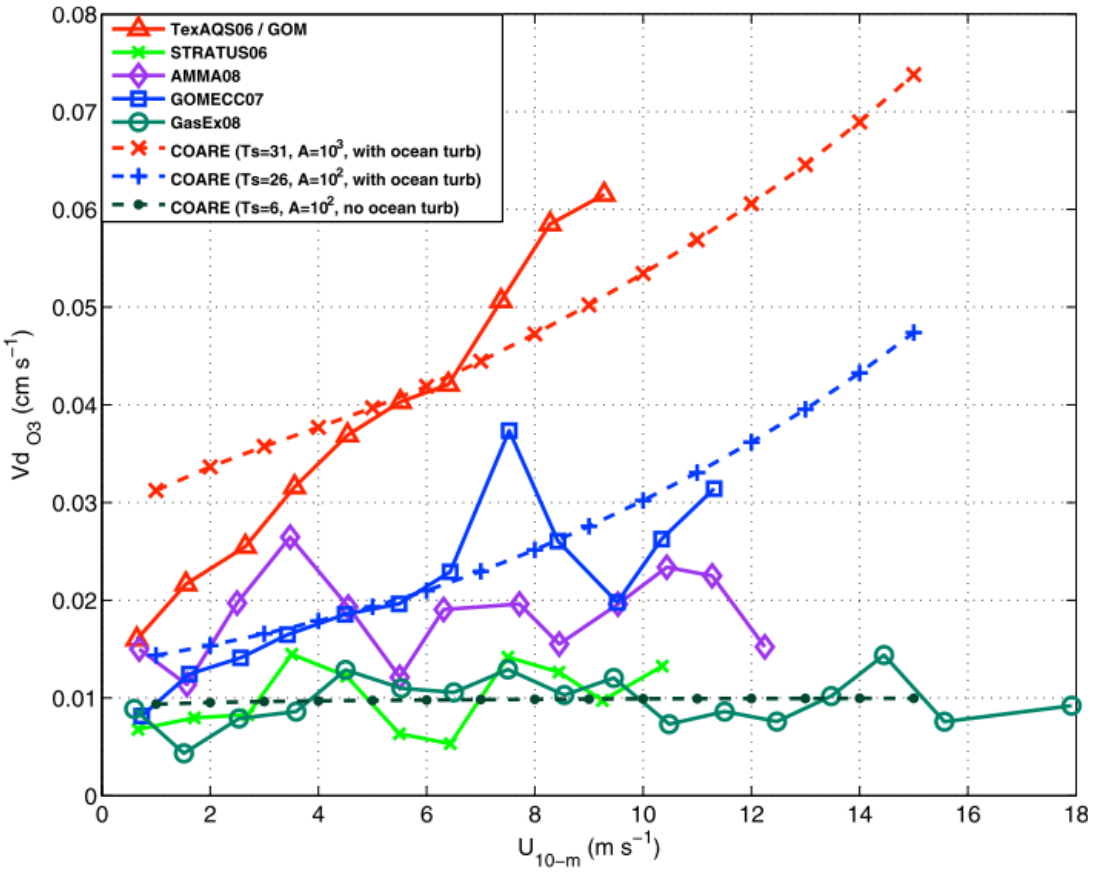

Figure 3.16: Ozone deposition velocity results varying with 10 m wind speed as presented in Helmig et al. (2012). Dashed lines represent model values obtained from the COARE algorithm with varying chemical reactivity (A). Where ocean turbulence is included, this represents the 1-layer model. Where it is omitted, it equates to the determination of surface resistance by Garland et al. (1980).

The TexAQS06 / GOM cruise, in the north-western Gulf of Mexico, showed the strongest dependency, with observations during GOMECC07 (Gulf of Mexico and USA east coast) also demonstrating some correlation. The authors found this trend could be reasonably matched using the 1-layer model, with a reactivity value chosen to adjust the magnitude of the model output to a similar level to observations. In contrast, the other cruises displayed little to no variation in deposition velocity with wind speed. In this case, the lack of trend was better represented by a model with no oceanic turbulence considered – the expression from Garland et al. (1980) (Eq. 24).

It is worth commenting that the results in Figure 3.16 are presented against 10 m wind speed, which the authors note varies approximately linearly with friction velocity over the ocean. The relationship between these two variables observed at the PPAO is shown in Figure 3.17.

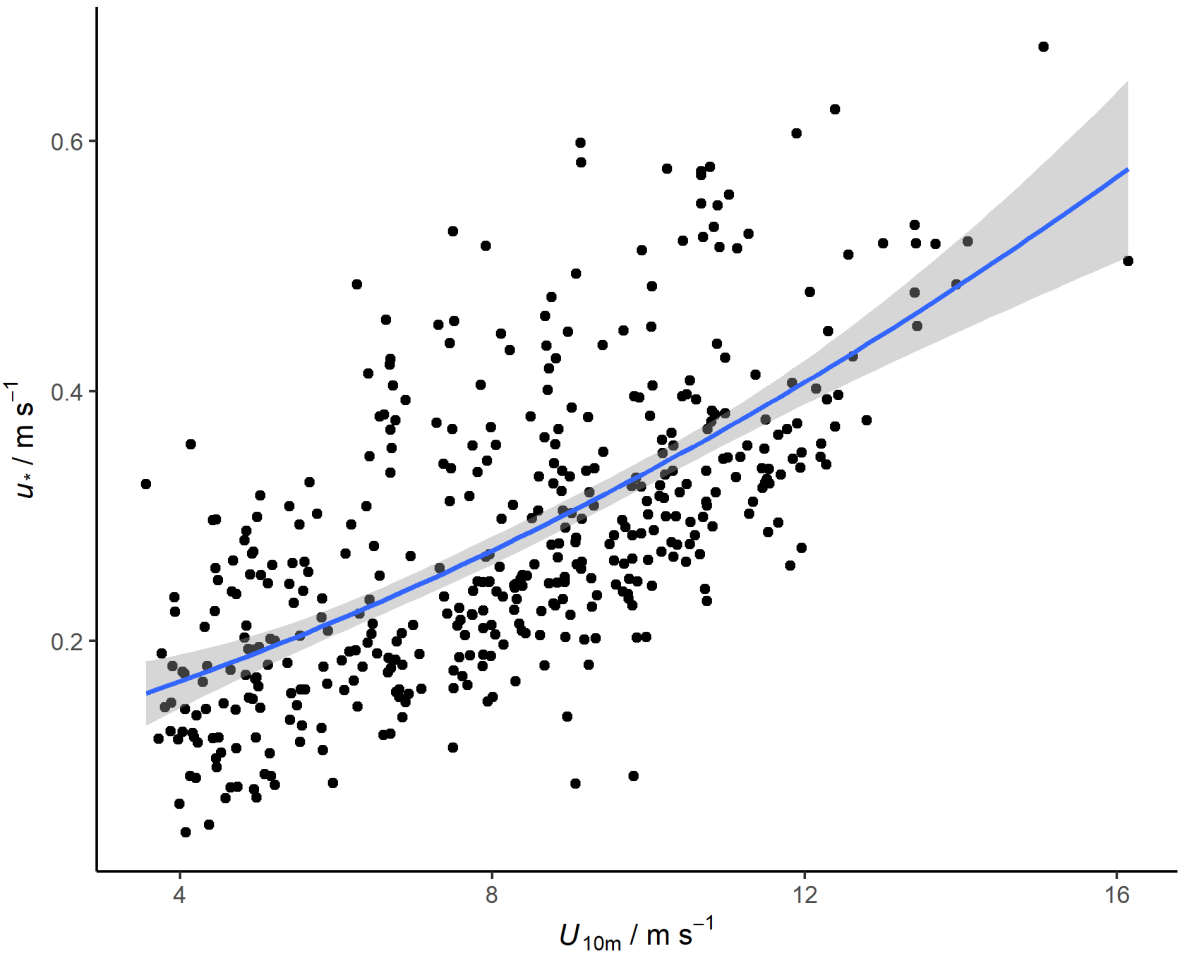

Figure 3.17: Variation of friction velocity with 10 m neutral wind speed for deployment 1. Results are presented with a 2nd order polynomial fit, though the correlation is near-linear.

Given this relationship, values for friction velocity can be fairly reliably predicted from simple wind speed data for use in models. However, since high frequency wind data makes experimental determination of u_* possible, this is what has been used to generate model values in this work. Therefore, variation of v_d will be considered with respect to friction velocity, though the approach is very similar to previous work using wind speed.

Figure 3.18 shows the observed deposition velocities, unadjusted for land influence, presented as medians with interquartile ranges within friction velocity bins. Figure 3.19 shows the deposition velocities adjusted for land – both are presented due to the particular effect of lowering v_d at low u_* caused by the adjustment for land influence. In both cases, the 1-layer and 2-layer models (green and blue lines respectively) are shown with iodide only, as DOC greatly raises the predicted values. The model values were obtained using the mean [I^-] and SST for each period.

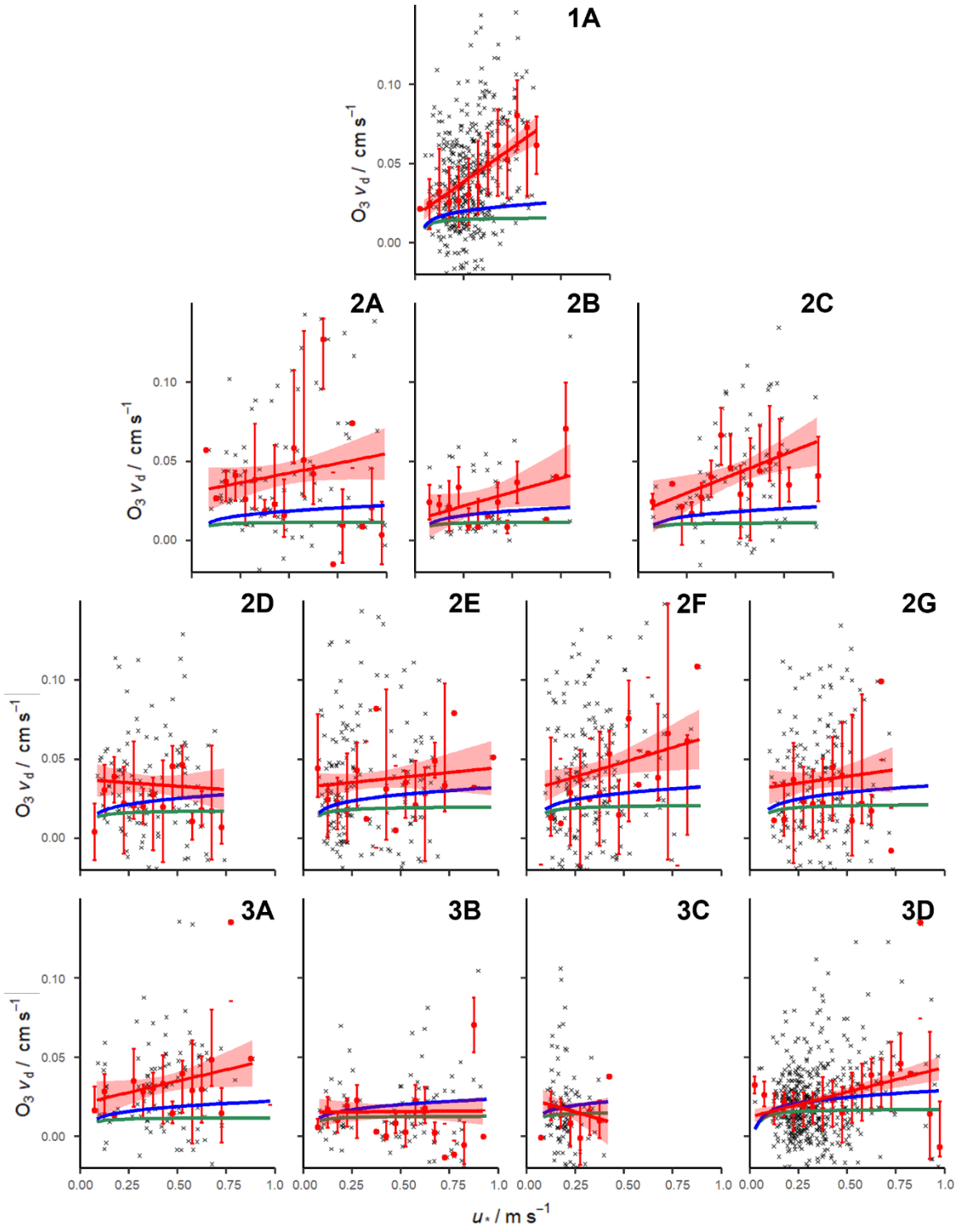

Figure 3.18: Deposition velocities, unadjusted for land influence, varying with friction velocity during each deployment. Deployment 1 is shown in 1A, deployment 2 is split into December of 2019 and January, February, May, June, July, and August of 2020 (2A-G) and deployment 3 is split into February, March, April, and May of 2021 (3A-D). Individual averaging periods are shown by grey crosses, with medians and interquartile ranges for each 0.05 m s^{-1} bin in red. A linear fit to the experimental data (individual points, not the binned medians) is shown in red. The 1- and 2-layer models are also shown (blue and green respectively) using the average $[I^-]$ and SST for the time period.

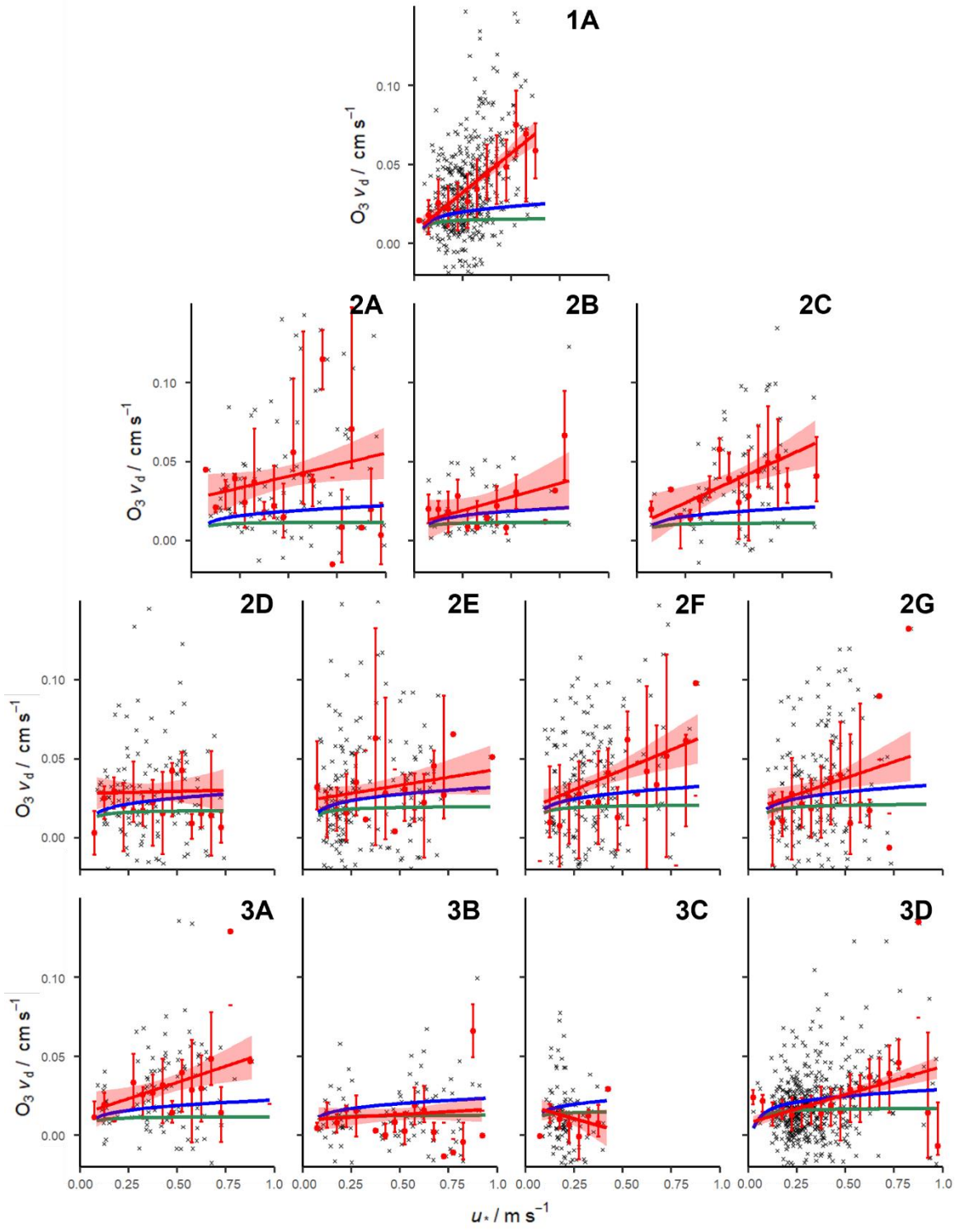

Figure 3.19: Deposition velocities, adjusted for land influence, varying with friction velocity during each deployment. Deployment 1 is shown in 1A, deployment 2 is split into December of 2019 and January, February, May, June, July, and August of 2020 (2A-G) and deployment 3 is split into February, March, April, and May of 2021 (3A-D). Individual averaging periods are shown by grey crosses, with medians and interquartile ranges for each 0.05 m s^{-1} bin in red. A linear fit to the experimental data (individual points, not the binned medians) is shown in red. The 1- and 2-layer models are also shown (blue and green respectively) using the average $[I^-]$ and SST for the time period.

Even when data are unadjusted for land influence (Figure 3.18), a positive correlation between deposition velocity and friction velocity is observed in almost all periods; the exceptions being May 2020 (2D), and March/April 2021 (3B/C). The negative gradient in May 2020 is flattened when land influence is adjusted for (Figure 3.19), showing little or no dependence on friction velocity, similar to March 2021. April 2021 is the only period where a negative gradient is sustained even when the effects of land within the flux footprint are accounted for. However, this is likely a consequence of the scarcity of data in that period, and a lack of range in observed u_* - never exceeding 0.45 m s^{-1}.

Since the footprint extent, and thus the land within it, depends greatly on wind speed/friction velocity, the effect of adjusting for land in Figure 3.19 is that the v_d values at the lowest friction velocities are reduced the most, with higher values largely unaffected. This tends to bring observations more in line with the models at low u_*, where the two models themselves converge. This is most apparent in deployment 1 (1A), and June – August 2020 (2E-G), where median deposition velocities are brought close to the models where $u_* < 0.25$ m s^{-1}.

While a positive correlation is most common, the extent and certainty of that dependence varies greatly. Deployment 1 (1A) and May 2021 (3D) offer the clearest dependencies, and it is noteworthy that these periods have considerably more accepted data than other periods. Even these two periods differ significantly, however. The v_d values and dependence on u_* in May 2021 are reasonably well represented by the 1-layer model; the observations during deployment 1 though show a vastly greater dependence than either model predicts. Regardless of whether it matches closely in magnitude or gradient, the 1-layer model at least displays some dependence on friction velocity that could reasonably fit with our observations. The 2-layer model however shows so little variation with u_* that it is hard to reconcile this element of it with the majority of these observations.

3.5 Conclusions

Iodide concentrations in the seawater around the PPAO show an annual cycle, increasing over the summer coinciding with phytoplankton blooms around the site. While no particular difference is observed between samples collected within the flux footprint and those collected at the L4 site ~8 km south, concentrations within the microlayer were consistently slightly lower than those in the underlying water. It is possible that this is a consequence of iodide in the SML reacting with ozone in the air.

Conversely to the iodide measurements, DOC concentrations were lower during the summer than the winter. This is perhaps surprising given the increase in biological activity during this period. One possibility is that a larger fraction of the TOC was present in particulate form. As no measurements of

TOC exist for these samples (due to the necessity to filter them to freeze for other analyses), this hypothesis cannot be tested here.

A consequence of these opposing seasonal cycles is that in terms of predicted chemical reactivity, these two components somewhat cancel each other out. This at least goes some way to explaining why no great increase in ozone deposition is observed during the summer months compared with winter.

The two models compared with the observations differ in their treatment of waterside turbulence in the calculation of surface resistance, R_c. Generally, both models primarily depend on SST, chemical reactivity, and friction velocity, with the 2-layer model of Luhar et al. (2018) giving consistently lower values than the 1-layer model of Fairall et al. (2007). Both models yielded considerably greater deposition velocity values when DOC was included in the reactivity term, approximately doubling. The majority of experimental observations lay somewhere around the values obtained by the 1-layer model in the absence of DOC, though some periods were closer to the 2-layer model with or without DOC (higher or lower respectively). The inclusion of DOC in the chemical reactivity term remains prone to huge uncertainty given the complex composition of DOC and the limited efficacy of attributing a single rate constant to a collection of compounds. It is possible that the reactions of iodide and DOC partially inhibit each other, resulting in a lower overall reaction rate than would be expected from each in isolation. DOC especially could present more considerations due to physical effects; both models use the solubility and diffusivity of ozone in water. While the overall concentrations of DOC are fairly low, the potential formation of slicks and the variation of surface tension due to surfactant constituents give rise to a number of other factors to be examined.

Lastly, a dependence of observed deposition velocity on friction velocity was observed during a number of periods. In contrast, the 1-layer model predicted a generally more modest correlation, while the 2-layer model displayed almost no dependence on friction velocity much above $u_* = 0.2$ m s^{-1}. Though the 2-layer model has been compared to past observations with some success[149,173], observations presented here suggest that the role of turbulence is not necessarily well reflected in the parameterisation.

4. Molecular Composition of the Water Around the PPAO

4.1 Introduction

As noted in chapter 3, dissolved organic carbon in the SML could be a crucial component in accurately parameterising oceanic ozone deposition. Its inclusion in models however is challenging (compared with iodide) due to its complex and variable composition making the application of a single rate constant a major oversimplification. This chapter presents analysis of the composition of dissolved organic material (DOM) in the SML around the PPAO flux site (sample locations in Figure 3.1) using liquid chromatography mass spectrometry (LCMS) and a non-targeted analysis to identify compounds present. An operationally defined fraction of the DOM is isolated and concentrated via solid phase extraction (SPE), hence the term SPE-DOM. Analysis using high resolution LCMS then allows for hundreds of compounds to be resolved and assigned formulae based on molecular mass. 'Bulk' metrics for various samples can then be examined, such as average double bond equivalence (DBE), or specific compounds of interest examined in particular details to gain greater insight into the variation in DOC composition that could affect ozone deposition.

Unsaturated fatty acids (FAs) are known to react with ozone. A number of fatty acids have been identified in seawater[182], and present good options to observe in our samples. Saturated FAs are not expected to be reactive due to the lack of carbon-carbon double bonds, whereas unsaturated FAs are more likely to react. FAs are often hard to detect by LCMS, and are commonly esterified for identification as fatty acid methyl esters (FAMEs) by GCMS.

The work presented in this chapter aims to identify changes in organic composition upon ozonolysis by examining bulk metrics such as DBE before and after exposure to high levels of ozone. Specific FAs and their products upon ozonolysis are also examined in detail to identify compounds being formed and lost. Metrics and compounds that show clear change in these experiments are then scrutinised in the samples from the PPAO to identify any seasonal changes in composition.

4.2 Methodology

4.2.1 Overview

The collection of SML samples around the PPAO was discussed in Section 3.2.1, and the samples used for the analyses presented here were collected in the same fashion; material was drawn up using a Garrett screen, filtered, and frozen for delivery to the labs in York. The only notable difference between these samples and those for DOC and iodide concentrations is the volume involved. Where 10-100 mL was sufficient for DOC and iodide concentrations, 2 L of SML were used per sample for SPE-DOM. This large volume was used in an effort to extract a sufficiently concentrated sample of

DOM for clear detection of individual compounds via liquid chromatography mass spectrometry (LCMS).

4.2.2 Sample Preparation

Samples were prepared according to the method of Koch & Dittmar (2006)[183], with each 2 L sample of water first being acidified to pH 2 using a small amount (~1 mL) of 12 mol dm^{-3} HCl (Fisher Analytical Reagent Grade). SPE cartridges (Bond Elut PPL, 500 mg sorbent, Agilent) were then prepared for each sample, rinsing through three times with Optima™ LCMS grade methanol (Fisher Chemical) without allowing cartridges to fully run dry. The setup for this consisted of a sealed glass manifold under vacuum with taps on top. Cartridges were connected to these taps, allowing for the adjustment of the suction on each to achieve a steady, slow flow through each. Waste methanol and water was then collected in a large trap before the pump to prevent liquid from damaging it. Once samples had been acidified and the cartridges prepared, siphons were set up between the cartridges and each sample bottle such that a steady flow of acidified water was drawn through each cartridge, accumulating the DOM within each. The siphon system was necessary due to the very small (~5 mL) volume of each cartridge making manual refilling excessively awkward and time-consuming. Every effort was made to maintain similar flow rates across all samples over the course of each extraction, which typically lasted 5-6 hours per batch. This corresponds to a typical flow rate of ~6 mL min^{-1} through each cartridge. After all 2 L of each sample has passed through a cartridge, each one was then rinsed through three times with 0.01 mol dm^{-3} HCl (in Optima™ water) and subsequently allowed to dry by fully opening each tap to the vacuum beneath.

At this point, each SPE cartridge contained the accumulated SPE-DOM from the sample passed through it, ready to be extracted and stored for subsequent analysis. Sample vials were placed on a shelf within the vacuum chamber under each tap, having previously been heated in a furnace (450 °C for 5+ hours) to remove any pre-existing organic compounds. The DOM from each cartridge was then eluted dropwise into these vials with 8 mL of Optima™ LCMS grade methanol. Due to the size constraints of the setup (8-10 samples at once) and the convenience of analysing as many at once on the LCMS, these samples were stored in a freezer at -20 °C, ready for redissolution once a good number of samples were prepared. Between extractions, all parts in contact with sample water were washed with milli-Q water before and after soaking in 0.65 mol dm^{-3} HCl.

Finally, once a collection of samples was ready for analysis, each was evaporated to dryness under vacuum using a miVac Quattro modular concentrator (part no. 04-5057, Genevac SP Scientific) before being re-dissolved in 1.5 mL of 5% acetonitrile in water (both Optima grade). A series of these re-dissolved samples were then analysed.

4.2.3 Orbitrap LCMS

Samples were analysed by reverse phase ultrahigh performance liquid chromatography (UHPLC) using negative mode high resolution electrospray ionisation mass spectrometry (HR-ESI-MS), though the whole process is more conveniently abbreviated to LCMS. Such methods have commonly been used in compositional analysis of complex organic mixtures[184–188]. The chromatography used a Dionex UltiMate 3000 (Thermo Scientific), consisting of an RS pump, RS autosampler and RS column compartment. Samples (50 µL injection volume) were run through a Accucore aQ column at 50 °C for 28 minutes, with a mobile phase of acetonitrile and water, both Optima LCMS grade with 0.1% formic acid as a modifier to improve ionisation. The total mobile phase flow was 300 µL min^{-1}, with the percentage of acetonitrile used starting at 5% for the first 2 minutes, before increasing over time according to the values in Table 4.1.

Table 4.1: Variation of acetonitrile present in the mobile phase. Concentration was ramped linearly between set points.

Time / minutes	Acetonitrile / %
0	5
2	5
11	35
20	95
26	95
26.5	5
28	5

The percentage of acetonitrile peaked at 95% at the 20-minute mark, at which point the analysis of sample was considered finished. The column was then flushed through with 95% acetonitrile to wash any remaining sample out of the column, before being further flushed with 5% acetonitrile to reset the column to starting conditions ready for the next sample to be run. This variable mobile phase was used to suitably separate compounds whilst maintaining a feasible analysis time. Since acetonitrile is less polar than water, the initial 5% solvent is the most polar. Some more polar compounds can readily reach the detector in these conditions, but less polar molecules would take an incredibly long time to elute, strongly preferring the non-polar, stationary phase. Increasing the acetonitrile content of the mobile phase therefore allows for these less polar compounds to be eluted at a reasonable time while still achieving good separation.

Mass spectrometric detection used a Q-Exactive Orbitrap (ThermoFisher Scientific) with a HESI-II probe ion source. A mass calibration was performed before each batch of samples was run (unless

multiple small batches were run on the same day), using Pierce ESI negative ion calibration solution (Thermo Scientific). The scan range was 85 – 1000 *m/z*.

4.2.4 Data processing

Initial processing of the LCMS outputs was handled by Dr Rosie Chance, a postdoctoral researcher in the Carpenter research group, using the software MZmine 2[189], based on the approaches of Pluskal et al. (2012)[189] and Verkh et al. (2018)[190]. Each feature with a given *m/z* value was assigned a selection of formula based on closeness of mass fit to the observed *m/z*, with the following upper limits on elements: C ≤ 100, H ≤ 100, O ≤ 50, N ≤ 5, S ≤ 3, Cl ≤ 1, I ≤ 1, P = 0, Na = 0. Many of these features identified by MS will not represent individual analytes though, and as such need excluding from formula assignment to avoid identifying compounds which are not truly present. Based on relative size and *m/z* value, peaks assigned to different atomic isotopes of the same compound were removed (e.g. a smaller peak 1 *m/z* up for a carbon-13 containing compound). A similar approach is taken to remove adducts – ions with one or more atoms added compared with a simple deprotonation. The adducts considered and removed were as follows: $[M\text{-}2H+Na]^-$, $[M\text{-}H_2O\text{-}H]^-$, $[M\text{-}2H_2O\text{-}H]^-$, $[M\text{-}2H+K]^-$, $[M+Cl]^-$, $[M\text{-}H+HAc]^-$, $[M\text{-}H_2O\text{-}H]^-$, $[M+Br]^-$, $[M\text{-}H+FA]^-$, $[M\text{-}H+TFA]^-$, $[M+NO_3]^-$. Clusters, where multiples of the analyte group together to form a single, larger ion, were similarly removed. Additionally, any features that failed to be assigned a formula were removed, and retention time (RT) was limited between 2.5 and 17.5 minutes. Lastly the number recorded points which make up the peak in each chromatogram was set to require at least 8 points to remove small, poorly defined features.

Subsequently, these data were refined by restricting assigned formulae to a set of chemically plausible boundaries. These limited the amount of non-carbon atoms permitted per structure, according to the following bounds: H/C < 2.25, O/C < 1, N/C < 0.5, S/C < 0.2. These are slightly more restrictive in allowing heteroatoms than the approach on which this method was based, as the original parameters were selected for the observation of wastewater[190]. A threshold related to the peak area and height was also used, area/height > 30, to prevent erroneous assignment of formulae to 'square peak' artifacts arising from the MZmine processing[190]. Of the formulae assigned for each peak in MZmine, the one with the closest *m/z* formula mass match was chosen that fulfilled the atomic ratio criteria. This resulted in a list of formulae and RTs for each identified peak, for which individual values could be calculated for atomic ratios (H/C, N/C and O/C), double bond equivalence (DBE) and aromaticity index, AI. DBE was calculated according to the formula

$$DBE = \frac{2C+N-H-I-Cl+2}{2} \quad (36)$$

where *C*, *N*, *H*, *I* and *Cl* are the number of carbon, nitrogen, hydrogen, iodine, and chlorine atoms, respectively, in the assigned formula.

The aromaticity index can be used to indicate the presence of aromatic systems within a compound. This is of interest in relation to ozone-organic reactivity due to the recorded reactivity of ozone with activated aromatic rings, such as phenols[191]. In simple hydrocarbons lacking heteroatoms, AI can be defined simply as DBE divided by the carbon atoms present:

$$AI = \frac{DBE}{C} \tag{37}$$

In this case, an AI of > 0.5 indicates the presence of an aromatic system, and AI > 0.67 indicates a condensed aromatic (CA) compound, in which the aromatic system spans the whole molecule. These boundaries break down in the presence of heteroatoms, however. This is because of the possibility of heteroatoms forming either single or double bonds with carbon atoms. As such, a number of other formulations of AI have been proposed to account for these effects. Koch and Dittmar (2006)[183] proposed the following formula:

$$AI = \frac{1+C-O-S-0.5H}{C-O-S-N-P} \tag{38}$$

This can be expanded for our applications to include halogens (which behave like hydrogen) and remove the *P* term (as it is not included in the formula assignment at present):

$$AI = \frac{1+C-O-S-0.5H-0.5I-0.5Cl}{C-O-S-N} \tag{39}$$

While Eq. 38/39 was intended to apply the same thresholds of 0.5 and 0.67 for aromatics and CAs respectively, Melendez-Perez et al. (2016) found the formulation to be overly generous in assigning aromaticity with certain cyclic carbonyl compounds[192]. They therefore proposed a more stringent parameter, rAI, which can again be adapted to include halogens and ignore phosphorous:

$$rAI = \frac{1+C-O-S-0.5N-0.5H-0.5I-0.5Cl}{C} \tag{40}$$

Eq. 40 presents the most stringent threshold for assigning aromaticity discussed here, though it has been noted that many genuine CAs may fail to be assigned as such by rAI due to oxygen commonly forming both single bonds (such as in alcohols, acids, and ethers) and double bonds (such as ketones and aldehydes). Koch and Dittmar (2006) therefore proposed an alteration to the oxygen term, also applied by Melendez-Perez et al. (2016), to provide a slightly more lenient assignment of aromaticity, rAI_{mod}:

$$rAI_{mod} = \frac{1+C-0.5O-S-0.5N-0.5H-0.5I-0.5Cl}{C} \tag{41}$$

Overall, this gives three different metrics for aromaticity. AI (Eq. 39) is the least stringent, potentially being overgenerous in assignment of aromaticity. rAI is the most stringent, providing the surest assignment of a condensed aromatic system at the cost of excluding many cases where it is ambiguous. Lastly, rAI_{mod} can be considered a compromise; it is less strict than rAI, with values >0.67 representing a good likelihood of the compound being a CA.

With all of these metrics, the goal is to be able to compare the values between samples. Since the compounds present in samples are likely to be numerous and variable, it makes sense to try to formulate a single value (of e.g. DBE, H/C etc) for each sample. This presents some issues due to the semi-quantitative nature of these analyses. Sensitivity for a given compound in several samples run together is likely to vary little, giving rise to the possibility of observing changes in concentration over time via observation of peak area. However, peak areas of different compounds are not comparable, as different analytes could behave very differently. For instance, a compound more readily retained during SPE, or more soluble in the LC solvent would have a higher response than one with lower retention/solubility. Additionally, the efficiency with which a given molecule is ionised in the ESI MS source could influence detection. Therefore, while average parameters are calculated weighted by peak area, these are expected to be dominated by a small number of compounds with greatest response. Since these are frequently sulfate-type molecules, weighted averages are also presented with sulfur-containing species omitted. Lastly, parameters are also calculated as simple means and medians, with all accepted formula assignments weighted equally.

4.3 Blank Tests

Given the very low concentrations of individual compounds, it is important to have some idea of what compounds may be introduced into the sample by the extraction and analysis processes. For example, lengths of plastic tubing the SPE cartridges could leach tiny amounts of organics into the samples. As such, blanks were run: a solvent blank which involved only the processing of pure solvent on the LCMS, and a SPE blank, where the SPE procedure was conducted (conditioning cartridges, eluting with methanol etc.) prior to LCMS analysis. A summary of these runs is given in Table 4.2.

Table 4.2: Features present in a solvent and an SPE blank processed by LCMS.

Metric	Solvent Blank	SPE blank
Total features	22	26
Unique formulae	21	15
Formulae only in this blank	9	3

Firstly, the number of compounds observed is, as expected, small compared with the hundreds or thousands seen in seawater samples. There are, however, differences between the two blanks, and not simply in the form of additional compounds introduced by the SPE process. Interestingly, the SPE blank contained several peaks assigned the formula $C_6H_{10}ClI$ that were not present in the solvent blanks. This is why there are only 15 unique formulae in the SPE blank, but 26 features identified. Many of the peaks seen in the solvent blank but not in the SPE blank were long chain sulfates; most of the biggest peaks present in both blanks were sulfates too.

A van Krevelen plot can be used to visualise the compounds present in these analyses, as shown in Figures 4.1 and 4.2. Van Krevelen plots visualise non-targeted organic composition data by the plotting the ratios of hydrogen and oxygen atoms to carbon. Different chemical species typically reside within certain areas of the plot: aromatics occur at the bottom, towards the left; fatty acids occupy the upper left region; carbohydrates exist in the upper right (beyond the bounds of the x axis in Figures 4.1 and 4.2). Dicarboxylic acids, discussed later in this chapter, occupy the region between 1.5 and 2 H/C, and span the range of the x axis depending on the hydrocarbon chain length. Moving directly up the y-axis represents the presence of more and more hydrogen atoms (hydrogenation) without the addition of any oxygen. As such, more saturated compounds occur higher on the y axis, and a greater degree of unsaturation lowers the H/C ratio. Similarly, moving along the x-axis represents changing numbers of oxygen atoms (oxidation/reduction) with a constant hydrogen/carbon ratio. For instance, small compounds with multiple carbonyl groups occur far along the x-axis. Several straight lines of compounds are observed where the compounds present vary by the presence of a simple chemical unit (such as $-CH_2-$ in a long carbon chain), known as homologous series. This can be more clearly seen in diagrams with greater numbers of compounds such as Figures 4.6 and 4.7. In the example of $-CH_2-$ units, this produces lines that converge on a H/C ratio of 2 and an O/C ratio of 0. Similarly, alkene units (-CH-) result in lines converging at a H/C ratio of 1 and an O/C ration of 0.

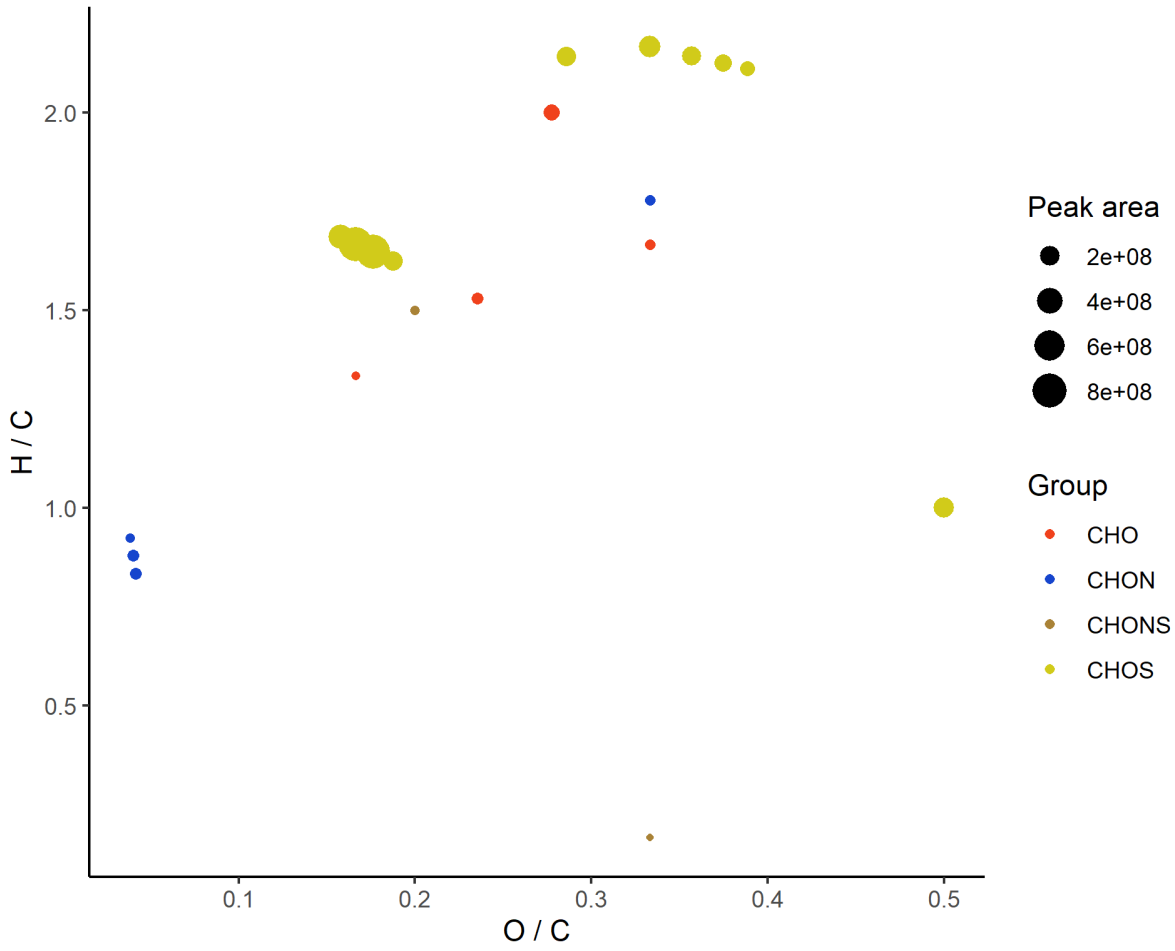

Figure 4.1: Van Krevelen plot for a solvent blank run on the LCMS. Most of the largest peaks are sulfates – surfactant molecules.

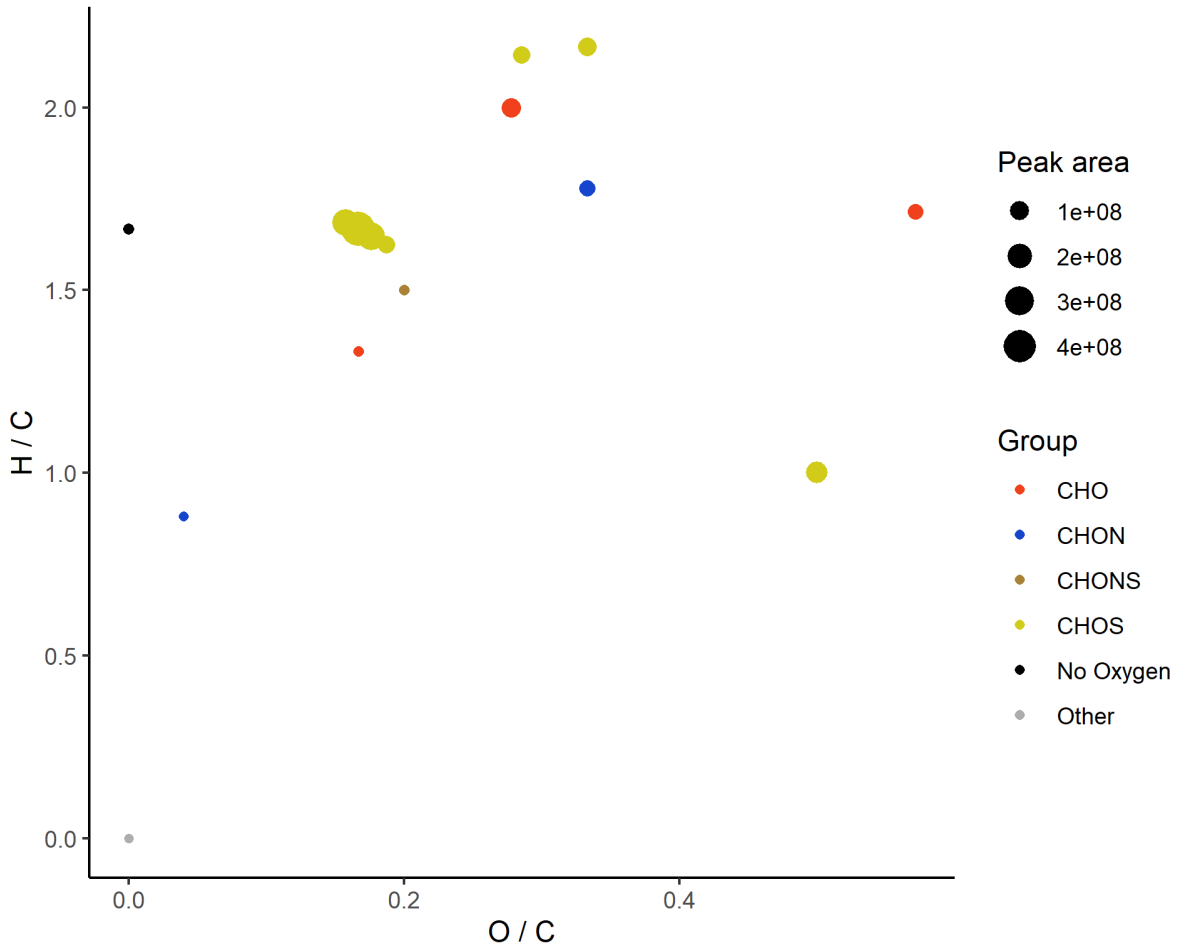

Figure 4.2: Van Krevelen plot for a SPE blank run on the LCMS. As with the solvent blank, most large peaks are sulfates.

As shown in Figures 4.1 and 4.2, most of the largest peaks occur consistently in both blanks. Those that don't often only just pass the filter for the number of observations within the chromatogram peak (Section 4.2.4). For instance, one of the largest sulfate peaks present in each - $C_{18}H_{30}O_3S$ – has 46 and 25 points defining the peak area in the solvent and SPE blanks respectively. The sulfate peaks absent from the SPE blank frequently have only 8-12 points, putting them near the 8-point minimum imposed by the processing in MZmine. Ignoring this threshold gives rise to considerably more peaks, of which some may be genuine, but many are potentially artifacts or will be poorly quantified. The same summary and van Krevelen plots for the same runs without the points filter are given in Table 4.3 and Figures 4.3 and 4.4.

Table 4.3: Features present in the same solvent and SPE blanks processed by LCMS without the MZmine filter for peaks comprised of fewer than 8 observations.

Metric	Solvent Blank	SPE blank
Total features	59	114
Unique formulae	55	72
Formulae only in this blank	18	35

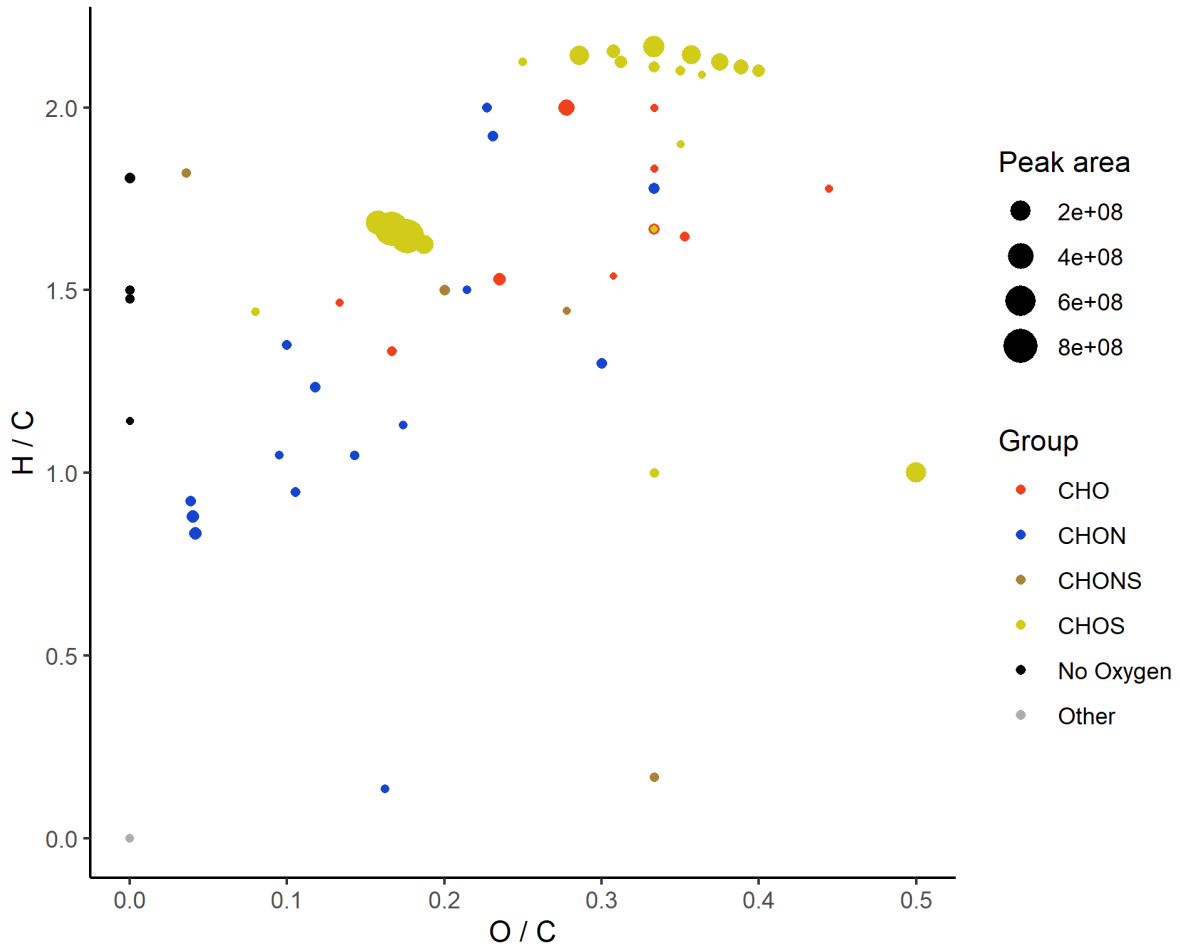

Figure 4.3: Van Krevelen plot for a solvent blank run on the LCMS without the MZmine filter for removing peaks consisting of fewer than 8 observations.

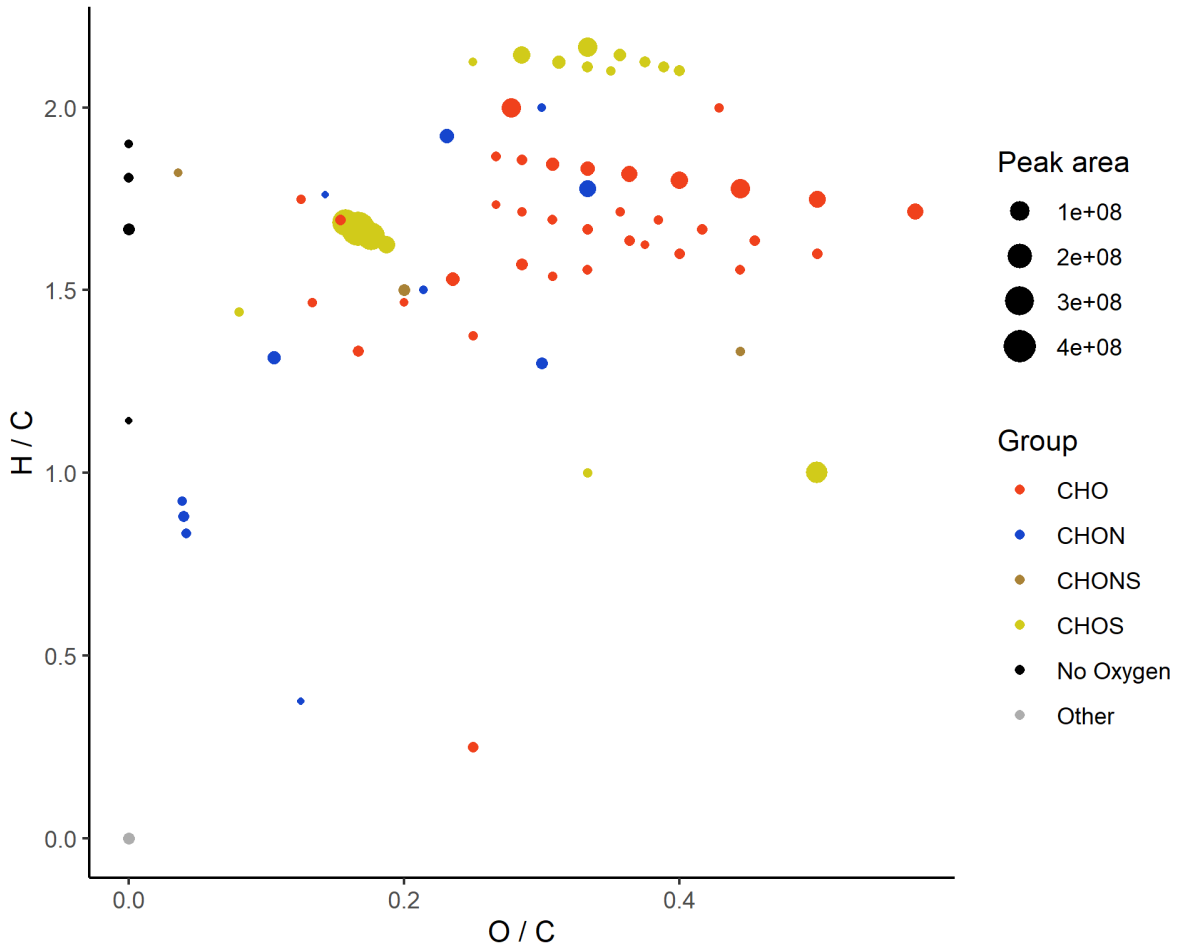

Figure 4.4: Van Krevelen plot for a SPE blank run on the LCMS without the MZmine filter for removing peaks consisting of fewer than 8 observations.

Figures 4.3 and 4.4 show a collection of extra peaks in both blanks. The sulfates that were absent from the SPE blank when the datapoint filter was applied are now present in both blanks, along with several new, smaller peaks. The main obvious difference between the two blanks without the datapoint filter is the presence of a number of CHO compounds, suggesting that these come, at least in part, from the extraction process. The formulae assigned to these 'additional' peaks often contain 4 oxygens, suggesting they are dicarboxylic acids. Taking two examples, a peak for $C_8H_{14}O_4$ is only present in the SPE blank, and the peak assigned $C_9H_{16}O_4$ is >50 times larger in the SPE blank. These are the formulae for octanedioic acid and nonanedioic acid respectively (also called suberic and azelaic acid). These sorts of compounds are of particular interest, as dicarboxylic acids are known products of the ozonolysis of fatty acids. Indeed, Figure 4.4 shows a near-horizontal line of CHO compounds at the top that represent the homologous series of saturated dicarboxylic acids from C7-15, with a number of similar, unsaturated compounds at slightly lower H/C.

This presents a challenge in how compounds such as these are handled. It appears as though small amounts of some dicarboxylic acids can leach into the samples during the SPE process. The presence

of these compounds is not hugely surprising, given their widespread use as plasticisers and lubricants in the chemical industry. However simply discounting compounds present in the blanks would discard an amount of real data; dicarboxylic acids are commonly found in seawater[193–195], whether as a result of pollution or natural biological sources. Therefore, in subsequent analysis of samples, formulae appearing within SPE blanks and solvent blanks are separately flagged to indicate the potential for contamination. Blanks using the datapoint filter in MZmine were used for this purpose for consistency, as all samples were processed using the same filtering.

4.4 Ozonolysis of Organics

An initial experiment was conducted to examine the changes in SPE-DOM composition upon total ozonisation, and assess to what extent these changes were reflected in the metrics discussed in Section 4.2.4. To this end, 12 L of additional underlying water samples were collected from the area around the PPAO and sent from the labs in Plymouth. Since the samples were to be used in isolation as a proof of concept, the samples were not filtered prior to freezing and shipping to save the time spent filtering large extra quantities of water.

Once in York, the 12 × 1 L samples were combined into 6 × 2 L samples (the volume used consistently for SPE), of which 3 were kept as controls. The other three were heavily ozonised by bubbling ozone through each sample. 500 ppb of ozone was generated using a 2B Technologies Model 306 Ozone Calibration Source™. A total flow rate of 216 mL min^{-1} was directed to the samples and split into three lines – one for each sample. In-line taps were used to adjust the individual flows to a roughly consistent flow of 72 mL min^{-1} of 500 ppb ozone per sample. The samples were then left for 20 hours with the aim of largely ozonising reactive components of the DOC. After this time, the three ozonised samples and the 3 control samples underwent SPE, as described in Section 4.2.2.

Due to a mix up with frozen samples, one of the ozonised samples was accidentally comprised of 50% filtered SML rather than just unfiltered ULW. Upon analysis by LCMS, it quickly became apparent that this was ozonolysis sample 2.

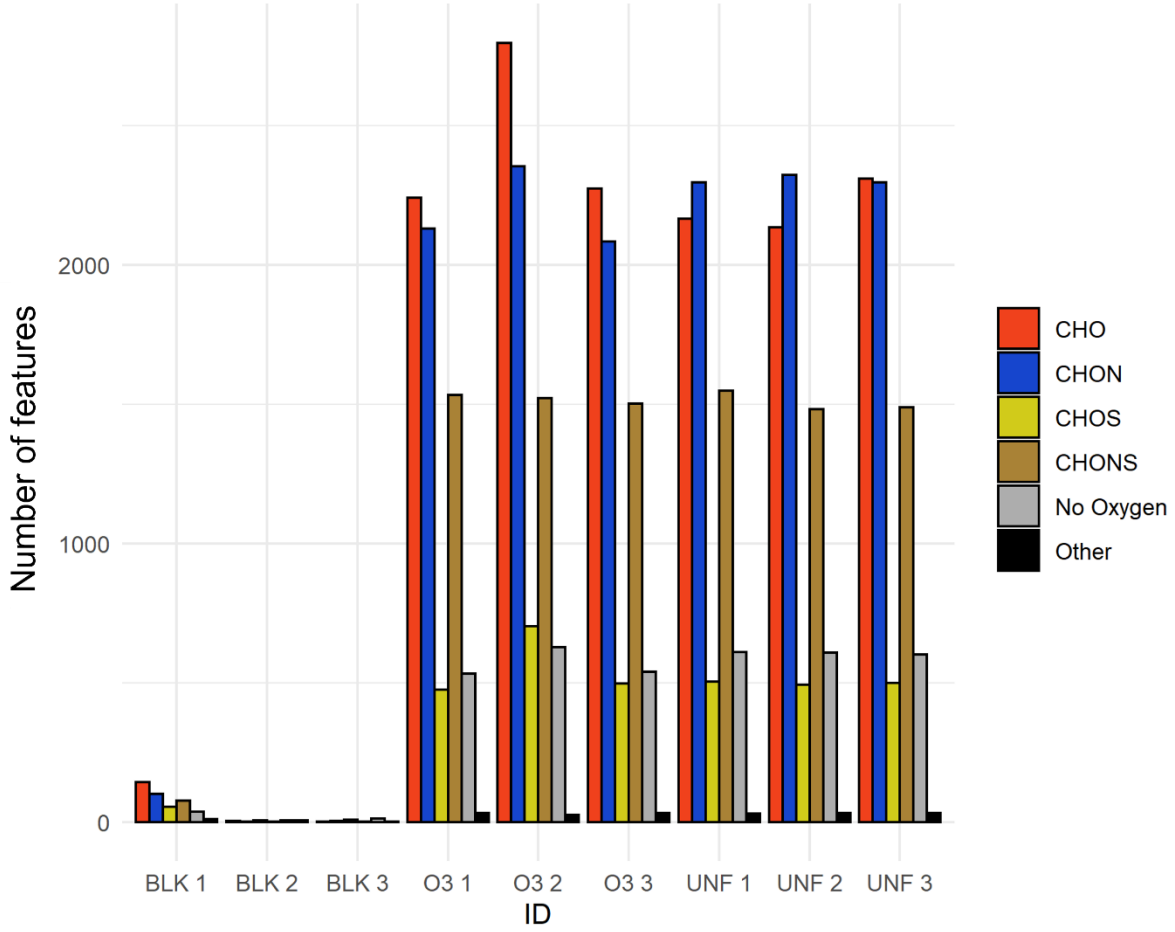

Figure 4.5: Bar plot of the number of identified features in different categories of compound in blanks (BLK 1-3), ozonised (O3 1-3) and unfiltered controls (UNF 1-3). O3 2 is likely the sample containing 50% filtered SML rather than pure unfiltered ULW.

Three solvent blanks run alongside the ozonolysis samples contained comparatively very few features, though the first blank run did have more than the subsequent 2. This is probably residual material within the lines and/or column that were flushed out after the first blank. The second ozonised sample (O3 2) had considerably more peaks than the other two, suggesting that this was the one containing some filtered SML. As such it has been excluded from averages taken from the ozonised samples below. Some compounds may be detected more readily in SML samples if they are enriched there, or some contaminants from either the filtering or the collection process may be present. This sample aside, the distribution of molecule types was fairly consistent across all samples. The only consistent differences were that ozonised samples had consistently fewer CHON compounds and compounds with no oxygen present.

Mean DBE, rAI and rAI_{mod} values were calculated for each run in 3 different ways: entirely unweighted (each feature contributed equally to the mean regardless of peak size), weighted by peak area, and weighted by peak area but with CHOS compounds excluded (due to the presence of several

large sulfate peaks dominating the weighting). Means were taken of all 3 unfiltered samples and ozonised samples 1 and 3, summarised in Tables 4.4 – 4.6.

Table 4.4: Mean DBE in unfiltered samples before and after ozonolysis with standard deviations. Weighted by peak area with and without CHOS compounds, and unweighted.

DBE Weighting	Unfiltered	Ozonised
Weighted	5.47 ± 0.11	5.27 ± 0.26
Weighted (no CHOS)	6.48 ± 0.19	6.20 ± 0.42
Unweighted	8.52 ± 0.05	8.38 ± 0.06

Table 4.5: Mean rAI in unfiltered samples before and after ozonolysis with standard deviations. Weighted by peak area with and without CHOS compounds, and unweighted.

rAI Weighting	Unfiltered	Ozonised
Weighted	0.042 ± 0.003	0.049 ± 0.008
Weighted (no CHOS)	0.116 ± 0.007	0.133 ± 0.014
Unweighted	0.029 ± 0.007	0.027 ± 0.002

Table 4.6: Mean rAI_{mod} in unfiltered samples before and after ozonolysis with standard deviations. Weighted by peak area with and without CHOS compounds, and unweighted.

rAI_{mod} Weighting	Unfiltered	Ozonised
Weighted	0.152 ± 0.002	0.159 ± 0.027
Weighted (no CHOS)	0.238 ± 0.003	0.250 ± 0.052
Unweighted	0.184 ± 0.007	0.183 ± 0.002

The lowest DBE values are observed when all accepted compounds are included in the mean and weighted according to their peak areas. This is likely a consequence of the very large sulfate peaks (with few double bonds) heavily weighting the DBE downwards. Excluding these largest peaks, and other CHOS type compounds from the mean results in an increase of mean DBE of about 1. Unweighted DBE means are the highest, since having all compounds contribute evenly to the mean results in a large number of small peaks with large *m/z* formulae and many double bonds drag the average up. Since the peak areas of different compounds are not directly comparable, it is hard to say which of the weightings used is most appropriate, hence all are presented here. Regardless of the weighting used, however, DBE is consistently slightly lower in ozonised samples than in the controls (+0.14 – 0.28), though there is overlap within the standard deviations of the groups. An explanation for this would be that ozone tends to react at the site of double bonds in long, unsaturated carbon chains. This results in larger, double bond-containing compounds being broken into smaller

compounds with fewer double bonds. If a bulk change in DBE can be observed upon ozonisation of the SML, then it may be possible to some degree to predict the reactivity of ozone to a water sample based on DBE.

The aromaticity indexes, rAI and rAI_{mod} present a less clear picture. rAI values are lower than rAI_{mod} values due to it being a more stringent qualifier of the presence of aromatic systems. Weighted values without CHOS compounds show some increase in aromaticity after exposure to ozone, though weighted rAI_{mod} with CHOS compounds, and both metrics when unweighted show little to no change. This is perhaps because the reaction of ozone with aromatic systems does not always lead to the removal of aromaticity. For instance the reaction of ozone with phenol has been shown to produce hydroquinone and catechol, both benzene diols, along with non-aromatic benzoquinone and *cis,cis*-muconic acid[196]. Therefore, while aromatic compounds may be reactive to ozone, they may not change much in their aromaticity overall upon reaction.

Table 4.7: Mean oxygen:carbon ratio in unfiltered samples before and after ozonolysis with standard deviations. Weighted by peak area with and without CHOS compounds, and unweighted.

O/C	Unfiltered	Ozonised
Weighted	0.220 ± 0.008	0.220 ± 0.039
Weighted (no CHOS)	0.243 ± 0.017	0.235 ± 0.075
Unweighted	0.311 ± 0.002	0.311 ± 0.0003

Table 4.8: Mean nitrogen:carbon ratio in unfiltered samples before and after ozonolysis with standard deviations. Weighted by peak area with and without CHOS compounds, and unweighted.

N/C	Unfiltered	Ozonised
Weighted	0.045 ± 0.003	0.050 ± 0.011
Weighted (no CHOS)	0.072 ± 0.005	0.080 ± 0.025
Unweighted	0.086 ± 0.0005	0.085 ± 0.00004

Table 4.9: Mean hydrogen:carbon ratio in unfiltered samples before and after ozonolysis with standard deviations. Weighted by peak area with and without CHOS compounds, and unweighted.

H/C	Unfiltered	Ozonised
Weighted	1.447 ± 0.020	1.446 ± 0.067
Weighted (no CHOS)	1.259 ± 0.048	1.266 ± 0.123
Unweighted	1.282 ± 0.013	1.286 ± 0.005

The average atomic ratios of oxygen, nitrogen and hydrogen to carbon were also considered in a similar fashion to double bonds and aromaticity, summarised in Tables 4.7 – 4.9. Unlike DBE and AI, there is no obvious change in any of the ratios, regardless of the weighting, before and after ozonisation. The only values that show any real change are the weighted N/C values, though it's hard to say definitively that this is a significant change given the low overall number of nitrogen atoms present compared with oxygen and hydrogen. This is reflected in the similar appearances of van Krevelen diagrams before and after, shown in Figures 4.6 and 4.7 respectively.

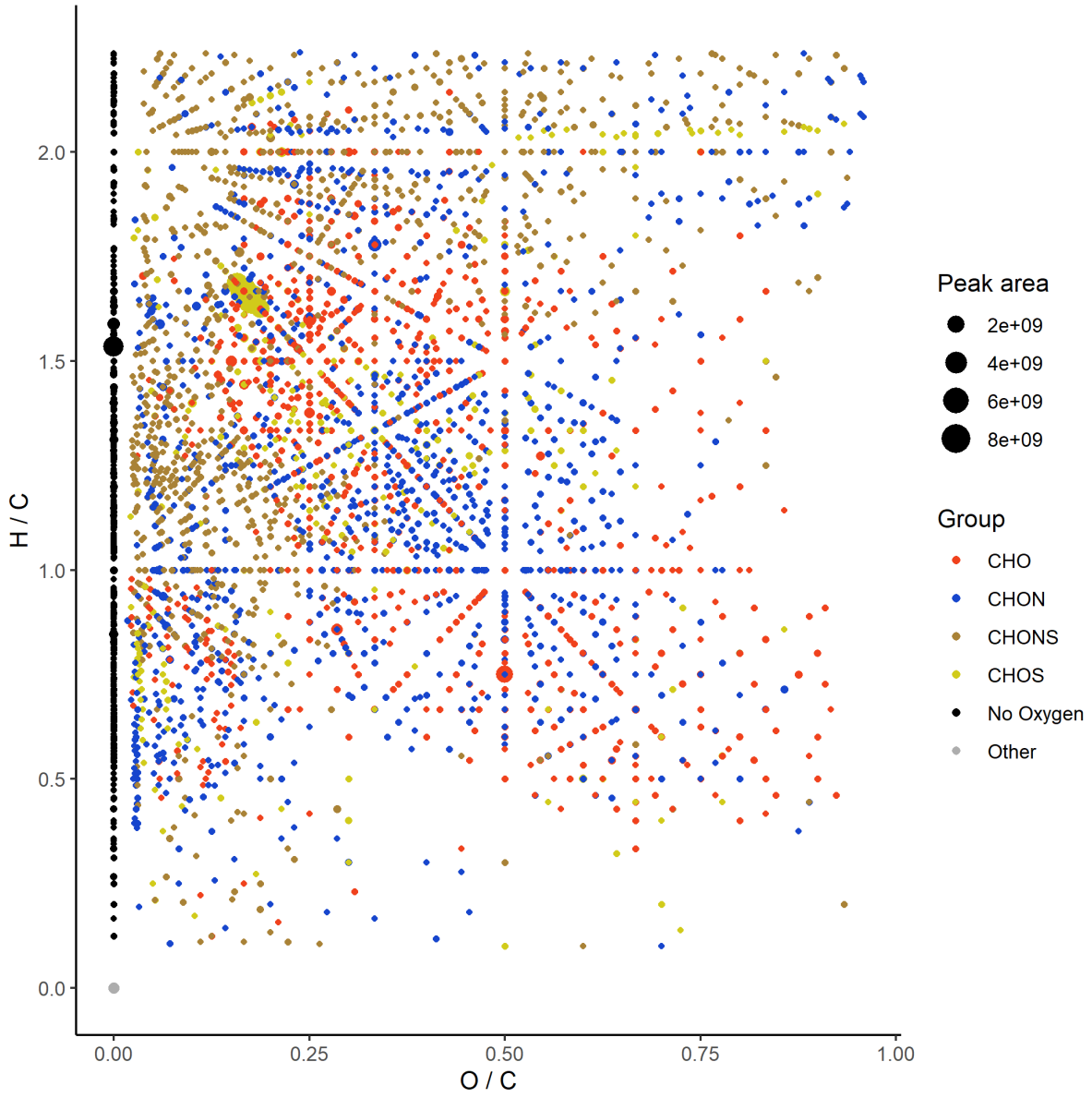

Figure 4.6: Van Krevelen plot of the unozonized, unfiltered sample UNF 1.

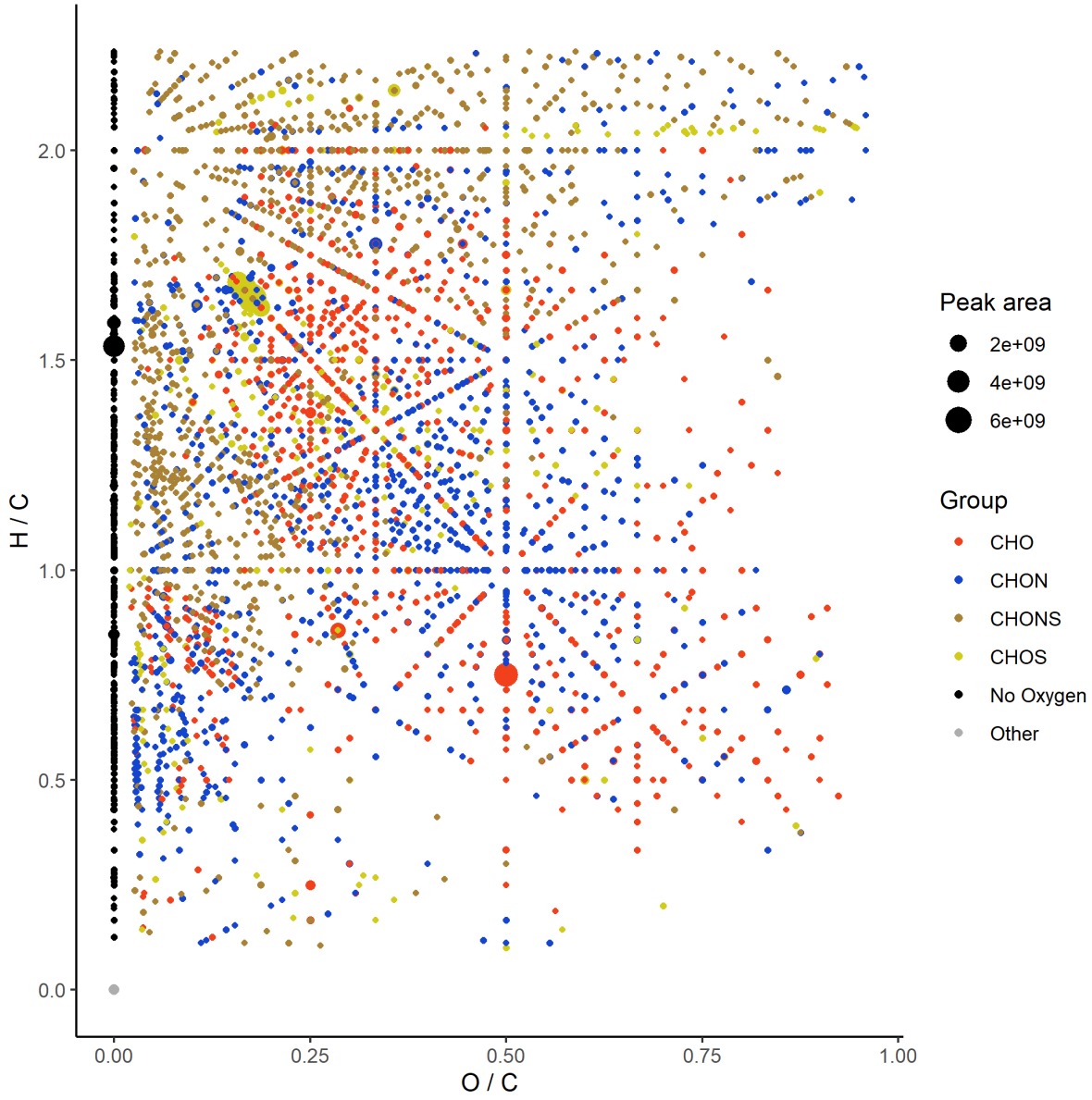

Figure 4.7: Van Krevelen of ozonised, unfiltered sample O3 1.

Figures 4.6 and 4.7 clearly show substantially more chemical complexity than the van Krevelen plots of the solvent and SPE blanks (Figures 4.1 and 4.2) and are broadly similar to one another in their overall appearance. Both show the large peaks of sulfate compounds identified in the blanks, though note that the size of these peaks is approximately an order of magnitude higher here. Many CHO compounds are clustered in the top left of each plot, suggesting that a number of fatty acids or dicarboxylic acids may be present in both samples. A selection of these compounds can be interrogated in more depth to see whether the quantities present differ significantly before and after ozonisation. The largest CHO peak in each plot was assigned the formula $C_8H_6O_4$, and can be seen as a large red dot on the vertical O/C = 0.50 line. This formula matches that of terephthalic acid – a benzene ring with two carboxylic acid groups – which is a precursor to polyester. Interestingly, this

was not seen in any blanks – neither the solvent and SPE blanks discussed in Section 4.3, nor the solvent blanks run alongside the ozonolysis samples. This suggests that it is reliably detectable in the collected water samples, though there was no clear variation of peak area before and after exposure to ozone. This is expected, as phthalic acid contains two carboxylic acid groups which would deactivate the aromatic system with respect to electrophilic attack by ozone.

A clear, consistent peak like that of $C_8H_6O_4$ is useful in examining the variation in retention time (RT) between samples run consecutively. Many of the formulae consistent with acids of interest often appear on multiple occasions at different RTs due to the existence of structural isomers. Since RTs will never be identical, it is useful to have an expected range of variation to help consistently pick peaks corresponding to a single isomer. In the case of terephthalic acid, the RT across all unfiltered samples, before and after ozonolysis, varied from 3.22 to 3.26 minutes. A range of ±0.15 minutes for RT can therefore reasonably be expected for a given molecule (since variation may be slightly higher at longer RTs). With these bounds, the change in several compounds was examined due to exposure to ozone.

The ozonised and control samples were examined for the presence of a number of saturated FAs (lauric $C_{12}H_{24}O_2$, myristic $C_{14}H_{28}O_2$, palmitic $C_{16}H_{32}O_2$, and stearic $C_{18}H_{36}O_2$) and unsaturated FAs (myristoleic $C_{14}H_{26}O_2$, palmitoleic $C_{16}H_{30}O_2$, oleic $C_{18}H_{34}O_2$, linoleic $C_{18}H_{32}O_2$, and linolenic $C_{18}H_{30}O_2$). Of all of these FAs, only formulae corresponding to lauric acid and myristoleic acid were identified in any of the samples (at any RT), and in these two cases the matching formulae were only present in sample O3 2 which contained 50% filtered SML rather than 100% unfiltered ULW.

It is clear then that since observations of reactive FAs require a different methodology, the observation of the products of FA ozonolysis may prove more reliable. With a similar approach to the FAs above, dicarboxylic acids were examined, all saturated, from length C7 – C15. The results are visualised in Figure 4.8.

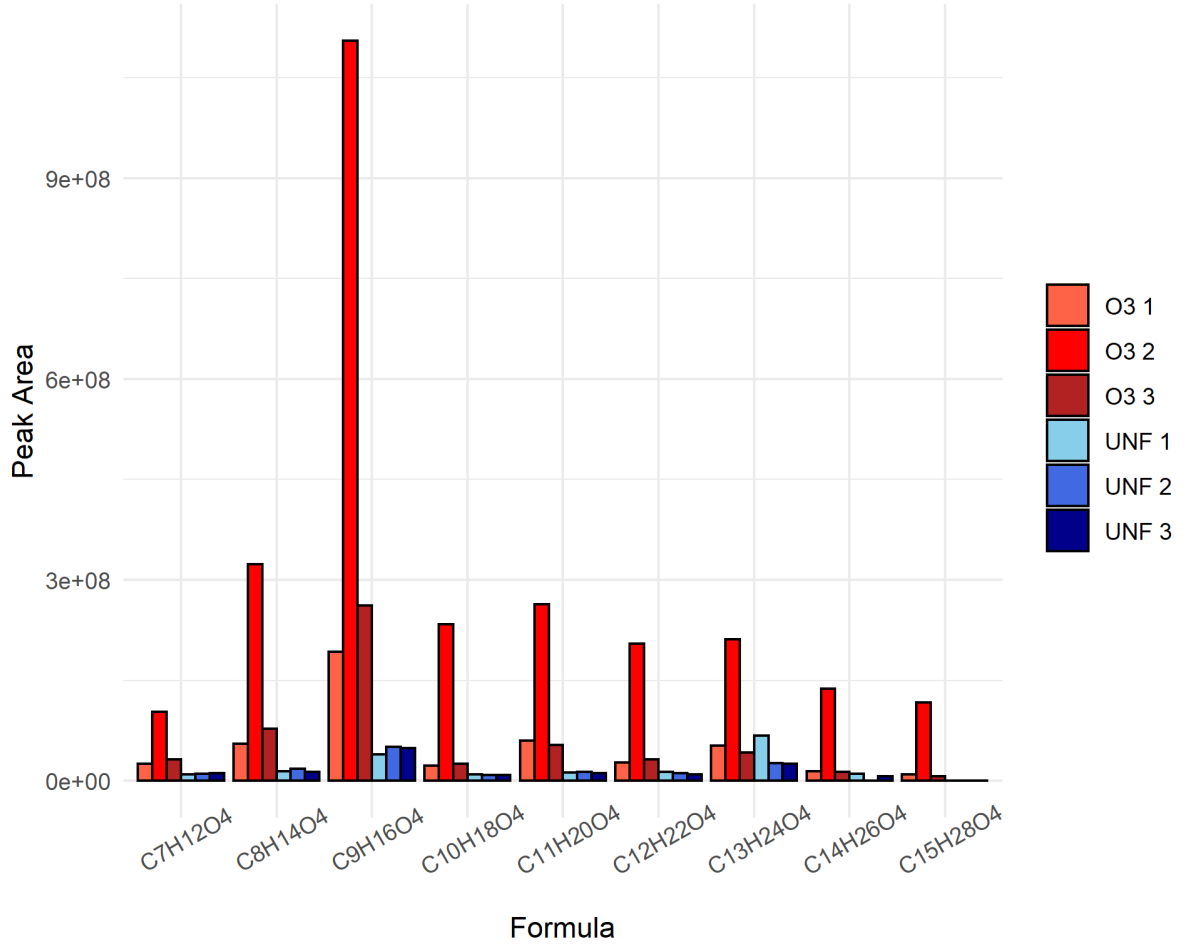

Figure 4.8: Peak areas of the formulae of the dicarboxylic acids from C7 – C15 in unfiltered ULW samples before and after ozonisation.

As has been noted before, sample O3 2 is vastly different from the other ozonised samples as a result of containing 50% filtered SML. The scale of the difference is interesting, but is hard to attribute to a single factor – it could be caused by any combination of difference in composition of the SML, cells lysing during freezing, or materials introduced from the Garrett screen used for sample collection.

That outlier aside, there is still a marked difference between ozonised samples and the controls. Assuming peak area to be proportional to the amount of a given single compound present across these runs, the amount of dicarboxylic acids present after ozonolysis increased for every compound examined with the exception of $C_{13}H_{24}O_4$, for which the first control had a larger peak than any other sample. The two longest chain dicarboxylic acids also had a less marked difference, with all peaks (besides that from O3 2) being comparatively small, and indeed fully absent from some of the control samples. Still, the increase in dicarboxylic acids of length C7-C12 is quite strong, and suggests that these may be interesting species to attempt to observe in the samples collected over a long timescale near the PPAO.

4.5 Time Series at the PPAO

Alongside the samples collected from the flux footprint near the PPAO for I^- and DOC measurements (Section 3.2.1), SML and ULW samples for SPE-DOM analyses were also collected, of which the first 30 have been analysed according the same methodology as the ozonolysis samples. This covers the time period of 11/11/19 until 24/08/20, with some small breaks in sampling around December 2019 and February 2020.

In Section 3.3.2, the concentration of DOC in the SML and ULW was discussed, and it was observed that the concentration of DOC in the SML appeared to fall ~40% during the timeframe of the SPE-DOM samples discussed here. As such, the series of samples were investigated for any changes in DBE or AI, both over time and between layers to see if any bulk changes of these metrics accompanied the apparent drop in concentration. The presence of dicarboxylic acids, found to measurably increase in samples exposed to high ozone, was also investigated. Initially though, examination of some sample van Krevelen plots revealed that the number of compounds being identified in the time series samples was considerably lower than in the ozonolysis experiments. Examples using the data from the first week's SML and ULW samples are shown in Figures 4.9 and 4.10 respectively.

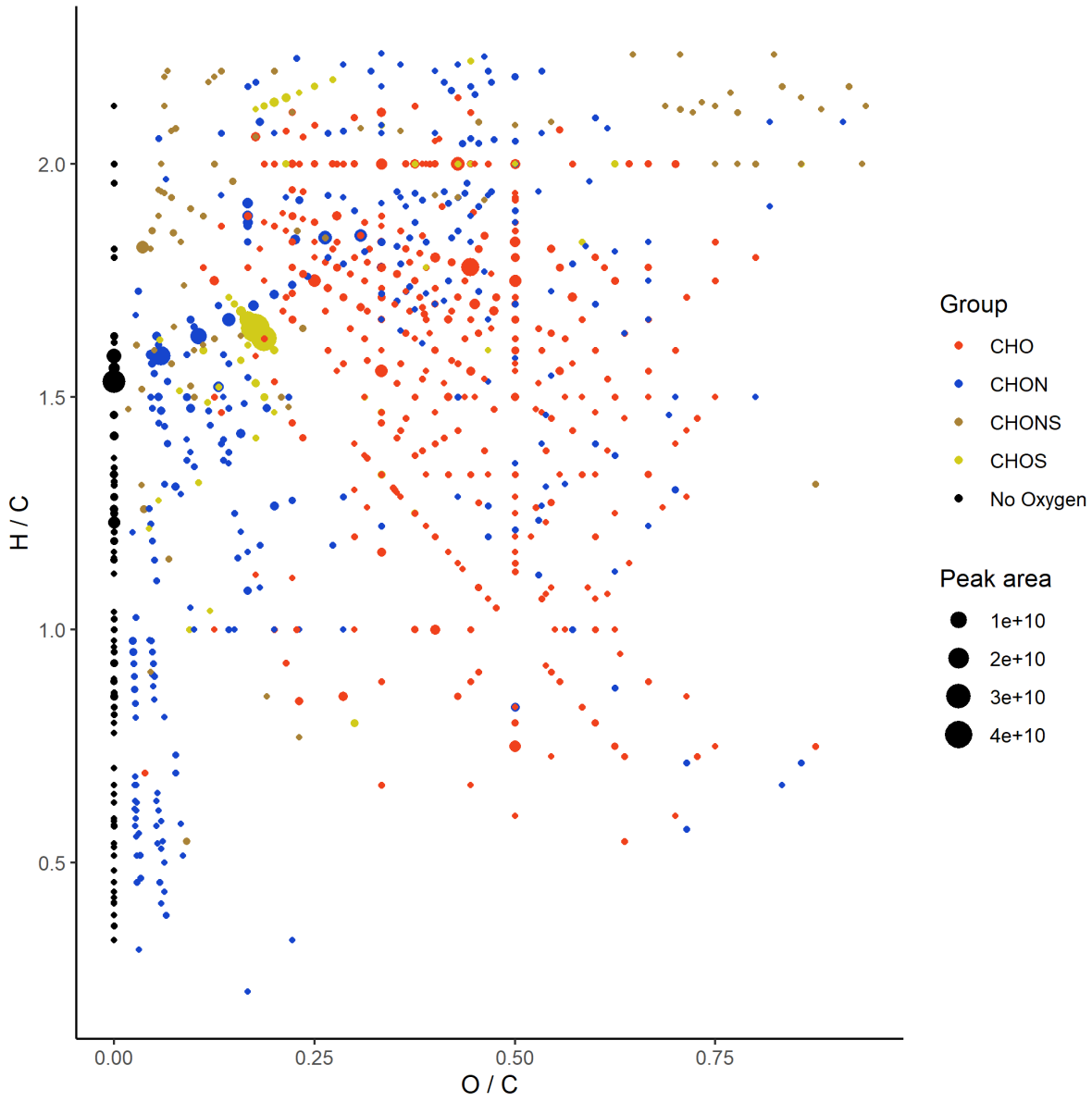

Figure 4.9: Van Krevelen plot for the SML sample, week 1 of the time series.

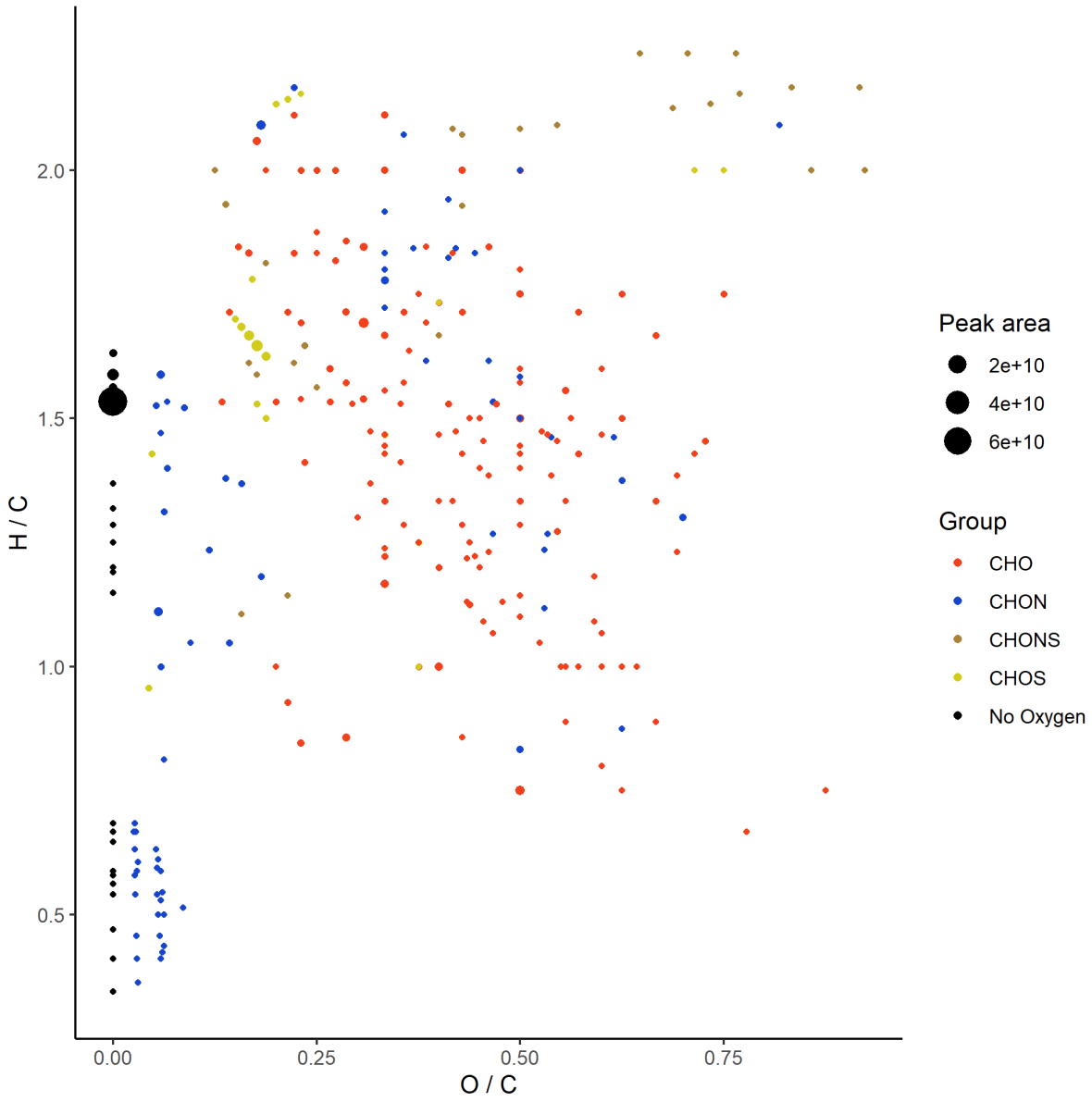

Figure 4.10: Van Krevelen plot for the ULW sample, week 1 of the time series.

Comparing Figures 4.9 and 4.10 to the van Krevelen plots of the ozonolysis experiments (Figures 4.6 and 4.7), there are clearly far fewer features identified in the former despite the same extraction and analysis procedure being in place for both sets of samples. Ozonolysis samples typically saw ~6000 features assigned formulae, whereas the time series samples were more in the range 500-1000. The unfiltered nature of the ozonolysis samples is bound to have an effect on the organics present, so this is possibly a factor. However, the accidental inclusion of filtered SML water into O3 2 still lead to a similar number of peaks, of which the dicarboxylic acid peaks were often stronger. This agrees with the observed greater presence of dicarboxylic acids in SML samples than in the ULW, see Figure 4.15.

The time series samples were analysed on the Orbitrap approximately a month after the ozonolysis samples, and the instrument was undergoing a series of cleans and maintenance checks around that time period. Another possible explanation therefore is that, in spite of the LCMS settings being consistent, the cleanliness and performance may have altered in the time between batches of samples being run. Figure 4.11 shows the ion chromatogram for two ozonolysis controls (UNF1 and 3, red and green respectively) and for the ULW sample from week 30 of the series (blue). Clearly considerably fewer ions were reaching the detector in the case of week 30 ULW, potentially resulting in fewer features being detected in the time series samples.

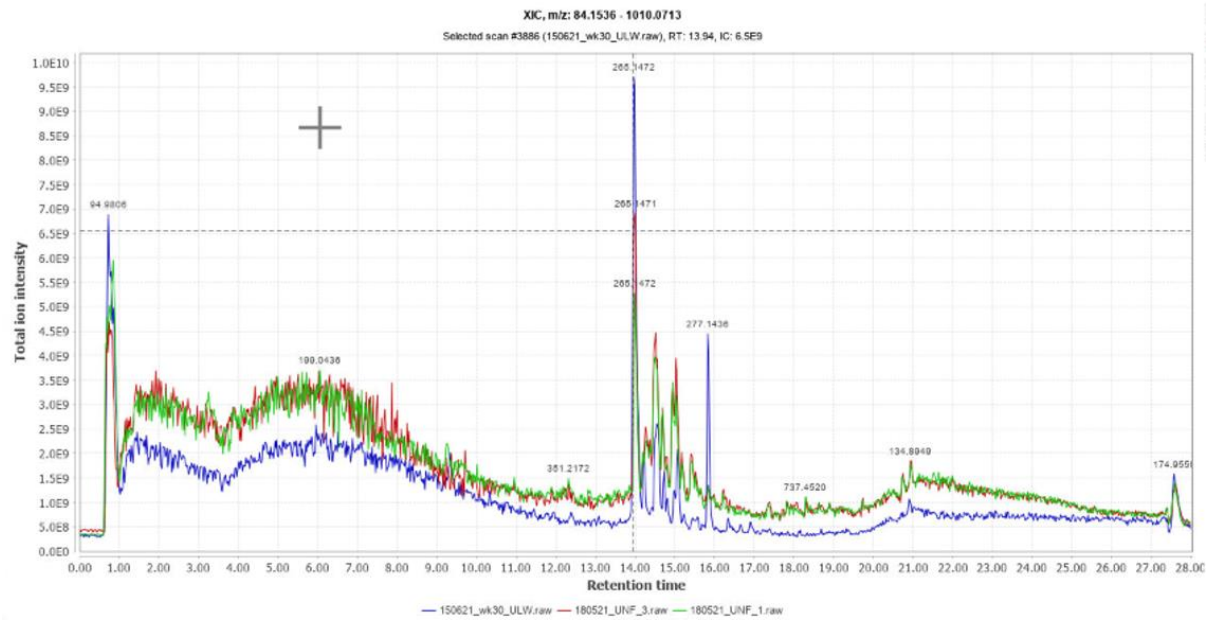

Figure 4.11: Total ion intensity of samples UNF1 and 3 (green and red respectively) and of week 30 ULW (blue).

Still, many of the large features in the ozonolysis samples exist within the time series, but it should be kept in mind that the number of formulae assigned and used to calculated DBE, rAI and rAI_{mod} are considerably lower.

In the same fashion as the ozonolysis samples, mean DBE, rAI and rAI_{mod} values were calculated for each sample, unweighted, weighted by area, and weighted by area in the absence of CHOS compounds (which included large peaks dominating the weighted results). The variation in DBE with different weighting is shown in Figure 4.12.

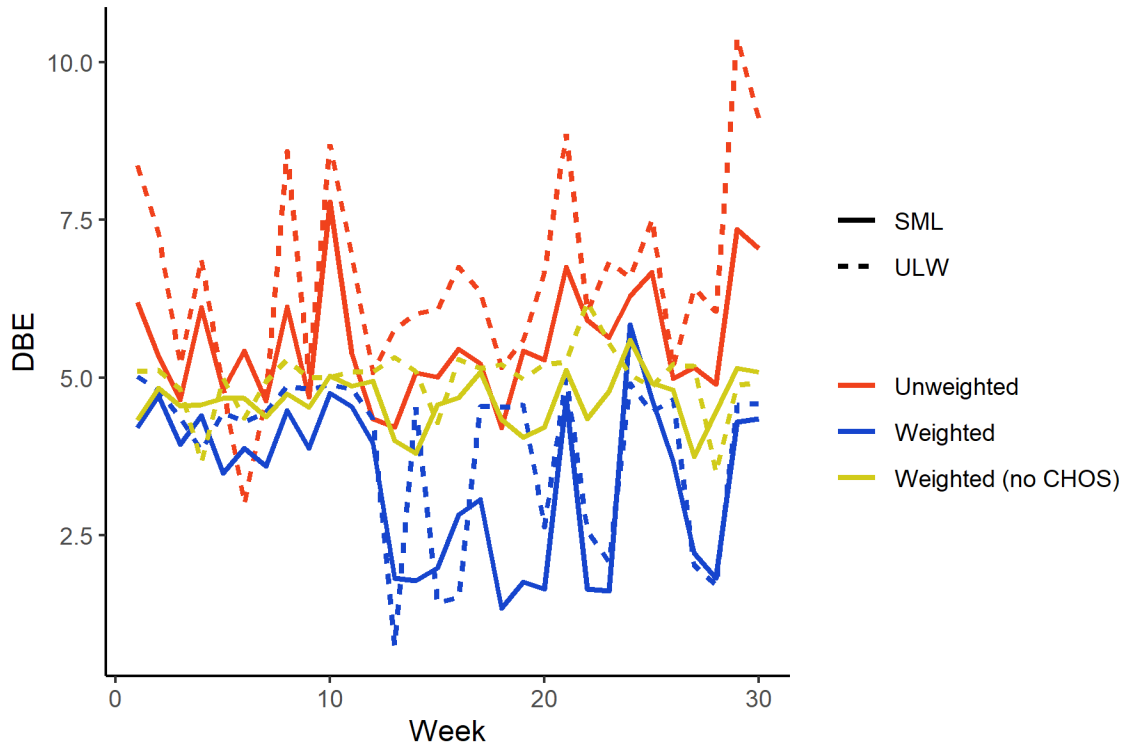

Figure 4.12: Variation in DBE over time in SML (solid line) and ULW (dashed line) samples, unweighted (red), weighted according to peak area (blue), and weighted according to peak areas, but with CHOS type compounds excluded (yellow).

While a consistent drop in DBE is observed after exposure to high ozone (Table 4.4), no particular trend in DBE emerges over the course of the time series. The only somewhat consistent result in that the unweighted DBE in the SML is almost always lower than that of the ULW. The mean unweighted DBE in the SML across all weeks was 5.53, compared to 6.53 in the ULW samples. This suggests that molecules with many double bonds are less abundant in the SML, possibly as a result of the reaction with ozone breaking the double bonds. This pattern is present, though less pronounced, in the weighted DBE values; mean weighted DBE was 3.36 in the SML and 3.87 in the ULW, and 4.63 and 4.98 respectively with CHOS compounds excluded. This suggests that the unweighted difference between SML and ULW is caused by numerous compounds with small responses that are less significant when formulae are weighted by area.

Similarly to DBE, rAI and rAI_{mod} showed no particular variation over time. This is not surprising, given the similar ways in which the metrics are calculated. While these parameters revealed no obvious pattern over the course of measurements, examination of the dicarboxylic acids present in the ozonised samples did yield some clearer variation.

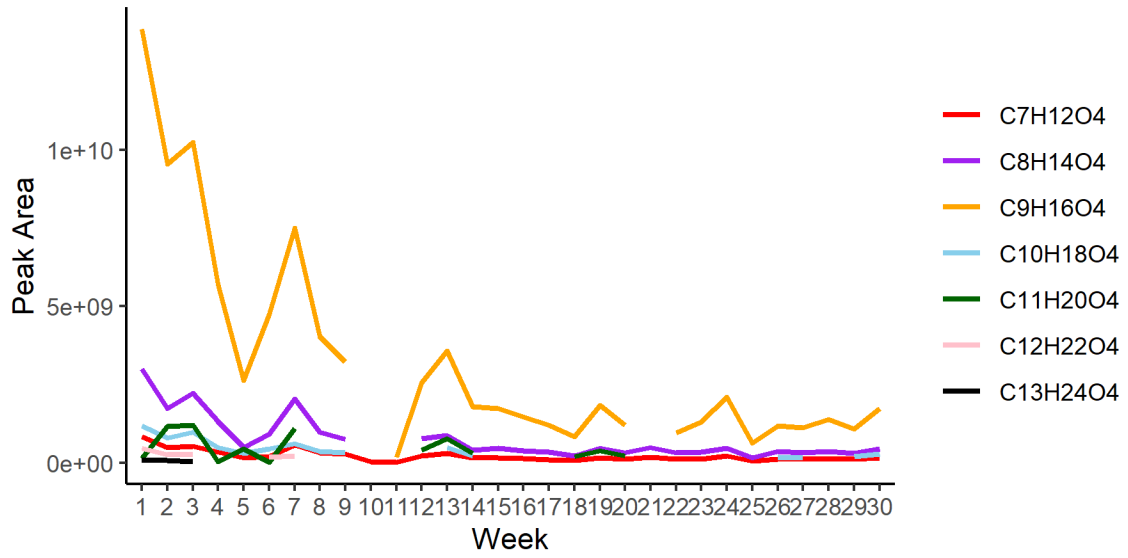

Figure 4.13: Change in dicarboxylic acid peak area in SML samples from C7 to C13 over 30 weeks.

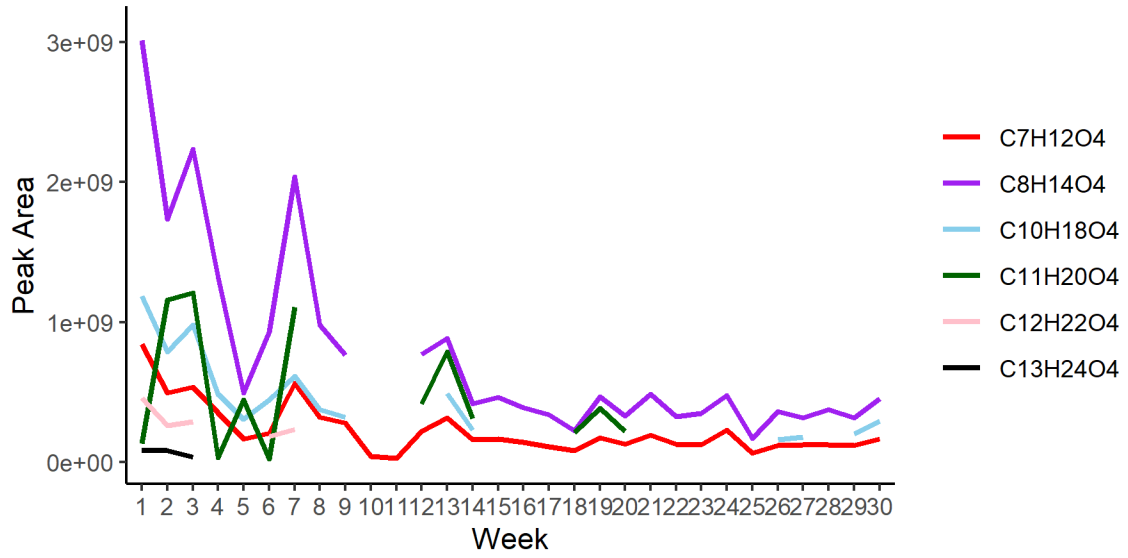

Figure 4.14: Change in dicarboxylic acid peak area in SML samples from C7 to C13 over 30 weeks, rescaled without $C_9H_{16}O_4$.

Figures 4.13 and 4.14 show the peak areas of the dicarboxylic acids from C7 to C13 over the course of the 30 weeks. The response of $C_9H_{16}O_4$, azelaic acid, dwarfs that of most other compounds in the early weeks, but decreases sharply over the course of the measurements. Furthermore, pimelic acid ($C_7H_{12}O_4$), suberic acid ($C_8H_{14}O_4$), and sebacic acid ($C_{10}H_{18}O_4$) all show decreases over the same timescale to varying extents. Intuitively this would appear to compliment the decreasing amounts of DOC observed in the SML over this time. Although, while DOC concentrations did drop

considerably, it only ever halved in concentration at the most extreme, whereas for some dicarboxylic acids, suberic and azelaic especially, peak areas decline an order of magnitude or more, far more than would be expected from the simple decrease in DOC. Examining the same compounds in the ULW samples for the same period yields very different results.

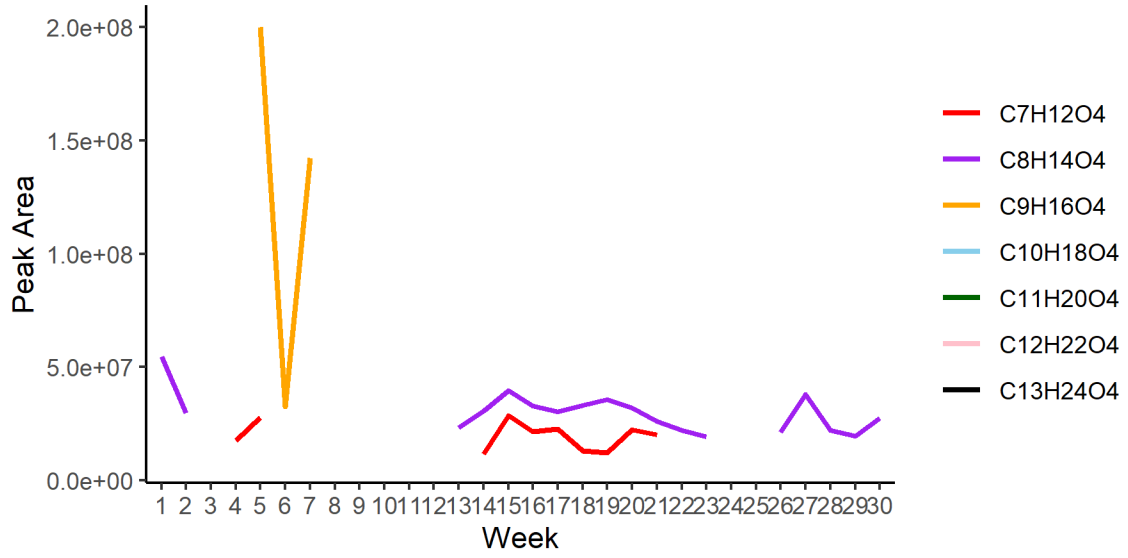

Figure 4.15: Change in dicarboxylic acid peak area in ULW samples from C7 to C13 over 30 weeks. Only C7-9 were reliably observed.

Not only is there no apparent change over time in the dicarboxylic acids in the ULW, but the magnitude of the peak areas for each are roughly an order of magnitude lower than the SML samples. In the majority of cases, no formula is even assigned, especially for the larger molecules. While some difference between the SML and ULW compositions may be expected, it seems highly improbable that this large difference accurately reflects the environment; previous work reports the DOC being enriched in the SML by a factor of 1.2 – 2.8 compared with underlying water[197]. Given the identical treatment of samples throughout SPE and analysis, the only outstanding difference in the treatment of the two sets of samples is the use of the Garrett screen in collecting SML, as opposed to the ULW being collected by an underway system. In weeks 7 and 30, 'procedural blank' samples were taken in which artificial seawater was poured over the Garrett screen prior to filtering and storing to at least partially mimic the contact with the Garrett screen experienced by SML samples. By analysing the presence of dicarboxylic acids in these blanks, the potential introduction of material from the Garrett screen can be tested.

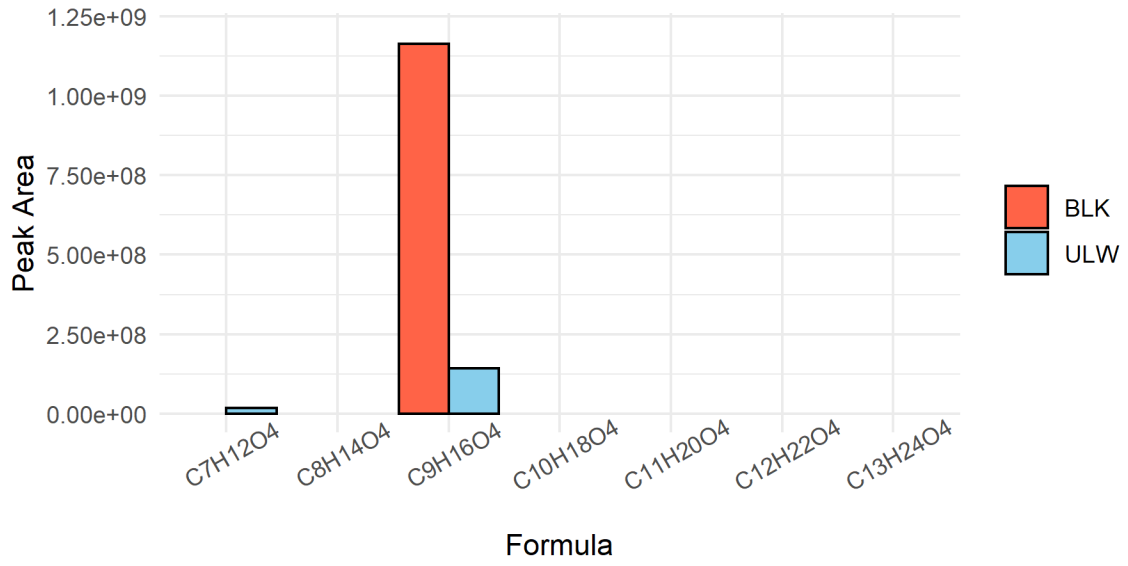

Figure 4.16: Dicarboxylic acid peak areas observed in the procedural blank (red) and ULW (blue) during week 7 of the time series.

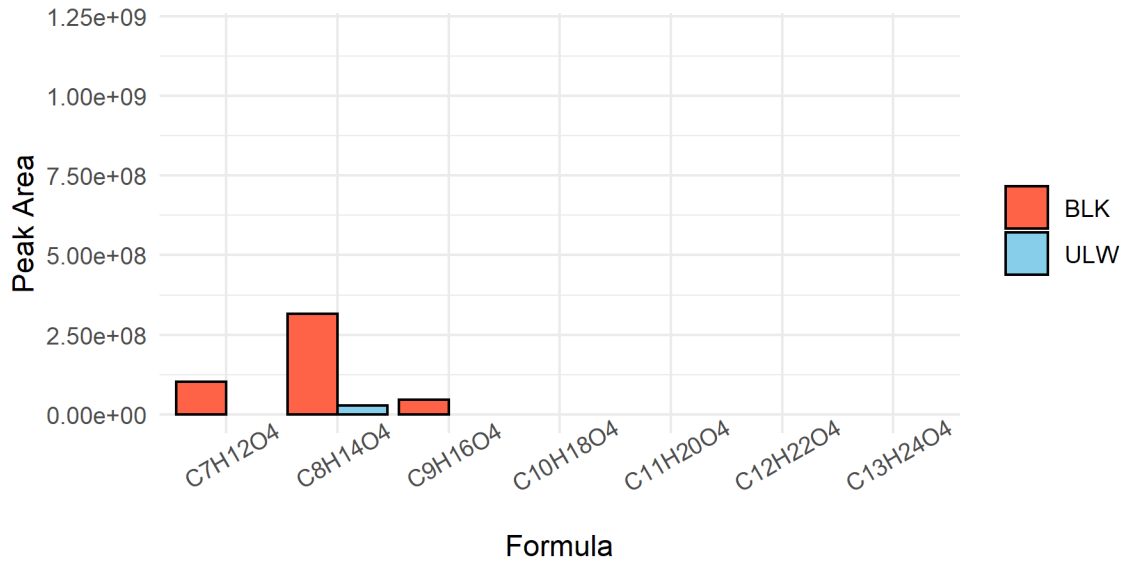

Figure 4.17: Dicarboxylic acid peak areas observed in the procedural blank (red) and ULW (blue) during week 30 of the time series.

Similarly to the ULW, the dicarboxylic acids with longer carbon chains were never identified in the procedural blanks. However in week 7, azelaic acid had a far stronger signal in the blank than in the ULW. In weeks 30, a small azelaic acid peak is observed, when it is absent from the corresponding ULW sample. This could be consistent with material on the surface on the mesh of the Garrett screen leaching into the samples, slowly depleting over time. Indeed, the manufacturers of the mesh to be used in the construction of new Garrett screens states on their website that 'As a result of the

manufacturing process, some mesh or mesh products may still have a light lubricant on its surface' (https://themeshcompany.com/handling-mesh/, accessed 20/09/21), and dicarboxylic acids see industrial use as lubricants and plasticisers. While efforts were made to clean the mesh prior to use, it is possible that contaminants remained. Pimelic and suberic acid also see larger peaks in the blank than in the ULW, though sebacic acid is absent from blanks and ULW samples in both weeks 7 and 30, despite showing a somewhat unsteady decline over the first 10 weeks of sampling. A greater number of procedural blanks alongside future samples will help make this issue clearer. So too will the extension of the time series into the winter of 2020/21 – if DOC in the SML raises again, then a corresponding rise in the variable dicarboxylic acids would suggest a genuine link, whereas a divergence in trends would point to the leaching of material from the Garrett screen.

4.6 Conclusions

Unfiltered ULW samples showed some bulk change in organic composition following prolonged exposure to large amounts of ozone; DBE consistently decreased after exposure, reasoned to be due to ozone reacting at these sites in molecules and breaking them down into smaller compounds with fewer double bonds. Measures of aromaticity in contrast showed no consistent change, perhaps on account of ozonolysis of these compounds often resulting in the aromaticity of the species being retained. A number of fatty acids previously identified in seawater commonly failed to be identified via LCMS, whether before or after ozone exposure. However, a number of dicarboxylic acids – products of the ozonolysis of fatty acids – were consistently identified and were found to be more abundant in samples exposed to ozone.

30 sets of SML and ULW samples from the waters around the PPAO, along with some procedural blanks, were also analysed via LCMS. These samples covered from 11/11/19 until 24/08/20, and commonly yielded far fewer identified features than the ozonolysis samples. This is reasoned to be a combination of more/different chemical species being present in the ozonolysis samples due to them not being filtered, and the potential change in instrument sensitivity between runs on account of maintenance on the Orbitrap LCMS. Measures of double bonds and aromaticity were variable from sample to sample but formed no clear seasonal pattern. However, a slight elevation in DBE in ULW samples was observed compared with the SML samples, which could be caused by the loss of several reactive compounds with individually very small responses.

Although few of the dicarboxylic acids could reliably be detected in the ULW samples, several were found consistently in the SML samples with a number of them, azelaic acid ($C_9H_{16}O_4$) especially, decreasing sharply over the course of the first ~10 SML samples. This partially compliments the

decrease in DOC concentration measured in the SML around the PPAO in the same period, but at this stage we cannot rule out contamination of the Garrett screen as a source of dicarboxylic acids.

Procedural blanks, in which ULW was poured over the Garrett screen, showed higher levels of pimelic, suberic and azelaic acids (C7-9) than the corresponding weeks' ULW samples. The effect was strongest for azelaic acid in week 7, suggesting that some dicarboxylic acids could be leaching from the Garrett screen mesh into samples, slowly depleting over time. Sebacic acid though was not identified in either of the blanks, though still displayed some decrease early on in the series. It is therefore hard to say to what extent this trend is a consequence of the dicarboxylic acids present decreasing as overall DOC concentration decrease, and to what extent it is affected by contamination from the Garrett screen. The collection of these samples, along with more blanks, have continued into 2021, so future samples may help resolve this. If DOC concentrations rise again, a corresponding rise in the dicarboxylic acids would point to a genuine signal (as the amount of contaminants on a screen ought to decrease over time with use). A divergence between these two sets of data however would suggest the introduction of material from the Garrett screen to be responsible for much of the change. A simple experiment could also be run in which a newly constructed screen is used to collect controls from a container of pure water. This would allow any compounds leeching off the Garrett screen to be identified, and give an idea of the timescale of use over which this contamination abates.

Overall, DBE has been shown to vary with exposure to ozone in the lab. SML samples also showed consistently lower DBE than ULW samples, suggesting a detectable difference in the composition of the two layers which may be a result of the reaction of ozone within the SML. However the variation in metrics such as DBE between repeats suggests that resolving small changes over time would be challenging. A better approach may be to use ozonolysis experiments to identify compounds of interest which show large changing in signal before and after exposure to ozone. These can then be the subjects of more targeted, possibly quantitative, analyses. In cases where isomers are impossible to separate on the basis of exact mass alone, tandem mass spectrometry could be used to distinguish between compounds based on their fragmentation patterns. Dicarboxylic acids have been discussed in this work as an expected product of fatty acid ozonolysis, and greater concentrations of many of these compounds was observed following exposure to ozone. Compounds such as phenols and amines could be other compounds to focus on changes in signal before and after ozonisation. The absence of fatty acids themselves in the mass spectra presented here highlights that not all compounds are detected well by this LCMS method. Analysis by other techniques such as GSMS or the derivatisation of reactive or unstable species will be necessary to obtain a more complete picture of DOC composition. Likewise, the process of solid phase extraction is not perfect, and alternatives such as liquid-liquid extraction or supported liquid extraction could be investigated to assess whether different parts of the DOC can be observed.

5. Summary, Conclusions, and Future Work

5.1 Overview

The work presented here aims to quantify ozone deposition to the sea from a coastal site and to improve our knowledge of its biogeochemical controls to help characterise the importance of oceanic ozone deposition in the tropospheric ozone budget. The eddy covariance method was used to collect ozone deposition observations at the PPAO on the UK south-coast, with semi-continuous measurements spanning from 2018 to 2021. Seawater samples were collected from the waters surrounding the observatory and analysed for iodide, dissolved organic carbon, and the molecular composition of dissolved organic material. This represents the first field study linking oceanic fluxes of ozone to the chemical composition of the surface seawater.

5.2 Eddy Covariance Measurements at Penlee Point

Chapter 2 focused on the ozone flux measurements themselves, the treatment of data necessary to obtain a good oceanic signal, and the errors associated with these measurements. Two high-frequency chemiluminescent ozone detectors were used over the course of the project, both of which agreed well with UV-based calibration instruments, and showed little effect from water vapour interference. Wind data were collected by a sonic anemometer co-located with the ozone inlet at the top of the PPAO, ~19 m above sea level. Together, these high-frequency ozone and wind data were used to calculate fluxes using the eddy4R codebase, with the lag between ozone and wind data being corrected for by using cross-correlation functions. 20-minute averaging intervals were used for the first and third deployments, and 60-minute intervals were used for the second to help counteract the effects of lower instrument sensitivity. Typically frequent south-westerly winds together with the landscape around the PPAO limited the sector in which reliable oceanic data could be gathered to 180-240° from north. Deposition velocity and roughness length values were both observed to be considerably elevated during periods of low wind speeds, contrary to expectations for an oceanic observation. This indicated an influence of land on both the turbulent characteristics of the winds and so on the deposition values, limiting their ability to accurately reflect an oceanic environment. Periods with average wind speeds below 4 m s^{-1} were excluded – the point below which both deposition velocity and roughness length showed an increase. Footprint analysis of the first deployment reinforced the view that land could affect deposition greatly at low wind speeds, and the land areas present in the footprints during different wind conditions were used to adjust fluxes and deposition velocities for any minor remaining elevation from land. Ultimately, this resulted in a range of observed monthly median deposition velocities of 0.007 – 0.033 cm s^{-1}. This is of comparable spread to values of 0.009 – 0.034 cm s^{-1} reported by Helmig et al. (2012)[79] in a series of 5 cruises observing ozone deposition using eddy covariance. However, a key difference is that the measurements reported here are from a fixed

location, not at a wide range of latitudes as reported for the ship-borne measurements. The variation in deposition velocity reported here cannot be attributed to great differences in water temperature to the same extent the observations of Helmig et al.[79] can be. It is therefore surmised that local, seasonal variation in water composition, possibly linked to biological cycles in the coastal water, could be responsible for the variation in deposition velocities observed.

While flux observations grouped into months typically showed clear peaks and averages, the variation between individual averaging periods was considerable. The random error on these individual observations was examined in a number of ways. Defining a limit of detection based off the background noise during cross-covariance revealed that a majority (~70%) of accepted data exceeded the 1σ LoD, though a smaller number (~50%) exceeded the 2σ limit. This included data during the 2nd deployment averaged at 60 minutes; reducing the averaging time to that of the other deployments resulted in a reduction of observations exceeding the 1σ and 2σ LoDs to ~60% and ~30% respectively. Two other methods were used to estimate the random error present in the observations as a result of sampling error and instrument noise – one using integral turbulence timescales defined from the cross-correlation functions (used to determine lag), and the other parameterising them using the peak of a flux cospectrum. The former estimated random error to be ~110% of a typical observation, slightly above the 1σ LoDs (which also reflect the random error in observations, albeit quantified in a different way). The latter random error method values were 3-4 times higher, though this was not caused by the difference in how integral turbulence timescales were parameterised; integral turbulence timescales determined using flux cospectral peak were similar to those estimated from the integral of the cross-correlation peak. The difference stemmed from the use of simple standard deviations in the latter method, whereas the former used correlation coefficients which would limit the influence of random noise.

Autocovariance of the ozone data suggested that 45-98% of the variation in ozone mixing ratio could be attributed to white noise in the ozone instrument during the first deployment. The extent to which this could affect the overall error of a flux measurement was investigated by calculating LoDs using fake, normally distributed ozone data with a standard deviation matching the observed average. In the worst case (where almost all ozone variation is noise), the instrument noise was determined to contribute up to 67% of the observed random error in the flux. As such, a more sensitive, less noisy instrument could help to lower the uncertainty in individual observations. Since individual flux values showed high error, monthly medians were taken forward for comparisons to existing ozone deposition models.

5.3 Biogeochemistry at the PPAO

With the ozone deposition values discussed in chapter 2, chapter 3 covered the analysis of water samples around the PPAO and how the chemical species within the water that are reactive towards ozone could influence ozone deposition observations and model predictions. Samples of the sea-surface microlayer were collected by researchers at the Plymouth Marine Laboratory using a Garrett screen, with underlying water samples taken for comparison. After filtering, these were frozen and shipped to York for analysis of a variety of compounds and physical properties. The focus in this work was on the concentrations of iodide and of dissolved organic carbon, both understood to show reactivity with ozone. Iodide observations made near the PPAO, measured previously by the Carpenter research group using square wave voltammetry, were available dating back to 2016 (though only for underlying water). While samples gathered at the L4 site (~8 km south of the PPAO) showed little difference from samples within the flux footprint, SML samples consistently contained lower concentrations of iodide than the deeper water. The extent to which this reflects genuine depletion in the SML rather than the reaction of iodide on the surface of the Garrett screen before decanting is unclear, but since the ozone reacts well within the depth of the SML samples, SML values were decided to be most appropriate for predicting ozone reactivity. Over the course of a year, iodide concentrations were observed to rise sharply throughout the spring into early summer, peaking at ~100 nmol dm^{-3} in July before falling to ~50 nmol dm^{-3} during the winter. This increase coincided with a series of phytoplankton blooms that appear in the waters around the PPAO throughout spring, suggesting there could be a link to local biological production. Concentrations of DOC measured by oxidation and combustion to CO_2 showed the opposite trend; DOC was highest during the winter months, falling to a minimum in the summer. Measurements of total organic carbon (particulate as well as dissolved) were not available, and so while it is possible that more carbon had coalesced into the particulate phase, this hypothesis could not be confirmed.

General additive models were created using the iodide and DOC SML data to allow prediction of both at a time coinciding with accepted eddy covariance measurements of ozone deposition. This allowed for the comparison of observed deposition values with those determined from existing models for ozone deposition. Two models were considered. The 1-layer model of Fairall et al.[76] assumes that the importance of waterside turbulence increases linearly with depth from 0 at the water surface. Conversely, the 2-layer model of Luhar et al.[149] proposes the presence of a reaction-diffusion sublayer, extending to a depth of ~3 μm in which the effects of turbulence are negligible compared with those of molecular diffusion. Beneath this, the importance of turbulence scales linearly again as per the 1-layer model. Both models predict ozone deposition velocity based primarily on water temperature, friction velocity (closely related to wind speed), and chemical reactivity. The reactivity term has typically been defined by the concentration of iodide and its temperature-dependant rate

constant when reacting with ozone. Given the known reactivity of some organic compounds (such as unsaturated fatty acids) towards ozone, the importance of both species, as well as wind and temperature on both models were examined for the observations at the PPAO.

The 1-layer model consistently predicted higher deposition velocities than the 2-layer model; median predictions from the 1-layer model across the 3 deployments were 0.045 – 0.049 cm s^{-1} and 0.020 – 0.024 cm s^{-1} with and without DOC reactivity respectively, whereas the corresponding values for the 2-layer model were 0.037 – 0.039 cm s^{-1} and 0.015 – 0.018 cm s^{-1}. The 1-layer model also showed a markedly greater dependence on friction velocity than the 2-layer model resulting from the difference in treatment of waterside turbulence. A considerable correlation between friction velocity and deposition velocity is seen in several monthly observations, best represented by the 1-layer model. The inclusion of DOC reactivity in the models, using an estimated rate constant of 3.7×10^{-6} dm^3 mol^{-1} s^{-1}, lead to much greater model values, higher in all cases than was every observed by the measurements at the PPAO. This is likely due to the relatively high levels of DOC around the PPAO compared with typical ocean values, as well as huge uncertainty surrounding the rate constant used. Despite this, the models frequently predicted deposition velocities below observations, and while the magnitude of the predictions was off, some of the variation in observed deposition from month to month was reflected in the DOC-including models. It is therefore possible that reactivity in the surface water is influenced by both iodide and DOC, and the models examined here may diverge from observations in cases were DOC and iodide concentrations diverge from one another. The overestimation of the DOC-including models could also partly be caused by the simple additive treatment of the reactivities of different species, where previous work suggests they may partially inhibit one another[172]. Ultimately, many of the species that comprise DOC are likely to be largely unreactive to ozone, rendering a single rate constant a gross oversimplification. As such, an examination into the composition of the DOC at the PPAO was conducted to better understand its variability.

5.4 Dissolved Organic Material Compositional Analysis

Chapter 4 focused on the characterising the organic compounds present in the water samples and assessing the variation in bulk metrics and specific species over time and after exposure to high levels of ozone. The dissolved organic material was isolated from a number of surface and underlying water samples from around the PPAO via solid phase extraction for subsequent analysis using LCMS. By measuring precise masses of the compounds, molecular formulae could be assigned using the software MZmine. The peak areas of chromatograms could then be used to examine changes in

concentration, but only semi-quantitatively; different species could not be directly compared with one another due to differences in ionisation efficiency or retention by the solid phase during extraction.

A number of unfiltered samples were exposed to 500 ppbv of ozone for 20 hours in order to assess the effects of extreme ozone exposure and identify species that vary. It was expected that ozone would react with double bond containing compounds, and indeed the average double bond equivalence of samples decreased by 2-5% following exposure to ozone, depending on the weighting of peaks used. Fatty acids were examined in particular due to their documented reactivity with ozone, but none of a selection of compounds could readily be identified. Low sensitivity to fatty acids is a limitation of the SPE-DOM method, and such compounds are more typically observed after conversion into fatty acid methyl esters. While common reactants of ozonolysis were absent, a number of products were readily observed. A number of dicarboxylic acids which can form following the ozonolysis of an unsaturated fatty acid were consistently identified (unsaturated, from length C7 – C13), with bigger peaks after exposure to ozone compared with before.

The SML samples collected around the PPAO from 11/11/19 until 24/08/20 showed no clear seasonal change in DBE, though frequently yielded slightly lower DBE values than their corresponding ULW samples. This may indicate a loss of some large molecules with many double bonds from the surface water due to their reaction with ozone. While fatty acids again were largely undetected, the dicarboxylic acids identified in the ozonolysis experiments were ubiquitously present, with many showing a marked decrease over the course of the 30 samples. This agrees in part with the decreasing concentrations of DOC observed at the site over the same period. Decreases in suberic acid ($C_8H_{14}O_4$) and azelaic acid ($C_9H_{16}O_4$) from the start to the end of sampling were almost tenfold, though both species showed signs of potential contamination; sampling blanks in which artificial seawater was rinsed over the Garrett screen showed higher levels of both compounds compared with the underlying water. As dicarboxylic acids are commonly used as lubricants and plasticisers, it is possible that an amount of each was introduced into SML samples selectively due to the necessary use of a Garrett screen. However, pimelic acid ($C_7H_{12}O_4$), and sebacic acid ($C_{10}H_{18}O_4$) also showed modest decreases over time with no clear evidence of contamination, suggesting the decrease in these compounds to be at least partially genuine. Many organic compounds such as these are likely to be present in sea water for the same reason they are possibly introduced as contaminants – they are used widely in chemical industry and plastic manufacture, some waste of which is bound to end up in coastal water. Though every care was taken to check for introduction of compounds through the extraction and analysis procedures, the complete eradication of contaminants in nigh impossible and can only reasonably be minimised and accounted for.

5.5 Future Work

The work presented here covers the fieldwork at the PPAO up to and including May of 2021, though work is set to continue until October 2021. This has scope to fill in some gaps in data so far or provide year-to-year comparisons. Flux data from deployments 2 and 3 cover largely separate parts of the year, and the extension of deployment 3 allows for comparison between deployments alongside biogeochemical data. The timeseries of DOC has not yet been completed, and more data could reinforce or reverse the unexpected dip over the summer months.

In drawing comparisons between ozone deposition observations and models, the high uncertainty of the former is an obvious issue. Especially during deployment 2, low instrument sensitivity made for noisy flux data, and while this could be countered in part by longer averaging periods, this in turn leads to greater risk of non-stationarity and the discarding of data from an already limited wind sector. One possible alternative would be employing wavelet analysis for the calculation of fluxes, rather than the 'classical' eddy covariance method. This involves convolution of scalar and wind data with a wavelet function at a range of different time and frequency intervals and could offer more frequent flux observations while still adequately accounting for the full range of eddy scales within the atmosphere. An improvement in instrumentation could also serve to reduce the problem of large flux uncertainties encountered in this work. While chemiluminescence-based instruments have been widely used, more sensitive mass spectroscopy[139] and cavity enhanced UV[198] techniques have been recently developed that can achieve the high frequency resolution necessary for eddy covariance. Additionally, by not relying on the formation of excited state NO_2, the issue of quenching by water vapour can be avoided (though interference can still be an issue in UV-based detectors).

With respect to the prediction of ozone deposition with models, the reactivity term is a clear source of uncertainty. While the rate constant for the iodide-ozone reaction is better characterised than that of DOC, there are still few observations, and indeed the evidence for its dependence on temperature is far from certain. As such, more studies of the kinetics of this interaction could help improve predictive oceanic ozone models. This could take the form of measuring ozone loss as known ozone is passed across a controlled water sample containing iodide. This could be expanded to study DOC reactivity too, and the interactions between the two. In general, this approach of observing a simplified system could be beneficial in separating the complex factors at play in the field measurements. Beyond the chemical reactivity, there are questions surrounding the importance of wind induced waterside turbulence. Experiments within chambers would allow for this element to be isolated. To study higher wind speed conditions, a wave chamber could be an option. There may also be value in revisiting the physical effects in the absence of chemical ones by observing exchange of species with little or no chemical reactivity in seawater.

As mentioned, the application of a single rate constant to a collection of compounds such as DOC is a large oversimplification. It does however provide at least some indication of reactivity, and the variation of DOC reactivity in different oceanic conditions could prove important. Besides the measurements discussed in this work, many more samples from the PPAO have been collected to assess the presence of nutrient species, surfactant activity, surface tension and more with a view better understand their potential effects of ozone deposition.

Given the shallow depth at which the reactions of ozone with iodide and DOC occur, accurate measurements of chemical concentrations in the very surface of the SML are important to understand the rate of ozone loss. Garrett screens have been used for SML collection in this work due to the large volumes required for analyses, but the depth of SML collected is estimated to be far greater than that over which the ozone reactions occur. Furthermore, the possibility for reactive species to be lost while the sample is drained from the screen could bias SML samples compared with underlying water. This could be tested using a control solution and varying the duration of air exposure to see if iodide or organic compounds were lost at longer exposure times. Collection techniques using glass screens have generally yielded smaller volumes of shallower SML – automation of this sampling process (with a remote-controlled unit with rolling sampling drums for instance) could be an option to combine the collection volume of the Garrett screens with the shallow sample depth of screen techniques.

This work has focused solely on observations from a single, coastal site. This inevitably will be an imperfect representation of open ocean conditions that will be relevant for global modelling. The headland on which observations were conducted will have affected wind speeds, and excluding terrestrial flux via footprint models is an imperfect solution to the problem of land influence. Ideal land-based observations would have to be conducted from a pier or similar feature reaching far out away from the land with minimal distortion of the wind, thought the presence of some structure is a practical necessity for housing equipment. Even in this case, the issues of a single fixed observation point and coastal waters remain. Coastal waters are likely to be high in nutrients, especially in upwelling waters, and therefore iodide and organics are likely to differ from open ocean conditions. However, if the reactivity of the water is different, this ought to be reflected in the ozone flux observations, and provide information on higher iodide and organic values that may be less common elsewhere.

Ultimately, better global prediction of ozone deposition will be helped by greater spatial information on iodide, doc, and ozone flux. The difficulty in obtaining clear oceanic fluxes from a land-based station and their restriction to coastal waters makes it unlikely that they can provide a complete picture alone. As such, measurements on moving platforms, such as ships or aircraft, present an excellent option to observe open ocean fluxes across a greater range of locations. Ship-based work would additionally present a convenient opportunity for remote SML collection to enable the kind of

comparisons conducted in this work. While this would not be an option for airborne measurements, the spatial coverage of such work would be far greater for the time required. The instrumentation requirements of such work may be more demanding however in order to calculate fluxes in motion.

Lastly, the SPE-DOM analysis remains a work in progress, with more samples yet to be analysed and the methodology itself still improving. While dicarboxylic acids have been identified as detectable ozonolysis products in the SML, more may yet come to light with continued interrogation of the thousands of identifiable features present. A strategy of identifying reactive compounds from ozone exposure experiments would allow for certain species or types of compounds to be selected for more rigorous analysis. Quantitative methods for compounds of interest could then be developed using LCMS, and their variation over time assessed. It may also be that relatively few species contribute a large portion of the total reactivity of DOC, in which case greater efforts to characterise these reactions could better define the overall ozone-DOC reaction. However, as is made apparent by the lack of fatty acids detected in this work, a complete picture of DOC reactivity cannot be obtained from this method alone. Alternative extraction methods to SPE may retain different portions of the DOC. As is the case for fatty acids, alternative detection methods (such as GCMS) could be pursued in cases where detection by LCMS is poor, but reactivity is expected based on chemical structure.

Abbreviations

α	Dimensionless solubility of ozone in water
δ_m	Reaction-diffusion sublayer
κ	Von Kármán constant
ρ_a	Density of air
ρ_w	Density of water
τ_{wca}	Integral turbulence timescale
a	Total reactivity of ozone to species in water
AI	Aromaticity Index
AQD	Air Quality Designs ozone instrument
BODC	British Oceanographic Data Centre
CCF	Cross-correlation function
CIMS	Chemical ionisation mass spectrometry
CLD86	Chemiluminescence detector ozone instrument
D	Diffusivity of ozone in water
DBE	Double bond equivalence
DOC	Dissolved organic carbon
DOM	Dissolved organic material
EC	Eddy covariance
ESI	Electrospray ionisation
FA	Fatty acid
GAM	General additive model
GCMS	Gas chromatography-mass spectrometry
I^-	Iodide

IO_3^-	Iodate
IQR	Interquartile range
ITS	Integral turbulence timescale
k_a	Transport rate (airside)
K_t	Turbulent diffusivity in water
k_w	Transport rate (waterside)
L	Obukhov length
L4	Sampling Buoy 8 km south of the PPAO
LCMS	Liquid chromatography-mass spectrometry
l_m	Reaction diffusion length scale
LoD	Limit of detection
LPDM-B	Lagrangian stochastic particle dispersion footprint model
MFC	Mass flow controller
m/z	Mass units divided by charge
NEON	National Ecological Observatory Network
NO	Nitric oxide
NO_2	Nitrogen dioxide
NO_x	$NO + NO_2$
O_3	Ozone
PMT	Photo-multiplier tube
PPAO	Penlee Point Atmospheric Observatory
PUFA	Polyunsaturated fatty acid
R_a	Atmospheric resistance
rAI	Restrictive aromaticity index
rAI_{mod}	Modified restrictive aromaticity index

R_b	Quasi-laminar layer resistance
R_c	Surface resistance
RE	Relative error
RF	Radiative forcing
RMSE	Root-mean-square error
RT	Retention time
Sc	Schmidt number
SML	Sea surface microlayer
SPE	Solid phase extraction
SPE-DOM	Solid phase extracted dissolved organic material
SST	Sea surface temperature
STE	Stratosphere-troposphere exchange
TOC	Total organic carbon
U	Wind speed
u_*	Friction velocity
u_{*w}	Waterside friction velocity
ULW	Underlying water
v_d	Deposition velocity
v_{dw}	Waterside deposition velocity
VOC	Volatile organic compound
z	Measurement height/depth
z_0	Roughness length
z/L	Dimensionless Obukhov stability parameter

Bibliography

1. Loades, D. C. *et al.* Ozone deposition to a coastal sea: Comparison of eddy covariance observations with reactive air-sea exchange models. *Atmos. Meas. Tech.* **13**, 6915–6931 (2020).

2. Guarnieri, M. & Balmes, J. R. Outdoor air pollution and asthma. *Lancet* **383**, 1581–1592 (2014).

3. Bălă, G. P., Râjnoveanu, R. M., Tudorache, E., Motișan, R. & Oancea, C. Air pollution exposure—the (in)visible risk factor for respiratory diseases. *Environ. Sci. Pollut. Res.* (2021) doi:10.1007/s11356-021-13208-x.

4. Nassikas, N. *et al.* Ozone-related asthma emergency department visits in the US in a warming climate. *Environ. Res.* **183**, 1–7 (2020).

5. Zheng, X. Y. *et al.* Association between Air pollutants and asthma emergency room visits and hospital admissions in time series studies: A systematic review and meta-Analysis. *PLoS One* **10**, (2015).

6. Strickland, M. J. *et al.* Short-term associations between ambient air pollutants and pediatric asthma emergency department visits. *Am. J. Respir. Crit. Care Med.* **182**, 307–316 (2010).

7. Johannson, K. A. *et al.* Air Pollution Exposure Is Associated With Lower Lung Function, but Not Changes in Lung Function, in Patients With Idiopathic Pulmonary Fibrosis. *Chest* **154**, 119–125 (2018).

8. Medina-Ramón, M., Zanobetti, A. & Schwartz, J. The effect of ozone and PM10 on hospital admissions for pneumonia and chronic obstructive pulmonary disease: A national multicity study. *Am. J. Epidemiol.* **163**, 579–588 (2006).

9. Bernardini, F. *et al.* Air pollutants and daily number of admissions to psychiatric emergency services: evidence for detrimental mental health effects of ozone. *Epidemiol. Psychiatr. Sci.* **29**, e66 (2019).

10. Organisation, W. H. *WHO Air quality guidelines for particulate matter, ozone, nitrogen dioxide and sulfur dioxide : global update 2005 : summary of risk assessment*. *WHO Press* (2006).

11. Lamarque, J. F. *et al.* Tropospheric ozone evolution between 1890 and 1990. *J. Geophys. Res. D Atmos.* **110**, 1–15 (2005).

12. Tripathi, O. P. *et al.* An assessment of the surface ozone trend in Ireland relevant to air pollution and environmental protection. *Atmos. Pollut. Res.* **3**, 341–351 (2012).

13. Chiquetto, J. B. *et al.* Air quality standards and extreme ozone events in the São Paulo megacity. *Sustain.* **11**, 1–14 (2019).

14. Roy, S. D., Beig, G. & Ghude, S. D. Exposure-plant response of ambient ozone over the tropical Indian region. *Atmos. Chem. Phys.* **9**, 5253–5260 (2009).

15. Godowitch, J. M., Gilliland, A. B., Draxler, R. R. & Rao, S. T. Modeling assessment of point source NOx emission reductions on ozone air quality in the eastern United States. *Atmos. Environ.* **42**, 87–100 (2008).

16. Dentener, F. *et al.* The impact of air pollutant and methane emission controls on tropospheric ozone and radiative forcing: CTM calculations for the period 1990-2030. *Atmos. Chem. Phys.* **5**, 1731–1755 (2005).

17. Fiore, A. M., West, J. J., Horowitz, L. W., Naik, V. & Schwarzkopf, M. D. Characterizing the tropospheric ozone response to methane emission controls and the benefits to climate and air quality. *J. Geophys. Res. Atmos.* **113**, 1–16 (2008).

18. Yadav, A. *et al.* Growth, yield and quality of maize under ozone and carbon dioxide interaction in North West India. *Aerosol Air Qual. Res.* **21**, 1–14 (2021).

19. Peng, J., Xu, Y., Shang, B., Agathokleous, E. & Feng, Z. Effects of elevated ozone on maize under varying soil nitrogen levels: Biomass, nitrogen and carbon, and their allocation to kernel. *Sci. Total Environ.* **765**, 144332 (2021).

20. Wang, X., Manning, W., Feng, Z. & Zhu, Y. Ground-level ozone in China: Distribution and effects on crop yields. *Environ. Pollut.* **147**, 394–400 (2007).

21. Schauberger, B., Rolinski, S., Schaphoff, S. & Müller, C. Global historical soybean and wheat yield loss estimates from ozone pollution considering water and temperature as modifying effects. *Agric. For. Meteorol.* **265**, 1–15 (2019).

22. Amin, N. Effect of ozone on the relative yield of rice crop in japan evaluated based on monitored concentrations. *Water. Air. Soil Pollut.* **225**, (2014).

23. Van Dingenen, R. *et al.* The global impact of ozone on agricultural crop yields under current and future air quality legislation. *Atmos. Environ.* **43**, 604–618 (2009).

24. Vlasáková-Matoušková, L. & Hůnová, I. Stomatal ozone flux and visible leaf injury in native juvenile trees of Fagus sylvatica L.: a field study from the Jizerske hory Mts., the Czech Republic. *Environ. Sci. Pollut. Res.* **22**, 10034–10046 (2015).

25. Fuhrer, J. *et al.* Current and future ozone risks to global terrestrial biodiversity and ecosystem processes. *Ecol. Evol.* **6**, 8785–8799 (2016).

26. Checa-Garcia, R., Hegglin, M. I., Kinnison, D., Plummer, D. A. & Shine, K. P. Historical Tropospheric and Stratospheric Ozone Radiative Forcing Using the CMIP6 Database. *Geophys. Res. Lett.* **45**, 3264–3273 (2018).

27. Conley, A. J., Lamarque, J. F., Vitt, F., Collins, W. D. & Kiehl, J. PORT, a CESM tool for the diagnosis of radiative forcing. *Geosci. Model Dev.* **6**, 469–476 (2013).

28. Lamarque, J. F. *et al.* The atmospheric chemistry and climate model intercomparison Project (ACCMIP): Overview and description of models, simulations and climate diagnostics. *Geosci. Model Dev.* **6**, 179–206 (2013).

29. Stevenson, D. S. *et al.* Tropospheric ozone changes, radiative forcing and attribution to emissions in the Atmospheric Chemistry and Climate Model Intercomparison Project (ACCMIP). *Atmos. Chem. Phys.* **13**, 3063–3085 (2013).

30. Shindell, D. *et al.* Attribution of historical ozone forcing to anthropogenic emissions. *Nat. Clim. Chang.* **3**, 567–570 (2013).

31. Skeie, R. B. *et al.* Anthropogenic radiative forcing time series from pre-industrial times until 2010. *Atmos. Chem. Phys.* **11**, 11827–11857 (2011).

32. Søvde, O. A., Hoyle, C. R., Myhre, G. & Isaksen, I. S. A. The HNO3 forming branch of the HO2 + NO reaction: Pre-industrial-to-present trends in atmospheric species and radiative forcings. *Atmos. Chem. Phys.* **11**, 8929–8943 (2011).

33. Myhre, G. *et al.* Anthropogenic and natural radiative forcing. in *Climate Change 2013 the Physical Science Basis: Working Group I Contribution to the Fifth Assessment Report of the Intergovernmental Panel on Climate Change* vol. 9781107057 659–740 (Cambridge University Press, 2013).

34. Jacob, D. J. *Introduction to Atmospheric Chemistry*. (Princeton University Press, 1999).

35. Stevenson, D. S. *et al.* Multimodel ensemble simulations of present-day and near-future tropospheric ozone. *J. Geophys. Res. Atmos.* **111**, (2006).

36. Lelieveld, J. & Dentener, F. J. What controls tropospheric ozone? *J. Geophys. Res.* **105**, 3531 (2000).

37. Bey, I. *et al.* Global Modeling of Tropospheric Chemistry with Assimilated Meteorology: Model Description and Evaluation. *J. Geophys. Res.* **106**, 73–95 (2001).

38. Sudo, K., Takahashi, M., Kurokawa, J. I. & Akimoto, H. CHASER: A global chemical model of the troposphere 1. Model description. *J. Geophys. Res. Atmos.* **107**, (2002).

39. Horowitz, L. W. A global simulation of tropospheric ozone and related tracers: Description and evaluation of MOZART, version 2. *J. Geophys. Res.* **108**, 4784-- (2003).

40. von Kuhlmann, R., Lawrence, M. G., Crutzen, P. J. & Rasch, P. J. A model for studies of tropospheric ozone and nonmethane hydrocarbons: Model description and ozone results. *J. Geophys. Res.* **108**, 4294, doi:10.1029/2002JD002893 (2003).

41. Shindell, D. T., Faluvegi, G. & Bell, N. Preindustrial-to-present-day radiative forcing by tropospheric ozone from improved simulations with the GISS chemistry-climate GCM. *Atmos. Chem. Phys.* **3**, 1675–1702 (2003).

42. Park, R. J., Pickering, K. E., Allen, D. J., Stenchikov, G. L. & Fox-Rabinovitz, M. S. Global simulation of tropospheric ozone using the University of Maryland Chemical Transport Model (UMD-CTM): 1. Model description and evaluation. *J. Geophys. Res. D Atmos.* **109**, 1–27 (2004).

43. Rotman, D. A. *et al.* IMPACT, the LLNL 3-D global atmospheric chemical transport model for the combined troposphere and stratosphere: Model description and analysis of ozone and other trace gases. *J. Geophys. Res. Atmos.* **109**, n/a-n/a (2004).

44. Wong, S., Wang, W. C., Isaksen, I. S. A., Berntsen, T. K. & Sundet, J. K. A global climate-chemistry model study of present-day tropospheric chemistry and radiative forcing from changes in tropospheric O3 since the preindustrial period. *J. Geophys. Res. D Atmos.* **109**, (2004).

45. Stevenson, D. S. *et al.* Radiative forcing from aircraft NOx emissions: Mechanisms and seasonal dependence. *J. Geophys. Res. D Atmos.* **109**, (2004).

46. Wild, O. *et al.* Chemical transport model ozone simulations for spring 2001 over the western Pacific: Regional ozone production and its global impacts. *J. Geophys. Res. D Atmos.* **109**, 1–16 (2004).

47. Folberth, G. A., Hauglustaine, D. A., Lathière, J. & Brocheton, F. Interactive chemistry in the Laboratoire de Météorologie Dynamique general circulation model: model description and impact analysis of biogenic hydrocarbons on tropospheric chemistry. *Atmos. Chem. Phys.* **6**, 2273–2319 (2006).

48. Stevenson, D. S. *et al.* Multimodel ensemble simulations of present-day and near-future tropospheric ozone. *J. Geophys. Res. Atmos.* **111**, (2006).

49. Huijnen, V. *et al.* The global chemistry transport model TM5: Description and evaluation of the tropospheric chemistry version 3.0. *Geosci. Model Dev.* **3**, 445–473 (2010).

50. Kawase, H., Nagashima, T., Sudo, K. & Nozawa, T. Future changes in tropospheric ozone under Representative Concentration Pathways (RCPs). *Geophys. Res. Lett.* **38**, 1–6 (2011).

51. Young, P. J. *et al.* Pre-industrial to end 21st century projections of tropospheric ozone from the Atmospheric Chemistry and Climate Model Intercomparison Project (ACCMIP). *Atmos. Chem. Phys.* **13**, 2063–2090 (2013).

52. Hu, L. *et al.* Global budget of tropospheric ozone: Evaluating recent model advances with satellite (OMI), aircraft (IAGOS), and ozonesonde observations. *Atmos. Environ.* **167**, 323–334 (2017).

53. Badia, A. *et al.* The Role of Natural Halogens in Global Tropospheric Ozone Chemistry and Budget Under Different 21st Century Climate Scenarios. *J. Geophys. Res. Atmos.* **126**, 1–25 (2021).

54. Griffiths, P. *et al.* Tropospheric ozone in CMIP6 Simulations. *Atmos. Chem. Phys.* 1–50 (2021) doi:10.5194/acp-2019-1216.

55. Yang, H., Chen, G., Tang, Q. & Hess, P. Quantifying isentropic stratosphere-troposphere exchange of ozone. *J. Geophys. Res.* **121**, 3372–3387 (2016).

56. Stohl, A. *et al.* Stratosphere-troposphere exchange: A review, and what we have learned from STACCATO. *J. Geophys. Res. Atmos.* **108**, (2003).

57. Holton, J. R. *et al.* Stratosphere-troposphere exchange. *Rev. Geophys.* **33**, 403–439 (1995).

58. Appenzeller, C. & Davies, H. C. Structure of stratospheric intrusions into the troposphere. *Nature* **358**, 570–572 (1992).

59. Forster, C. & Wirth, V. Radiative decay of idealized stratospheric filaments in the troposphere. *J. Geophys. Res. Atmos.* **105**, 10169–10184 (2000).

60. Wesely, M. L. & Hicks, B. B. A review of the current status of knowledge on dry deposition. *Atmos. Environ.* **34**, 2261–2282 (2000).

61. Emerson, E. W. *et al.* Revisiting particle dry deposition and its role in radiative effect estimates. *Proc. Natl. Acad. Sci. U. S. A.* **117**, 26076–26082 (2020).

62. Hardacre, C., Wild, O. & Emberson, L. An evaluation of ozone dry deposition in global scale chemistry climate models. *Atmos. Chem. Phys.* **15**, 6419–6436 (2015).

63. Fowler, D., Flechard, C., Cape, J. N., Storeton-West, R. & Coyle, M. Measurements of Ozone

Deposition to Vegetation Quantifying the Flux, the Stomatal and Non-Stomatal Components. *Water, Air, Soil Pollut.* **130**, 63–74 (2001).

64. Hogg, A. *et al.* Stomatal and non-stomatal fluxes of ozone to a northern mixed hardwood forest. *Tellus, Ser. B Chem. Phys. Meteorol.* **59**, 514–525 (2007).

65. Coyle, M., Nemitz, E., Storeton-West, R., Fowler, D. & Cape, J. N. Measurements of ozone deposition to a potato canopy. *Agric. For. Meteorol.* **149**, 655–666 (2009).

66. Turner, N. C., Waggoner, P. E. & Rich, S. Removal of ozone from the atmosphere by soil and vegetation. *Nature* **250**, 486–489 (1974).

67. Massman, W. J. Toward an ozone standard to protect vegetation based on effective dose: A review of deposition resistances and a possible metric. *Atmos. Environ.* **38**, 2323–2337 (2004).

68. Lenschow, D. H., Pearson, R. & Stankov, B. B. Measurements of ozone vertical flux to ocean and forest. *J. Geophys. Res. Ocean.* **87**, 8833–8837 (1982).

69. Chang, W., Heikes, B. G. & Lee, M. Ozone deposition to the sea surface: Chemical enhancement and wind speed dependence. *Atmos. Environ.* **38**, 1053–1059 (2004).

70. Garland, J. A., Elzerman, A. W., Penkett, A. A. The mechanism for dry deposition of ozone to seawater surface. *J. Geophys. Res.* **85**, 7488–7492 (1980).

71. Hu, J. H. *et al.* Reactive uptake of Cl2(g) and Br2(g) by aqueous surfaces as a function of Br- and I- ion concentration. The effect of chemical reaction at the interface. *J. Phys. Chem.* **99**, 8768–8776 (1995).

72. Magi, L. *et al.* Investigation of the Uptake Rate of Ozone and Methyl Hydroperoxide by Water Surfaces. *J. Phys. Chem. A* **101**, 4943–4949 (1997).

73. Liu, Q. *et al.* Kinetics and mechanisms of aqueous ozone reactions with bromide, sulfite, hydrogen sulfite, iodide, and nitrite ions. *Inorg. Chem.* **40**, 4436–4442 (2001).

74. Sarwar, G. *et al.* Technical note: Examining ozone deposition over seawater. *Atmos. Environ.* **141**, 255–262 (2016).

75. McKay, W. A., Stephens, B. A. & Dollard, G. J. Laboratory measurements of ozone deposition to sea water and other saline solutions. *Atmos. Environ. Part A, Gen. Top.* **26**, 3105–3110 (1992).

76. Fairall, C. W., Hare, J. E., Helmig, D. & Ganzveld, L. Water-side turbulence enhancement of ozone deposition to the ocean. in *86th AMS Annual Meeting* 443–451 (2007). doi:10.5194/acpd-6-5137-2006.

77. Gallagher, M. W., Beswick, K. M. & Coe, H. Ozone deposition to coastal waters. *Q. J. R. Meteorol. Soc.* **127**, 539–558 (2001).

78. Wanninkhof, R. Relationship Between Wind Speed and Gas Exchange. *J. Geophys. Res.* **97**, 7373–7382 (1992).

79. Helmig, D. *et al.* Atmosphere-ocean ozone fluxes during the TexAQS 2006, STRATUS 2006, GOMECC 2007, GasEx 2008, and AMMA 2008 cruises. *J. Geophys. Res. Atmos.* **117**, 1–15 (2012).

80. von Kuhlmann, R., Lawrence, M. G., Crutzen, P. J. & Rasch, P. J. A model for studies of tropospheric ozone and nonmethane hydrocarbons: Model description and ozone results. *J. Geophys. Res. Atmos.* **108**, (2003).

81. Kerkweg, A. *et al.* Technical Note: An implementation of the dry removal processes DRY DEPosition and SEDImentation in the Modular Earth Submodel System (MESSy). *Atmos. Chem. Phys.* **6**, 4617–4632 (2006).

82. Emmons, L. K. *et al.* Description and evaluation of the Model for Ozone and Related chemical Tracers, version 4 (MOZART-4). *Geosci. Model Dev.* **3**, 43–67 (2010).

83. Lamarque, J. F. *et al.* CAM-chem: Description and evaluation of interactive atmospheric chemistry in the Community Earth System Model. *Geosci. Model Dev.* **5**, 369–411 (2012).

84. Mao, J. *et al.* Ozone and organic nitrates over the eastern United States: Sensitivity to isoprene chemistry. *J. Geophys. Res. Atmos.* **118**, 11,256-11,268 (2013).

85. Macdonald, S. M. *et al.* A laboratory characterisation of inorganic iodine emissions from the sea surface: Dependence on oceanic variables and parameterisation for global modelling. *Atmos. Chem. Phys.* **14**, 5841–5852 (2014).

86. Carpenter, L. J. *et al.* Atmospheric iodine levels influenced by sea surface emissions of inorganic iodine. *Nat. Geosci.* **6**, 108–111 (2013).

87. Tinel, L. *et al.* Influence of the Sea Surface Microlayer on Oceanic Iodine Emissions. *Environ. Sci. Technol.* **54**, 13228–13237 (2020).

88. Wadley, M. R. *et al.* A Global Model for Iodine Speciation in the Upper Ocean. *Global Biogeochem. Cycles* **34**, (2020).

89. Sherwen, T. M. *et al.* Global modeling of tropospheric iodine aerosol. *Geophys. Res. Lett.* **43**, 10012–10019 (2016).

90. Sipilä, M. *et al.* Molecular-scale evidence of aerosol particle formation via sequential addition

of HIO3. *Nature* **537**, 532–534 (2016).

91. Gómez Martín, J. C. *et al.* A gas-to-particle conversion mechanism helps to explain atmospheric particle formation through clustering of iodine oxides. *Nat. Commun.* **11**, 1–14 (2020).

92. Koenig, T. K. *et al.* Quantitative detection of iodine in the stratosphere. *Proc. Natl. Acad. Sci. U. S. A.* **117**, 1860–1866 (2020).

93. Sherwen, T. *et al.* Global impacts of tropospheric halogens (Cl, Br, I) on oxidants and composition in GEOS-Chem. *Atmos. Chem. Phys.* **16**, 12239–12271 (2016).

94. Sherwen, T. *et al.* Effects of halogens on European air-quality. *Faraday Discuss.* **200**, 75–100 (2017).

95. Read, K. A. *et al.* Extensive halogen-mediated ozone destruction over the tropical Atlantic Ocean. *Nature* **453**, 1232–1235 (2008).

96. Prados-Roman, C. *et al.* A negative feedback between anthropogenic ozone pollution and enhanced ocean emissions of iodine. *Atmos. Chem. Phys.* **15**, 2215–2224 (2015).

97. Shaw, M. D. & Carpenter, L. J. Modification of ozone deposition and I2 emissions at the air-aqueous interface by dissolved organic carbon of marine origin. *Environ. Sci. Technol.* **47**, 10947–10954 (2013).

98. Reeser, D. I. & Donaldson, D. J. Influence of water surface properties on the heterogeneous reaction between O3(g) and I(aq)-. *Atmos. Environ.* **45**, 6116–6120 (2011).

99. Hayase, S. *et al.* Heterogeneous reaction of gaseous ozone with aqueous iodide in the presence of aqueous organic species. *J. Phys. Chem. A* **114**, 6016–6021 (2010).

100. Hayase, S. *et al.* Weak acids enhance halogen activation on atmospheric waters surfaces. *J. Phys. Chem. A* **115**, 4935–4940 (2011).

101. Rossignol, S. *et al.* Atmospheric photochemistry at a fatty acid–coated air-water interface. *Science (80-.).* **353**, 699–702 (2016).

102. Zhou, S. *et al.* Formation of gas-phase carbonyls from heterogeneous oxidation of polyunsaturated fatty acids at the air-water interface and of the sea surface microlayer. *Atmos. Chem. Phys.* **14**, 1371–1384 (2014).

103. Zhang, Z., Liu, L., Liu, C. & Cai, W. Studies on the sea surface microlayer: II. The layer of sudden change of physical and chemical properties. *J. Colloid Interface Sci.* **264**, 148–159 (2003).

104. Hühnerfuss, H. Basic physicochemical principles of monomolecular sea slicks and crude oil spills. in *Marine Surface Films: Chemical Characteristics, Influence on Air-Sea Interactions and Remote Sensing* (eds. Gade, M., Hühnerfuss, H. & Korenowski, G. M.) 21–35 (Springer Berlin Heidelberg, 2006). doi:10.1007/3-540-33271-5_4.

105. Salter, M. E. *et al.* Impact of an artificial surfactant release on air-sea gas fluxes during Deep Ocean Gas Exchange Experiment II. *J. Geophys. Res. Ocean.* **116**, 1–9 (2011).

106. Broecker, H. C., Petermann, J. & Siems, W. Influence of wind on CO2-exchange in a wind-wave tunnel, including effects of monolayers. *J. Mar. Res.* **36**, 595–610 (1978).

107. Carlson, D. J. Dissolved organic materials in surface microlayers: Temporal and spatial variability and relation to sea state. *Limnol. Oceanogr.* **28**, 415–431 (1983).

108. Kuznetsova, M., Lee, C., Aller, J. & Frew, N. Enrichment of amino acids in the sea surface microlayer at coastal and open ocean sites in the North Atlantic Ocean. *Limnol. Oceanogr.* **49**, 1605–1619 (2004).

109. Reinthaler, T., Sintes, E. & Herndl, G. J. Dissolved organic matter and bacterial production and respiration in the sea-surface microlayer of the open Atlantic and the western Mediterranean Sea. *Limnol. Oceanogr.* **53**, 122–136 (2008).

110. Upstill-Goddard, R. C. Air-sea gas exchange in the coastal zone. *Estuar. Coast. Shelf Sci.* **70**, 388–404 (2006).

111. Liss, P. S. & Slater, P. G. Flux of Gases across the Air-Sea Interface. *Nature* **247**, 181–184 (1974).

112. McGillis, W. R., Dacey, J. W. H., Frew, N. M., Bock, E. J. & Nelson, R. K. Water-air flux of dimethylsulfide. *J. Geophys. Res. Ocean.* **105**, 1187–1193 (2000).

113. Cunliffe, M. *et al.* Sea surface microlayers: A unified physicochemical and biological perspective of the air-ocean interface. *Prog. Oceanogr.* **109**, 104–116 (2013).

114. Clifford, D., Donaldson, D. J., Brigante, M., D'Anna, B. & George, C. Reactive uptake of ozone by chlorophyll at aqueous surfaces. *Environ. Sci. Technol.* **42**, 1138–1143 (2008).

115. Moise, T. & Rudich, Y. Reactive uptake of ozone by aerosol-associated unsaturated fatty acids: Kinetics, mechanism, and products. *J. Phys. Chem. A* **106**, 6469–6476 (2002).

116. He, X., Leng, C., Pang, S. & Zhang, Y. Kinetics study of heterogeneous reactions of ozone with unsaturated fatty acid single droplets using micro-FTIR spectroscopy. *RSC Adv.* **7**, 3204–3213 (2017).

117. Thornberry, T. & Abbatt, J. P. D. Heterogeneous reaction of ozone with liquid unsaturated fatty acids: Detailed kinetics and gas-phase product studies. *Phys. Chem. Chem. Phys.* **6**, 84–93 (2004).

118. Elderfield, H. & Truesdale, V. W. On the biophilic nature of iodine in seawater. *Earth Planet. Sci. Lett.* **50**, 105–114 (1980).

119. Truesdale, V. W., Bale, A. J. & Woodward, E. M. S. The meridional distribution of dissolved iodine in near-surface waters of the Atlantic Ocean. *Prog. Oceanogr.* **45**, 387–400 (2000).

120. Wong, G. T. . The marine geochemistry of iodine. *Rev. Aquat. Sci.* **4**, 45–73 (1991).

121. Wong, G. T. . & Brewer, P. G. The marine chemistry of iodine in anoxic basins. *Geochim. Cosmochim. Acta* **41**, 151–159 (1977).

122. Chance, R., Baker, A. R., Carpenter, L. & Jickells, T. D. The distribution of iodide at the sea surface. *Environ. Sci. Process. Impacts* **16**, 1841–1859 (2014).

123. Wong, G. T. F. & Brewer, P. G. Determination and distribution of iodate in south-Atlantic waters. *J. Mar. Res.* **32**, 25–36 (1974).

124. Huang, Z. *et al.* Sensitive monitoring of iodine species in sea water using capillary electrophoresis: vertical profiles of dissolved iodine in the Pacific Ocean. *J. Environ. Monit.* **7**, 804–8 (2005).

125. Ganzeveld, L., Helmig, D., Fairall, C. W., Hare, J. & Pozzer, A. Atmosphere-ocean ozone exchange: A global modeling study of biogeochemical, atmospheric, and waterside turbulence dependencies. *Global Biogeochem. Cycles* **23**, 1–16 (2009).

126. Chapman, P. & Liss, P. S. The sea surface microlayer : Measurements of dissolved iodine bound and particulate species and nutrients in coastal waters. **26**, 387–390 (1981).

127. Truesdale, V. W. & Upstill-Goddard, R. Dissolved iodate and total iodine along the British east coast. *Estuar. Coast. Shelf Sci.* **56**, 261–270 (2003).

128. Wong, G. T. F. & Zhang, L. S. Geochemical dynamics of iodine in marginal seas: The southern East China Sea. *Deep. Res. Part II Top. Stud. Oceanogr.* **50**, 1147–1162 (2003).

129. Wong, G. T. F., Hung, C. C. & Gong, G. C. Dissolved iodine species in the East China Sea - A complementary tracer for upwelling water on the shelf. *Cont. Shelf Res.* **24**, 1465–1484 (2004).

130. Aldaz, L. Flux Measurements of Atmospheric Ozone Over Land Water. *J. Geophys. Res.* **74**, 6943–6946 (1969).

131. Galbally, I. E. & Roy, C. R. Destruction of ozone at the earth's surface. *Q. J. R. Meteorol. Soc.*

106, 599–620 (1980).

132. Tiefenau, H. & Fabian, P. The Specific Ozone Destruction at the Ocean Surface. **412**, 399–412 (1972).

133. Garland, J. A. & Penkett, S. A. Absorption of peroxy acetyl nitrate and ozone by natural surfaces. *Atmos. Environ.* **10**, 1127–1131 (1976).

134. Wesely, M. L., Cook, D. R. & Williams, R. M. Field measurement of small ozone fluxes to snow, wet bare soil, and lake water. *Bound. Layer Meteorol.* **20**, 459–471 (1981).

135. Kawa, S. R. & Pearson, R. Ozone budgets from the dynamics and chemistry of marine stratocumulus experiment. *J. Geophys. Res.* **94**, 9809 (1989).

136. Heikes, B. *et al.* Ozone, hydroperoxides, oxides of nitrogen, and hydrocarbon budgets in the marine boundary layer over the South Atlantic. *J. Geophys. Res.* **101**, 24221 (1996).

137. Whitehead, J. D., Mcfiggans, G. B., Gallagher, M. W. & Flynn, M. J. Direct linkage between tidally driven coastal ozone deposition fluxes, particle emission fluxes, and subsequent CCN formation. *Geophys. Res. Lett.* **36**, 1–5 (2009).

138. McVeigh, P., O'Dowd, C. & Berresheim, H. Eddy Correlation Measurements of Ozone Fluxes over Coastal Waters West of Ireland. *Adv. Meteorol.* **2010**, 1–7 (2010).

139. Novak, G. A., Vermeuel, M. P. & Bertram, T. H. Simultaneous detection of ozone and nitrogen dioxide by oxygen anion chemical ionization mass spectrometry: a fast-time-response sensor suitable for eddy covariance measurements. *Atmos. Meas. Tech.* **13**, 1887–1907 (2020).

140. Bariteau, L. *et al.* Determination of oceanic ozone deposition by ship-borne eddy covariance flux measurements. *Atmos. Meas. Tech.* **3**, 441–455 (2010).

141. Baldocchi, D. *et al.* FLUXNET: A New Tool to Study the Temporal and Spatial Variability of Ecosystem-Scale Carbon Dioxide, Water Vapor, and Energy Flux Densities. *Bull. Am. Meteorol. Soc.* **82**, 2415–2434 (2001).

142. Hyson, P., Garratt, J. R. & Francey, R. J. Algebraic and electronic corrections of measured uw covariance in the lower atmosphere. **16**, 43–47 (1977).

143. Wilczak, J. M., Oncley, S. P. & Stage, S. A. Sonic anemometer tilt correction algorithms. *Boundary-Layer Meteorol.* **99**, 127–150 (2001).

144. Mammarella, I. *et al.* Determining the contribution of vertical advection to the net ecosystem exchange at Hyytiäläforest, Finland. *Tellus, Ser. B Chem. Phys. Meteorol.* **59**, 900–909 (2007).

145. Yuan, R. *et al.* Expansion of the planar-fit method to estimate flux over complex terrain.

Meteorol. Atmos. Phys. **110**, 123–133 (2011).

146. Ross, A. N. & Grant, E. R. A new continuous planar fit method for calculating fluxes in complex, forested terrain. *Atmos. Sci. Lett.* **16**, 445–452 (2015).

147. Lee, J. D. *et al.* Year-round measurements of nitrogen oxides and ozone in the tropical North Atlantic marine boundary layer. *J. Geophys. Res. Atmos.* **114**, 1–14 (2009).

148. Andersen, S. T. *et al.* Long-Term no*x* measurements in the remote marine tropical troposphere. *Atmos. Meas. Tech.* **14**, 3071–3085 (2021).

149. Luhar, A. K., Woodhouse, M. T. & Galbally, I. E. A revised global ozone dry deposition estimate based on a new two-layer parameterisation for air–sea exchange and the multi-year MACC composition reanalysis. *Atmos. Chem. Phys.* **18**, 4329–4348 (2018).

150. Metzger, S. *et al.* Eddy4R 0.2.0: A DevOps model for community-extensible processing and analysis of eddy-covariance data based on R, Git, Docker, and HDF5. *Geosci. Model Dev.* **10**, 3189–3206 (2017).

151. Brock, F. V. A Nonlinear Filter to Remove Impulse Noise from Meteorological Data. *Journal of Atmospheric and Oceanic Technology* vol. 3 51–58 (1986).

152. Starkenburg, D. *et al.* Assessment of despiking methods for turbulence data in micrometeorology. *J. Atmos. Ocean. Technol.* **33**, 2001–2013 (2016).

153. Wilczak, James, M., Oncley, Steven, P. & Stage, Steven, A. Sonic anemometer tilt correction algorithms. *Boundary-Layer Meteorol.* **99**, 127–150 (2001).

154. Hartmann, J., Gehrmann, M., Kohnert, K., Metzger, S. & Sachs, T. New calibration procedures for airborne turbulence measurements and accuracy of the methane fluxes during the AirMeth campaigns. *Atmos. Meas. Tech.* **11**, 4567–4581 (2018).

155. Feng, J., Zhang, B., Wei, Z. & Xu, D. Effects of Averaging Period on Energy Fluxes and the Energy-Balance Ratio as Measured with an Eddy-Covariance System. *Boundary-Layer Meteorol.* **165**, 545–551 (2017).

156. Burba, G. & Anderson, D. *A Brief Practical Guide to Eddy covariance CO2 flux measurements*. *LI-COR Biosciences* (Li-COR Biosciences, 2010). doi:10.13140/RG.2.1.1626.4161.

157. Businger, J. A., Wyngaard, J. C., Izumi, Y. & Bradley, E. F. Flux-profile relationships in the atmospheric surface layer. *Journal of the Atmospheric Sciences* vol. 28 181–189 (1971).

158. Högström, U. Non-dimensional wind and temperature profiles in the atmospheric surface

layer: A re-evaluation. *Boundary-Layer Meteorol.* **42**, 55–78 (1988).

159. World Meteorological Organisation. *Guide to meteorological instruments and methods of observation.* (WMO-No. 8, 2008).

160. Yang, M. *et al.* Air-sea fluxes of CO2 and CH4 from the penlee point atmospheric observatory on the south-west coast of the UK. *Atmos. Chem. Phys.* **16**, 5745–5761 (2016).

161. Yang, M. *et al.* Insights from year-long measurements of air-water CH4 and CO2 exchange in a coastal environment. *Biogeosciences Discuss.* **16**, 961–978 (2019).

162. Kljun, N., Rotach, M. W. & Schmid, H. P. A Three-Dimensional Backward Lagrangian Footprint Model For A Wide Range Of Boundary-Layer Stratifications. *Boundary-Layer Meteorol.* **103**, 205–226 (2002).

163. Langford, B., Acton, W., Ammann, C., Valach, A. & Nemitz, E. Eddy-covariance data with low signal-to-noise ratio: Time-lag determination, uncertainties and limit of detection. *Atmos. Meas. Tech.* **8**, 4197–4213 (2015).

164. Lenschow, D. H., Mann, J. & Kristensen, L. How Long Is Long Enough When Measuring Fluxes and Other Turbulence Statistics? *American Meteorological Society* vol. 11 661–673 (1994).

165. Fairall, C. W., Hare, J. E., Edson, J. B. & McGillis, W. *Parameterization and Micrometeorological Measurement of Air-Sea Gas Transfer. Boundary Layer Meteorology* vol. 96 (2000).

166. Blomquist, B. W., Huebert, B. J., Fairall, C. W. & Faloona, I. C. Determining the sea-air flux of dimethylsulfide by eddy correlation using mass spectrometry. *Atmos. Meas. Tech.* **3**, 1–20 (2010).

167. Lenschow, D. H. & Kristensen, L. Uncorrelated noise in turbulence measurements. *J. Atmos. Ocean. Technol.* **2**, 68–81 (1985).

168. Fairall, C. W. Interpretation of eddy-correlation measurements of particulate deposition and aerosol flux. *Atmos. Environ.* **18**, 1329–1337 (1984).

169. Garrett, W. D. Collection of Slick-forming Materials from the Sea Surface. *Limnol. Oceanogr.* **10**, 602–605 (1965).

170. Harvey, G. W. & Burzell, L. A. A Simple Microlayer Method for Small Samples. *Limnol. Oceanogr.* **17**, 156–157 (1972).

171. Luther, G. W., Swartz, C. B. & Ullman, W. J. Direct Determination of Iodide in Seawater by

Cathodic Stripping Square Wave Voltammetry. 1721–1724 (1988).

172. Martino, M., Lézé, B., Baker, A. R. & Liss, P. S. Chemical controls on ozone deposition to water. *Geophys. Res. Lett.* **39**, 39–43 (2012).

173. Pound, R., Sherwen, T., Helmig, D., Carpenter, L. & Evans, M. Influences of oceanic ozone deposition on tropospheric photochemistry. *Atmos. Chem. Phys. Discuss.* 1–25 (2019) doi:10.5194/acp-2019-1043.

174. Sherwen, T. *et al.* A machine learning based global sea-surface iodide distribution. *Earth Syst. Sci. Data Discuss.* 1–40 (2019) doi:10.5194/essd-2019-40.

175. Luhar, A. K., Galbally, I. E., Woodhouse, M. T. & Thatcher, M. An improved parameterisation of ozone dry deposition to the ocean and its impact in a global climate-chemistry model. *Atmos. Chem. Phys.* **17**, 3749–3767 (2017).

176. Morris, J. C. The aqueous solubility of ozone - a review. *Ozone News* vol. 1 14–16 (1988).

177. Johnson, P. N. & Davis, R. A. Diffusivity of Ozone in Water. **9568**, 1485–1487 (1996).

178. Hansell, D. A., Carlson, C. A., Repeta, D. J. & Schlitzer, R. Dissolved organic matter in the ocean a controversy stim ulates new insights. *Oceanography* **22**, 202–211 (2009).

179. Gardner, W. D., Mishonov, A. V. & Richardson, M. J. Global POC concentrations from in-situ and satellite data. *Deep. Res. Part II Top. Stud. Oceanogr.* **53**, 718–740 (2006).

180. Maciejewska, A. & Pempkowiak, J. DOC and POC in the water column of the southern Baltic. Part I. Evaluation of factors influencing sources, distribution and concentration dynamics of organic matter**This study was supported by the Baltic-C/BONUS Plus EUFP6 Project, statutory activities o. *Oceanologia* **56**, 523–548 (2014).

181. Coleman, L., Varghese, S., Tripathi, O. P., Jennings, S. G. & O'Dowd, C. D. Regional-Scale Ozone Deposition to North-East Atlantic Waters. *Adv. Meteorol.* **2010**, 1–16 (2010).

182. Slowey, J. F., Jeffrey, L. M. & Hood, D. W. The fatty-acid content of ocean water. *Geochim. Cosmochim. Acta* **26**, 607–616 (1962).

183. Koch, B. P. & Dittmar, T. From mass to structure: An aromaticity index for high-resolution mass data of natural organic matter. *Rapid Commun. Mass Spectrom.* **20**, 926–932 (2006).

184. Longnecker, K., Kido Soule, M. C. & Kujawinski, E. B. Dissolved organic matter produced by Thalassiosira pseudonana. *Mar. Chem.* **168**, 114–123 (2015).

185. Giavalisco, P. *et al.* Elemental formula annotation of polar and lipophilic metabolites using 13C, 15N and 34S isotope labelling, in combination with high-resolution mass spectrometry.

Plant J. **68**, 364–376 (2011).

186. Petras, D. *et al.* High-resolution liquid chromatography tandem mass spectrometry enables large scale molecular characterization of dissolved organic matter. *Front. Mar. Sci.* **4**, (2017).

187. Pemberton, J. A. *et al.* Untargeted characterisation of dissolved organic matter contributions to rivers from anthropogenic point sources using direct-infusion and high-performance liquid chromatography/Orbitrap mass spectrometry. *Rapid Commun. Mass Spectrom.* **34**, (2020).

188. Brüggemann, M. *et al.* Interfacial photochemistry of biogenic surfactants: A major source of abiotic volatile organic compounds. *Faraday Discuss.* **200**, 59–74 (2017).

189. Pluskal, T., Castillo, S., Villar-Briones, A. & Orešič, M. MZmine 2: Modular framework for processing, visualizing, and analyzing mass spectrometry-based molecular profile data. *BMC Bioinformatics* **11**, (2010).

190. Verkh, Y., Rozman, M. & Petrovic, M. Extraction and cleansing of data for a non-targeted analysis of high-resolution mass spectrometry data of wastewater. *MethodsX* **5**, 395–402 (2018).

191. Gunten, U. Von. Ozonation of drinking water: Part I. Oxidation kinetics and product formation. *Water Res.* **37**, 1443–1467 (2003).

192. Melendez-Perez, J. J., Martínez-Mejia, M. J. & Eberlin, M. N. A reformulated aromaticity index equation under consideration for non-aromatic and non-condensed aromatic cyclic carbonyl compounds. *Org. Geochem.* **95**, 29–33 (2016).

193. Tedetti, M., Kawamura, K., Charrièra, B., Chevalier, N. & Sempéré, R. Determination of low molecular weight dicarboxylic and ketocarboxylic acids in seawater samples. *Anal. Chem.* **78**, 6012–6018 (2006).

194. Wang, L. *et al.* Bioactive hydroxyphenylpyrrole-dicarboxylic acids from a new marine Halomonas sp.: Production and structure elucidation. *Appl. Microbiol. Biotechnol.* **72**, 816–822 (2006).

195. Traulsen, F., Andersson, J. T. & Ehrhardt, M. G. Acidic and non-acidic products from the photo-oxidation of the crude oil component dibenzothiophene dissolved in seawater. *Anal. Chim. Acta* **392**, 19–28 (1999).

196. Mvula, E. & Von Sonntag, C. Ozonolysis of phenols in aqueous solution. *Org. Biomol. Chem.* **1**, 1749–1756 (2003).

197. Gašparović, B., Plavšić, M., Ćosović, B. & Saliot, A. Organic matter characterization in the sea surface microlayers in the subarctic Norwegian fjords region. *Mar. Chem.* **105**, 1–14

(2007).

198. Hannun, R. A. *et al.* A cavity-enhanced ultraviolet absorption instrument for high-precision, fast-Time-response ozone measurements. *Atmos. Meas. Tech.* **13**, 6877–6887 (2020).